Publ. Astron. Soc. Japan (2023) 75 (6), 1030–1071
https://doi.org/10.1093/pasj/psad056
Advance Access Publication Date: 2023 September 13

Revisiting planetary systems in the Okayama Planet Search Program: A new long-period planet, RV astrometry joint analysis, and a multiplicity-metallicity trend around evolved stars

Huan-Yu Teng [1,*] Bun'ei Sato [1] Masayuki Kuzuhara [2] Takuya Takarada [2] Masashi Omiya [2,3] Hiroki Harakawa [4] Hideyuki Izumiura [5] Eiji Kambe [4] Mesut Yilmaz [6] Ilfan Bikmaev [7,8] Selim O. Selam [6] Timothy D. Brandt [9] Guang-Yao Xiao [10,11] Michitoshi Yoshida [4] Yoichi Itoh [12] Hiroyasu Ando [3] Eiichiro Kokubo [3] and Shigeru Ida [13]

[1]Department of Earth and Planetary Sciences, School of Science, Tokyo Institute of Technology, 2-12-1 Ookayama, Meguro-ku, Tokyo 152-8550, Japan
[2]Astrobiology Center, National Institutes of Natural Sciences, 2-21-1 Osawa, Mitaka, Tokyo 181-8588, Japan
[3]National Astronomical Observatory of Japan, National Institutes of Natural Sciences, 2-21-1 Osawa, Mitaka, Tokyo 181-8588, Japan
[4]Subaru Telescope, National Astronomical Observatory of Japan, National Institutes of Natural Sciences, 650 North A'ohoku Pl., Hilo, HI 96720, USA
[5]Okayama Branch Office, Subaru Telescope, National Astronomical Observatory of Japan, National Institutes of Natural Sciences, Kamogata, Asakuchi, Okayama 719-0232, Japan
[6]Ankara University, Dept. of Astronomy and Space Sciences, TR-06100 Besevler/Ankara, Türkiye
[7]Kazan Federal University, Kremlyevskaya Str. 18, Kazan, 420008, Russia
[8]Academy of Sciences of Tatarstan, Bauman Str. 20, Kazan, 420111, Russia
[9]Department of Physics, University of California, Santa Barbara, Santa Barbara, CA 93106, USA
[10]CAS Key Laboratory of Optical Astronomy, National Astronomical Observatories, Chinese Academy of Sciences, Beijing 100101, China
[11]Department of Physics, College of Science, Tibet University, Lhasa 850000, China
[12]Nishi-Harima Astronomical Observatory, Center for Astronomy, University of Hyogo, 407-2 Nishigaichi, Sayo, Hyogo 679-5313, Japan
[13]Earth-Life Science Institute, Tokyo Institute of Technology, 2-12-1 Ookayama, Meguro-ku, Tokyo 152-8550, Japan

*E-mail: hyteng@bao.ac.cn

Received 2023 April 3; Accepted 2023 August 10

Abstract

In this study, we revisit 32 planetary systems around evolved stars observed within the framework of the Okayama Planet Search Program (OPSP) and its collaborative framework of the East Asian Planet Search Network to search for additional companions

© The Author(s) 2023. Published by Oxford University Press on behalf of the Astronomical Society of Japan.
All rights reserved. For permissions, please e-mail: journals.permissions@oup.com

Downloaded from https://academic.oup.com/pasj/article/75/6/1030/7272944 by ANKARA user on 22 December 2023

and investigate the properties of stars and giant planets in multiple-planet systems. With our latest radial velocities obtained from Okayama Astrophysical Observatory, we confirm an additional giant planet in the wide orbit of the 75 Cet system ($P_c = 2051.62^{+45.98}_{-40.47}$ d, $M_c \sin i = 0.912^{+0.088}_{-0.090}$ M_J, and $a_c = 3.929^{+0.052}_{-0.058}$ au), along with five stars exhibiting long-term radial velocity accelerations, which indicates massive companions in the wide orbits. We also find that the radial velocity variations of several planet-harboring stars may indicate additional planet candidates, stellar activities, or other understudied sources. These stars include ϵ Tau, 11 Com, 24 Boo, 41 Lyn, 14 And, HD 32518, and ω Ser. We further constrain the orbital configuration of the HD 5608, HD 14067, HD 120084, and HD 175679 systems by combining radial velocities with astrometry, as their host central stars exhibit significant astrometric accelerations. For other systems, we simply refine their orbital parameters. Moreover, our study indicates that the OPSP planet-harboring stars are more metal poor compared to the currently known planet-harboring stars, and this is likely due to the $B - V$ color upper limit at 1.0 for star selection in the beginning of the survey. Finally, by investigating the less massive giant planets (<5 M_J) around currently known planet-harboring evolved stars, we find that metallicity positively correlates with the multiplicity and total planet mass of the system, which can be evidence for the core-accretion planet formation model.

Key words: planetary systems — stars: individual — techniques: radial velocities

1 Introduction

So far, over 5000 extrasolar planets (exoplanets) having various orbital properties have been discovered around different types of stars. Most of these planets were known to orbit stars having solar mass or lower mass and living in their main-sequence stage. Solar twins ($0.7 \leq M_\star < 1.5$ $M_\odot$), e.g., G and K dwarfs, are the optimal objects to search for "solar systems" in terms of giving an answer to the formation of solar systems. Low-mass stars ($M_\star < 0.7$ $M_\odot$), e.g., the M dwarfs, are the best targets to search for "Earths" in habitable zones in terms of terrestrial world and habitability. They are both befitting candidates for the most widely used observational techniques, i.e., the transit method and radial velocity (RV) method (or Doppler method). On the contrary, those massive stars ($\gtrsim 1.5$ $M_\odot$), e.g., intermediate-mass stars ($1.5 \leq M_\star < 5$ $M_\odot$), are observationally poor candidates during the main-sequence phase. The large body of massive stars restricts the detectability of planets in transit, and the lack of absorption lines due to their high surface temperature and fast self-rotation (Lagrange et al. 2009) confines RV measurement to bad accuracy.

However, planet surveys around massive stars are particularly valuable concerning the point that the properties of giant planets would constrain the time scale and the mechanism of planet formation. Compared to less massive stars, both the lifetimes of the massive host stars and those of their surrounding disks (Haisch et al. 2001a, 2001b; Andrews et al. 2013; Ribas et al. 2015) can be as short as the critical time scales of the core-accretion planet formation scenario (a few million years; Pollack et al. 1996), a popular and favorable solution to solve the puzzle. Another plausible solution refers to the disk-instability scenario (Boss 1997), where planets can form in a much shorter period (as short as a few thousand years) than in the core-accretion scenario. Thus, more observational evidence of planets and their properties is welcome in understanding the formation of giant planets.

The evolved counterpart of massive stars, spectroscopically G- or K-type subgiants or giants, have lower temperatures and slower rotation, suggesting that these targets are more promising to RV measurements. From this, the evolved stars have been widely surveyed in a number of projects: Lick (Frink et al. 2001; Reffert et al. 2015), the Okayama Planet Search Program (OPSP: Sato et al. 2005), with its extended Subaru program (Sato et al. 2010), and its collaborative survey the East Asian Planet Search Network (EAPS-Net; Izumiura 2005), the ESO planet search program (Setiawan et al. 2003), the Tautenburg Observatory Planet Search (Hatzes et al. 2005; Döllinger et al. 2007), the "Retired A Stars and Their Companions" (Johnson et al. 2007), the Penn State-Toruń Planet Search (Niedzielski et al. 2007), including its follow-up program "Tracking Advanced Planetary systems" (Niedzielski et al. 2015a), the BOAO K-giant survey (Han et al. 2010), the Pan-Pacific Planet Search (PPPS: Wittenmyer et al. 2011), the

Downloaded from https://academic.oup.com/pasj/article/75/6/1030/7272944 by ANKARA user on 22 December 2023

EXoPlanet aRound Evolved StarS project (Jones et al. 2011). Based on large surveys, over 150 planetary systems around evolved stars have been discovered.[1]

Among these systems, ∼15% of them are known to be multiple-planet systems. Thanks to long-baseline RV surveys, these systems can be more widely discovered. These multiple-planet systems are of primary focus and a particular interest in terms of the formation and evolution of planetary systems. Furthermore, these multiple-planet systems around evolved stars are mostly in the pattern of "planet pairs," and many of them have small orbital separations or they are in mean-motion resonance (MMR). Some typical systems with small orbital separation include BD +20 2457 (Niedzielski et al. 2009), a metal-poor K2 giant with [Fe/H] = −1.0 orbited by two brown dwarf-mass bodies with near 3:2 MMR; HD 33844 (Wittenmyer et al. 2016a), a two-giant-planets system in 5:3 resonance; 7 CMa, HD 5319, HD 99706, HD 102329, HD 116029, and HD 200964 (Johnson et al. 2011; Wittenmyer et al. 2011; Giguere et al. 2015; Bryan et al. 2016; Luque et al. 2019), harboring giant planet pairs with a period ratio equal to or close to 4:3. Some typical systems with large orbital separation include HD 4732 (Sato et al. 2013a), a subgiant star with two giant planets at 1.19 and 4.60 au; ν Oph (Quirrenbach et al. 2011, 2019; Sato et al. 2012), an $M_\star = 2.7\ M_\odot$ giant star having two brown dwarfs in 6:1 resonance at 1.8 and 6.0 au.

In addition, precise astrometry has recently started to help much more in planet detection and characterization, and it is especially sensitive for massive companions in wide orbits. Precise astrometry can be effectively combined with RV measurements to distinguish and constrain the masses of giant planets, brown dwarfs, and low-mass stellar companions, as well as to search for wide-orbit planets suggested by RV long-term acceleration. Several groups of researchers have been working on joint constraints on RV-detected planets. Li et al. (2021) used the Keplerian orbital code `orvara` (Brandt 2021) to fit the published RVs and Hipparcos–Gaia Catalog of Accelerations (HGCA; Brandt 2018, 2021; Gaia EDR3 version) of nine single and massive RV-detected exoplanets and obtained an accurate determination of their masses. Kiefer et al. (2021) investigated the nature of hundreds of RV-detected exoplanets with `GASTON` (Kiefer et al. 2019). Feng et al. (2022) identified 167 cold giants and 68 other types of companions by combining RVs and astrometric data with `pexo` (Feng et al. 2019). Delisle and Ségransan (2022) analyzed three systems on the basis of Hipparcos data, together with on-ground RVs, with their newly developed `kepmodel` code. More recently, Xiao et al. (2022) independently measured the masses of 115 RV-detected substellar companions with `orvara` and `HGCA`.

The giant planet–metallicity relation has been studied for years. Many studies have suggested a positive planet-metallicity correlation that giant planets are preferentially found around more metal-rich stars (e.g., Fischer & Valenti 2005; Reffert et al. 2015; Jones et al. 2016; Wittenmyer et al. 2017; Wolthoff et al. 2022), but some others (e.g., Jofré et al. 2015) have conservatively stated that no clear correlation exists. Yet, a relation between stellar metallicity and the multiplicity of planets has not been well established or quantified. Fischer and Valenti (2005) pointed out that the presence of multiple-planet systems appeared to correlate with high stellar metallicity. Jofré et al. (2015) also showed that evolved stars hosting multiple planets appear to be more metal rich compared with evolved stars hosting single planets. These trends follow the study on main-sequence stars by Wright et al. (2009).

In this study, we revisit the 32 planetary systems involved in OPSP. These systems were released no later than 2018 with limited RV measurements. Here we extend their time baseline of RV monitoring to hunt for extra companions and update the orbital parameters of the system as well as their host star. We also investigate the correlation between orbital properties and host star properties, especially for multiple-planet systems. In section 2, we revise the general information and 20-yr operation of OPSP, and we update the properties of stars involved in this study. In section 3, we describe the observations and data we have used in this study, and we provide the analysis of RV data. In section 4, we release the latest RV results of the 32 planetary systems, including the newly discovered 75 Cet c. In section 5, we present another seven stars showing noteworthy RV variability. In section 6, we present RV astrometry joint fitting results of four systems. In section 7, we discuss the properties of planet-harboring evolved stars and their planetary systems. Finally, in section 8, we summarize the paper.

2 OPSP

OPSP surveys late-G (including early-K) giant stars in RV, aiming to search for planets around intermediate-mass stars in their evolved stages. OPSP selected 300 late-G giant stars and began the survey in 2001.

To extend the OPSP program, an international network was established among Japanese, Korean, and Chinese researchers using three telescopes in the 2 m class in 2005 (EAPS-Net: Izumiura 2005), and the Subaru Planet Search Program was started in 2006. The Subaru program targets ∼300 late-G giant stars, which could be examined with 2 m class telescopes after a quick identification of stars exhibiting large RV variation. The survey at TÜBİTAK

1 We defined evolved stars as stars having a surface gravity of $\log g < 3.5$. Here we do not strictly account for samples by intermediate mass ($1.5 < M_\star < 5\ M_\odot$); thus, some less massive stars are included.

Downloaded from https://academic.oup.com/pasj/article/75/6/1030/7272944 by ANKARA user on 22 December 2023

National Observatory (TUG) is another extension of OPSP within the framework of an international collaboration between Türkiye, Russia, and Japan.

The targeted stars in the aforementioned surveys were selected from the Hipparcos catalog (ESA 1997) and they generally obey the following criteria: stars with (1) $V < 7$ to attain a sufficient signal-to-noise ratio, (2) a color index of $0.6 \lesssim B - V \lesssim 1.0$ to achieve intrinsic RV stability to a level of $\sigma \lesssim 20$ m s^{-1}, (3) an absolute magnitude of $-3 \lesssim M_V \lesssim 2$ to include stars with masses of 1.5–5 $M_\odot$.

By the end of 2021, OPSP and its extensions had discovered 36 planetary systems, including systems with substellar companions, four candidates (ϵ Psc, HD 40956, HD 111591, and HD 175679), and independently confirmed three systems (κ CrB, ν Oph, and HD 210702). In 2022, OPSP confirmed another two systems around two red giant stars (HD 167768 and HD 184010).

In this study, we revisited planetary systems, which were observed within OPSP and its extensions and were released before 2019. But we did not include stars involved in the Korean-Japanese planet search program (Omiya et al. 2009, HD 119445; Omiya et al. 2012, HD 100655; Jeong et al. 2018, HD 40956 and HD 111591). The update on these stars will appear in a forthcoming paper.

The stellar parameters in this study, as listed in table 1, were obtained in two ways, which were discriminatively illustrated with different markers in figure 1. For stars involved in Takeda, Sato, and Murata (2008), we followed the same method as Teng et al. (2022b) and re-estimated their stellar parameters by using `isoclassify` (Huber et al. 2017) with the atmospheric parameters given by Takeda, Sato, and Murata (2008). For other stars, we directly adopted the stellar parameters given in the planet detection paper, as indicated in table 2.

3 Observations and analyses

3.1 Okayama Astrophysical Observatory observations

The RV data in this study were mainly extracted from the spectra that were obtained by the 1.88 m reflector with a high-dispersion echelle spectrograph (HIDES: Izumiura 1999) at Okayama Astrophysical Observatory (OAO) from 2001 to 2021. The instrument was equipped with an iodine cell in the HIDES optical path to HIDES, which provided numerous iodine absorption lines in the range of 5000–5800 Å as a reference for precise RV measurements.

HIDES has experienced several upgrades. At first, HIDES was set to cover a wavelength range of 5000–6100 Å with one 2K × 4K CCD. In 2007 December, HIDES was upgraded from a single CCD to a mosaic of three. This widened the wavelength region to 3700–7500 Å (3700–5000 Å, 5000–5800 Å, and 5800–7500 Å for each, respectively) and enabled us to simultaneously measure the level of stellar activities (e.g., Ca II H&K lines) and line profiles as well as RVs. In 2010, HIDES was equipped with a new high-efficiency fiber-link system with its own iodine cell installed in the optical path. This greatly enhanced the overall throughput (Kambe et al. 2013) and efficiently shortened the exposure time of our targets. In 2018, HIDES was upgraded with its slit mode elements fully removed from the HIDES optical path, and with the optical instruments of the fiber-link mode re-arranged on a new stabilized platform in the precise temperature-controlled coudé room. Since the optical path was re-arranged in the upgrade, fiber-link modes pre-/post-upgrade are considered to be two independent instruments.

In this study, the HIDES RVs were extracted by spectra from both conventional slit mode (HIDES-S) and fiber mode pre- and post-upgrades (HIDES-F1 and HIDES-F2).

3.2 Other observations

The RV data obtained from sites other than OAO were mainly obtained from published papers. These include data obtained from the high-dispersion spectrograph (HDS; Noguchi et al. 2002) mounted on the Subaru telescope at Maunakea, the Coudé echelle spectrograph (CES[2]; Zhao & Li 2001) and the high-resolution spectrograph (HRS) on the 2.16 m telescope at Xinglong Observatory, the UCLES echelle spectrograph (Diego et al. 1990) on the Anglo-Australian Telescope at Siding Spring Observatory, the Hamilton echelle spectrograph on the Coudé Auxiliary Telescope at Lick Observatory (Lick), the CES on the 2 m Alfred Jensch Telescope (AJT) at Thuringia State Observatory, and the CES on the 1.5 m Russian-Turkish Telescope at TUG. Furthermore, we obtained new RV data from TUG after the last data release in 2017 January (Yılmaz et al. 2017). A listing of the data acquisition for each star is given in table 2.

3.3 RV from HIDES spectra

We extracted RVs with the same methodology given in Teng et al. (2022b, 2023). Here, we briefly review the flow.

The reduction of echellé spectra taken by HIDES was performed with IRAF[3] packages in a standard way. To

2 The CES pre-upgrade and post-upgrade are respectively marked as CES-O and CES-N.

3 IRAF is distributed by the National Optical Astronomy Observatory, which is operated by the Association of Universities for Research in Astronomy, Inc. under a cooperative agreement with the National Science Foundation, USA.

Downloaded from https://academic.oup.com/pasj/article/75/6/1030/7272944 by ANKARA user on 22 December 2023

Table 1. Stellar parameters.*

	π (mas)	V (mag)	$B-V$ (mag)	Spec. type	$T_{\rm eff,\,sp}$ (K)	[Fe/H]$_{\rm sp}$ (dex)	$\log g_{\star,\,\rm sp}$ (cgs)	$T_{\rm eff}$ (K)	[Fe/H] (dex)	$\log g_{\star}$ (cgs)	$L_{\star}$ ($L_{\odot}$)	$M_{\star}$ ($M_{\odot}$)	$R_{\star}$ ($R_{\odot}$)
HD 2952	9.1205	5.92	1.04	K0 III	4844	0.00	2.67	4853	$-0.00^{+0.10}_{-0.10}$	$2.65^{+0.09}_{-0.08}$	$58.59^{+8.12}_{-6.43}$	$1.91^{+0.42}_{-0.22}$	$10.90^{+0.57}_{-0.81}$
HD 4732	18.1441	5.90	0.94	K0 IV	4959	0.01	3.16	4898	$-0.01^{+0.05}_{-0.11}$	$3.17^{+0.05}_{-0.06}$	$13.13^{+0.81}_{-0.78}$	$1.39^{+0.15}_{-0.17}$	$5.03^{+0.12}_{-0.13}$
HD 5608	17.0697	5.98	1.00	K0 IV	4854	0.06	3.03	4807	$0.04^{+0.07}_{-0.10}$	$3.06^{+0.08}_{-0.08}$	$14.28^{+4.07}_{-3.26}$	$1.29^{+0.23}_{-0.23}$	$5.43^{+0.70}_{-0.62}$
HD 14067	7.1092	6.51	1.03	G9 III	—	—	—	4815	$-0.10^{+0.08}_{-0.08}$	$2.61^{+0.10}_{-0.10}$	79	$2.40^{+0.20}_{-0.20}$	$12.40^{+1.10}_{-1.10}$
75 Cet	12.1717	5.36	1.00	G3 III	4846	0.00	2.63	4809	$0.10^{+0.08}_{-0.05}$	$2.69^{+0.03}_{-0.04}$	$51.82^{+1.46}_{-2.45}$	$1.92^{+0.07}_{-0.08}$	$10.38^{+0.15}_{-0.26}$
81 Cet	9.5199	5.65	1.02	G5 III	4785	−0.06	2.35	4734	$-0.11^{+0.10}_{-0.06}$	$2.41^{+0.07}_{-0.06}$	$57.58^{+8.43}_{-5.14}$	$1.23^{+0.30}_{-0.25}$	$11.21^{+0.81}_{-0.35}$
ϵ Tau	22.3654	3.53	1.10	K0 III	4883	0.13	2.57	4877	$0.10^{+0.11}_{-0.10}$	$2.66^{+0.03}_{-0.05}$	$78.11^{+5.68}_{-5.82}$	$2.57^{+0.17}_{-0.25}$	$12.35^{+0.41}_{-0.36}$
HD 32518	8.2192	6.42	1.11	K1 III	—	—	—	4580	$-0.15^{+0.04}_{-0.04}$	$2.10^{+0.15}_{-0.15}$	49	$1.13^{+0.18}_{-0.18}$	$10.22^{+0.87}_{-0.87}$
6 Lyn	18.2183	5.86	0.93	K0 IV	4978	−0.13	3.16	4941	$-0.17^{+0.11}_{-0.07}$	$3.16^{+0.08}_{-0.08}$	$13.14^{+3.23}_{-2.66}$	$1.32^{+0.20}_{-0.21}$	$4.94^{+0.55}_{-0.50}$
HD 47366	11.9187	6.11	0.99	K1 III	—	—	—	4866	$-0.02^{+0.09}_{-0.09}$	$2.97^{+0.06}_{-0.06}$	26	$1.81^{+0.13}_{-0.13}$	$7.30^{+0.33}_{-0.33}$
o Uma	17.9335	3.42	0.86	G4 II-III	5242	−0.09	2.64	5075	$-0.16^{+0.08}_{-0.10}$	$2.58^{+0.06}_{-0.05}$	$115.52^{+20.53}_{-17.61}$	$2.72^{+0.14}_{-0.16}$	$13.84^{+1.19}_{-1.04}$
4 Uma	13.2035	4.61	1.17	K1 III	—	—	—	4415	$-0.25^{+0.04}_{-0.04}$	$1.80^{+0.15}_{-0.15}$	103	$1.23^{+0.15}_{-0.15}$	$18.11^{+1.47}_{-1.47}$
41 Lyn	11.8163	5.39	0.99	K0 III-IV	4771	−0.34	2.26	4797	$-0.32^{+0.10}_{-0.10}$	$2.37^{+0.05}_{-0.07}$	$60.30^{+14.76}_{-7.39}$	$1.07^{+0.27}_{-0.16}$	$11.13^{+1.58}_{-0.68}$
HD 104985	9.9280	5.78	1.03	G9 III	4679	−0.35	2.47	4738	$-0.32^{+0.10}_{-0.10}$	$2.42^{+0.07}_{-0.06}$	$58.87^{+11.69}_{-11.20}$	$1.22^{+0.29}_{-0.23}$	$11.12^{+1.23}_{-0.74}$
11 Com	10.1677	4.74	1.00	G8 III	4841	−0.28	2.51	4874	$-0.26^{+0.10}_{-0.10}$	$2.45^{+0.08}_{-0.08}$	$95.11^{+48.85}_{-29.11}$	$2.09^{+0.64}_{-0.63}$	$13.76^{+2.85}_{-2.45}$
HD 120084	9.6277	5.90	1.00	G7 III	4892	0.09	2.71	4879	$0.10^{+0.08}_{-0.10}$	$2.74^{+0.07}_{-0.09}$	$54.68^{+9.23}_{-7.44}$	$2.16^{+0.31}_{-0.26}$	$10.37^{+0.82}_{-0.80}$
24 Boo	10.5895	5.58	0.86	G3 IV	4893	−0.77	2.21	4816	$-0.78^{+0.10}_{-0.10}$	$2.28^{+0.09}_{-0.07}$	$75.32^{+17.34}_{-14.85}$	$1.05^{+0.27}_{-0.18}$	$12.19^{+1.45}_{-1.28}$
o CrB	11.9113	5.51	1.02	K0 III	4749	−0.29	2.34	4769	$-0.27^{+0.09}_{-0.10}$	$2.36^{+0.07}_{-0.12}$	$66.37^{+82.64}_{-14.04}$	$1.30^{+0.95}_{-0.36}$	$11.87^{+6.20}_{-1.50}$
γ Lib	20.2593	3.91	1.01	K0 III	4822	−0.30	2.56	4879	$-0.27^{+0.08}_{-0.10}$	$2.50^{+0.06}_{-0.07}$	$78.94^{+4.18}_{-4.49}$	$1.78^{+0.24}_{-0.24}$	$12.38^{+0.30}_{-0.24}$
ω Ser	13.1026	5.22	1.02	G8 III	4770	−0.24	2.21	4724	$-0.12^{+0.01}_{-0.03}$	$2.37^{+0.02}_{-0.04}$	$54.18^{+1.50}_{-2.23}$	$1.01^{+0.07}_{-0.08}$	$10.99^{+0.15}_{-0.24}$
κ CrB	33.3433	4.82	1.00	K0 III-IV	4877	0.10	3.21	4840	$0.09^{+0.07}_{-0.10}$	$3.20^{+0.10}_{-0.10}$	$10.86^{+4.38}_{-3.18}$	$1.33^{+0.24}_{-0.25}$	$4.68^{+0.84}_{-0.71}$
HD 145457	7.3867	6.57	1.04	K0 III	—	—	—	4757	$-0.14^{+0.09}_{-0.09}$	$2.77^{+0.10}_{-0.10}$	45	$1.90^{+0.30}_{-0.30}$	$9.90^{+0.50}_{-0.50}$
ν Oph	22.9031	5.44	0.99	K0 III	4928	0.13	2.63	4887	$0.10^{+0.10}_{-0.10}$	$2.64^{+0.10}_{-0.10}$	$78.48^{+34.05}_{-23.33}$	$2.61^{+0.32}_{-0.57}$	$12.24^{+2.55}_{-1.76}$
HD 167042	20.1313	5.97	0.94	K1 IV	4943	0.00	3.28	4919	$-0.01^{+0.10}_{-0.11}$	$3.23^{+0.07}_{-0.07}$	$11.40^{+2.30}_{-1.98}$	$1.39^{+0.17}_{-0.19}$	$4.63^{+0.43}_{-0.40}$
HD 173416	7.5363	6.04	1.06	G8	—	—	—	4683	$-0.22^{+0.09}_{-0.09}$	$2.48^{+0.10}_{-0.10}$	78	$2.00^{+0.30}_{-0.30}$	$13.50^{+0.90}_{-0.90}$
HD 175679	5.9475	6.13	0.96	G8 III	—	—	—	4844	$-0.14^{+0.10}_{-0.10}$	$2.59^{+0.10}_{-0.10}$	66	$2.70^{+0.30}_{-0.30}$	$11.60^{+1.60}_{-1.60}$
HD 180314	8.1261	6.61	1.02	K0	—	—	—	4917	$0.20^{+0.09}_{-0.09}$	$2.98^{+0.10}_{-0.10}$	44	$2.60^{+0.30}_{-0.30}$	$9.20^{+0.40}_{-0.10}$
ξ Aql	17.5183	4.71	1.02	K0 III	4802	−0.18	2.72	4841	$-0.11^{+0.06}_{-0.10}$	$2.61^{+0.08}_{-0.08}$	$58.54^{+6.02}_{-12.37}$	$1.74^{+0.21}_{-0.28}$	$10.86^{+0.44}_{-1.05}$
18 Del	13.3021	5.51	0.93	G6 III	4985	−0.05	2.84	4980	$-0.06^{+0.10}_{-0.10}$	$2.87^{+0.03}_{-0.05}$	$43.02^{+6.49}_{-4.04}$	$2.10^{+0.13}_{-0.09}$	$8.80^{+0.61}_{-0.40}$
HD 208897	14.9591	6.51	1.01	K0	—	—	—	4860	$0.21^{+0.15}_{-0.15}$	$3.13^{+0.14}_{-0.14}$	12	$1.25^{+0.11}_{-0.11}$	$4.98^{+0.20}_{-0.20}$
HD 210702	18.4593	5.93	0.95	K1 IV	4967	0.01	3.19	4912	$-0.02^{+0.07}_{-0.10}$	$3.23^{+0.08}_{-0.07}$	$10.85^{+2.56}_{-2.14}$	$1.33^{+0.19}_{-0.20}$	$4.54^{+0.49}_{-0.45}$
14 And	13.1681	5.22	1.03	K0 III	4813	−0.24	2.63	4888	$-0.21^{+0.10}_{-0.10}$	$2.55^{+0.06}_{-0.07}$	$69.17^{+14.25}_{-7.51}$	$1.78^{+0.43}_{-0.29}$	$11.55^{+1.12}_{-0.51}$
Source	Gaia	HIP	HIP	HIP	T08	T08	T08	This work	This work	This work	This work	This work	This work

*Stellar parameters of the 32 OPSP planet-harboring stars in this study. Gaia refers to Gaia EDR3, HIP refers to Hipparcos, and T08 refers to Takeda, Sato, and Murata (2008). The stellar parameters of stars included in T08 are re-estimated using the same methodology as in Teng et al. (2022a). The subscript "sp" refers to spectral determination in T08.

Downloaded from https://academic.oup.com/pasj/article/75/6/1030/7272944 by ANKARA user on 22 December 2023

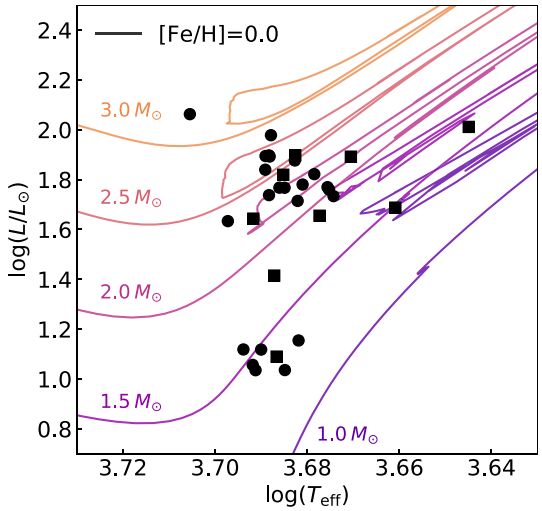


Fig. 1. HR diagram of the 32 OPSP planet-harboring stars in this study. The stars included in Takeda, Sato, and Murata (2008) are shown with circles, while other stars are shown with squares. The colored lines represent evolutionary tracks for solar-metallicity stars of masses between 1.0 and 3.0 $M_\odot$.

make the RV measurement, we used spectra covering 5000–5800 Å in which I_2 absorption lines are superimposed by an I_2 cell. Following the procedure in Sato et al. (2002, 2012), a method based on Butler et al. (1996), we modeled the spectra (I_2 superposed stellar spectra) by using the stellar template and high-resolution I_2 spectra convolved with the instrumental profile (IP) of the spectrograph. The stellar template spectra used for HIDES-S were obtained by deconvolving a pure stellar spectrum with the IP estimated from an I_2 superposed B-type star or flat spectra. If a star has spectra taken by the HIDES-F1 high-resolution mode ($R \sim 100000$) without an I_2 cell in its optical path, the stellar template spectra used for HIDES-F1 and HIDES-F2 were obtained with its high-resolution spectra. Otherwise, we use the same deconvolved spectra for HIDES-S. The final RV values and their measurement errors were taken from the average of the measurement in each segment set in the I_2 absorption region for each instrument.

3.4 Period search and a Keplerian orbital fit

For a given RV time series, a generalized Lomb–Scargle periodogram (hereafter GLS; Zechmeister & Kürster 2009) was performed to search for periodicity caused by planets in the time series. To assess the significance of the periodicity, false alarm probability (FAP) was applied with the approximation method developed by Baluev (2008) in the same package. A peak higher than the 0.1% threshold, i.e., with its FAP value significantly lower than 0.1%, was recognized as a credible signal.

The Keplerian model was generated with free parameters, including Keplerian orbital elements (orbital period P, RV semiamplitude K, the combination of eccentricity e and argument of periastron ω, $\sqrt{e}\cos\omega$ and $\sqrt{e}\sin\omega$, and time of inferior conjunction[4] $T_{\rm c}$), extra Gaussian noise $s_{\rm inst}$, RV offset of different instruments γ, and long-term trends of second order at highest:

$$V_{\rm r} = \sum_{k}^{N_{\rm pl}} V_{r,k}(t|P, K, e, \omega, T_{\rm p}) + \gamma + \dot{\gamma}(t - t_0) + \ddot{\gamma}(t - t_0)^2. \quad (1)$$

Here $N_{\rm pl}$ is the total number of planets in the system, $\dot{\gamma}$ indicates the linear trend term, $\ddot{\gamma}$ indicates the quadratic trend term, and t_0 is the midpoint of the full time span. Since the main instrument, HIDES, is confirmed to be stable after 20 yr without long-term RV drifts (appendix 1), the trend terms in equation (1) are used to fit the long-term RV variations, which are not induced by the instrumental systematics.

The best-fit Keplerian orbits and the uncertainties were derived by the maximum a posteriori (MAP) method from Markov chain Monte Carlo (MCMC) sampling. The MCMC starting point was generated from likelihood maxima, which were determined by a truncated Newton constrained method and a Nelder–Mead method (Nelder & Mead 1965).

The long-term trend was determined by model comparison. The goodness of fit was indicated by reduced chi-square $\chi^2_{\rm red}$ ($\chi^2_{\rm red} = \chi^2/N_{\rm DoF}$, where $N_{\rm DoF}$ is the degree of freedom), and the best model was determined by Bayesian information criteria [BICs; Schwarz 1978; BIC $= -2\ln(\hat{L}) + n_{\rm pars}\ln(n_{\rm data})$, where $\hat{L}$ is the maximized value of the likelihood function, $n_{\rm pars}$ is the number of parameters, and $n_{\rm data}$ is the number of data points]. Fittings with $\chi^2_{\rm red}$ far from 1 were not considered to be well fitted. Models with an absolute value of ΔBIC less than 10 were not considered to be distinct (Kass & Raftery 1996). For two comparable models with different long-term trends, we chose the simpler one with fewer free parameters, i.e., the model described by a simpler long-term trend. However, only when two models have comparable BICs but simultaneously vary in long-term trends and Keplerian orbits, e.g., the orbit solutions of HD 14067 b in Wang et al. (2014), do we provide both models since the current observations cannot determine the true scenario.

The determination of a possible extra planet was made in a similar way. We compared Keplerian models with different planet numbers with $\chi^2_{\rm red}$ and BICs if an extra periodic signal appeared in the periodogram. Similarly, we applied a

4 The periastron passage $T_{\rm p}$ is converted from the inferior conjunction $T_{\rm c}$ after parameter fitting.

Downloaded from https://academic.oup.com/pasj/article/75/6/1030/7272944 by ANKARA user on 22 December 2023

Table 2. Data acquisition details for each planet-harboring star included in OPSP studied in this work.*

Star name	HD number	Data acquisition outside this work	Stellar parameters
HD 2952	HD 2952	Sato et al. (2013b)	This work
HD 4732	HD 4732	Sato et al. (2013a)	This work
HD 5608	HD 5608	Sato et al. (2012)	This work
HD 14067	HD 14067	Wang et al. (2014)	Wang et al. (2014)
75 Cet	HD 15779	Sato et al. (2012)	This work
81 Cet	HD 16400	Sato et al. (2008b)	This work
ϵ Tau	HD 28305	Sato et al. (2007)	This work
HD 32518	HD 32518	Döllinger et al. (2009)	Döllinger et al. (2009)
6 Lyn	HD 45410	Sato et al. (2008b)	This work
HD 47366	HD 47366	Sato et al. (2016)	Sato et al. (2016)
o Uma	HD 71369	Sato et al. (2012)	This work
4 Uma	HD 73108	—	Döllinger et al. (2007)
41 Lyn	HD 81688	Sato et al. (2008a)	This work
HD 104985	HD 104985	Sato et al. (2003, 2008a)	This work
11 Com	HD 107383	Liu et al. (2008)	This work
HD 120084	HD 120084	Sato et al. (2013b)	This work
24 Boo	HD 127243	Takarada et al. (2018)	This work
o CrB	HD 136512	Sato et al. (2013b)	This work
γ Lib	HD 138905	Takarada et al. (2018)	This work
ω Ser	HD 141680	Sato et al. (2013b)	This work
κ CrB	HD 142091	Bowler et al. (2010), Sato et al. (2012)	This work
HD 145457	HD 145457	Sato et al. (2010)	Sato et al. (2010)
ν Oph	HD 163917	Sato et al. (2012), Quirrenbach et al. (2019)	This work
HD 167042	HD 167042	Sato et al. (2008b), Bowler et al. (2010)	This work
HD 173416	HD 173416	Liu et al. (2009)	Liu et al. (2009)
HD 175679	HD 175679	Wang et al. (2012)	Wang et al. (2012)
HD 180314	HD 180314	Sato et al. (2010)	Sato et al. (2010)
ξ Aql	HD 188310	Sato et al. (2008a)	This work
18 Del	HD 199665	Sato et al. (2008a), Ryu et al. (2016)	This work
HD 208897	HD 208897	Yılmaz et al. (2017)	Yılmaz et al. (2017)
HD 210702	HD 210702	Bowler et al. (2010), Sato et al. (2012)	This work
14 And	HD 221345	Sato et al. (2008b)	This work

*The RVs for stars previously studied in OPSP papers were re-extracted from one-dimensional spectra, and may differ from those reported in previous studies. RV data of 6 Lyn in Bowler et al. (2010) and HD 73108 in Döllinger et al. (2007) are not provided, while the RV data of ν Oph in Quirrenbach et al. (2019) include the RVs reported in the original planet discovery paper (Quirrenbach et al. 2011).

model with possible extra planets only if this model was significantly better, i.e., $\chi^2_{\rm red} \sim 1$, and had a lower BIC value that differed by more than 10.

3.5 Chromospheric activity and line profile analysis of HIDES spectra

Spectral line profile deformation can lead to wavelength shifts and mimic planetary signals, and stellar chromospheric activity can also result in RV variations. Thus, line profile analyses are necessary in order to eliminate any fake planetary signal. In this study, these analyses were performed the same as in Teng et al. (2022a).

A bisector inverse span (BIS; Queloz et al. 2001) was adopted as an indicator of line profile asymmetry. The spectra in the iodine-free region (4000–5000 Å) were taken for measurement. The BIS was defined as the offset of the averaged velocity between the cross-correlation function (CCF[5]; Baranne et al. 1996; Pepe et al. 2002) upper region (5%–15% from the continuum of the CCF) and lower region (85%–95% from the continuum of the CCF). The mean removed BIS, $\mathrm{BIS}' = \mathrm{BIS} - \overline{\mathrm{BIS}}$, was calculated in order to suppress the offset between instruments. Notably, while the amplitude of BIS measurements might be expected to change with different instruments, only the offset (without scaling) was taken into account in this analysis.

5 The CCF is constructed by shifting the mask as a function of Doppler velocity, and its weight is determined by the depth of the spectral line. The numerical mask is generated from SPECTRUM (Gray & Corbally 1994) for a G-type giant star with approximately 800 lines.

Downloaded from https://academic.oup.com/pasj/article/75/6/1030/7272944 by ANKARA user on 22 December 2023

The line cores of Ca II H&K lines are widely used in the visible band to trace chromospheric activity (Duncan et al. 1991). In this study, the Ca II H index $S_{\rm H}$, defined in Sato et al. (2013b), was applied to quantify the strength of chromospheric activity. However, Ca II K lines were not included since the signal-to-noise ratio for the spectra in this region was not high enough for measurement. If a stellar chromospheric activity causes an apparent RV variation, a clear correlation between RV and $S_{\rm H}$ can be detected (e.g., figure 9 of Sato et al. 2013b). Additionally, it should be noted that Ca II H&K lines are located in the order overlapping regions in HIDES-F1 and HIDES-F2 spectra; therefore, $S_{\rm H}$ cannot be measured with HIDES-F1 and HIDES-F2 spectra.

4 Fitting results and discovery of a new planet

4.1 Refined orbital parameters

Following the methodology outlined in subsection 3.4, we refined the orbital parameters of the 32 revisited systems. Our analysis revealed an additional planet, 75 Cet c, in one of the systems, and five systems with significant long-term trends: HD 5608, κ CrB, HD 167042, 18 Del, and HD 208897.

This manuscript provides a comprehensive listing of the best-fit orbital parameters in table 3. The online material[6] contains the orbital parameters as well as additional parameters such as extra jitter and instrumental offsets. Furthermore, the online material includes a compilation of all RV and other spectral measurements.

4.2 A new planet: 75 Cet c

75 Cet (HD 15779, HIP 11791) is a G3 III star and reported to harbor a giant planet in Sato et al. (2012). We started to observe 75 Cet in 2002 February at OAO with HIDES-S. After a 10-yr observation, we released a giant planet of $M_{\rm p}\sin i = 3.0\ M_{\rm J}$ at $a = 2.1$ au, and a possible planet(s) at a wider orbit(s). We continued monitoring the star with HIDES-S, HIDES-F1, and HIDES-F2 at OAO until 2020 December and in total obtained 147 spectra with RVs.

We fitted the latest data with a single Keplerian model, and it yielded the orbital parameters for the known companion of $P = 696.26$ d, $K = 35.63$ m s^{-1}, and $e = 0.05$, with an rms scatter of 10.45 m s^{-1}. We then performed a periodogram analysis of the residuals and found possible peaks at round 307 and 1966 d (figure 2), which were close to those reported in Sato et al. (2012). Since the observation had a strong sampling window of 1 yr, and two periodic signals had the relation $1/307 \sim 1/365 + 1/1966$, we realized that the 307 d signal could be an alias of the 1966-d signal.

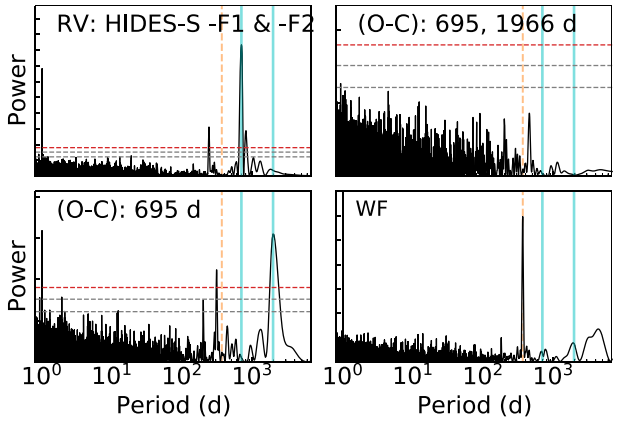


Fig. 2. GLS periodograms for 75 Cet. Top left: Observed RVs. Bottom left: RV residuals to the single Keplerian fitting of the inner planet. Top right: RV residuals to the 2-Keplerian fitting. Bottom right: window function of the observed RVs. The horizontal lines represent 10%, 1%, and 0.1% FAP levels from bottom to top. The vertical cyan solid lines indicate planetary signals, and the vertical orange dashed line indicates 1 yr.

We thus applied a double Keplerian model, and the orbit fitting yielded $P_{\rm b} = 696.62^{+1.33}_{-1.69}$ d, $K_{\rm b} = 36.92^{+1.09}_{-1.35}$ m s^{-1}, and $e_{\rm b} = 0.093^{+0.026}_{-0.042}$ for the inner known planet, and $P_{\rm c} = 2051.62^{+45.98}_{-40.47}$ d, $K_{\rm c} = 9.44^{+1.04}_{-1.39}$ m s^{-1}, and $e_{\rm c} = 0.023^{+0.191}_{-0.003}$. Adopting a stellar mass of $M_\star = 1.92\ M_\odot$, we obtained the minimum masses and semimajor axes $M_{\rm b}\sin i = 2.479\ M_{\rm J}$, $a_{\rm b} = 1.912$ au, and $M_{\rm c}\sin i = 0.912\ M_{\rm J}$, $a_{\rm c} = 3.929$ au, respectively (figure 3). The rms scatter of residuals of the double Keplerian model was suppressed to 10.45 m s^{-1}, and the periodogram did not show any significant signal (figure 2).

We used the scaling relation in Kjeldsen and Bedding (1995) to estimate the expected p-mode oscillation, based on the stellar parameters derived in this study. The amplitude obtained was approximately 6.4 m s^{-1}, which provides a plausible explanation for the rms of the residuals to the double Keplerian fitting. Additionally, we searched for regular variability corresponding to 696 and 2051 d in the BIS, which indicates line profiles, and Ca II index $S_{\rm H}$, but we did not find any. Thus we confirm the presence of an outer planet in the 75 Cet system.

Interestingly, only considering the gas giant planets, the configuration of the 75 Cet system is similar to our solar system. The mass ratio of the two gas giants in the 75 Cet system, assuming co-planarity, is $M_{\rm b}/M_{\rm c} = 2.72$, while their semimajor-axis ratio is $a_{\rm b}/a_{\rm S} = 0.487$. Notably, these values are comparable to those of Jupiter and Saturn in our own solar system, with a mass ratio of $M_{\rm J}/M_{\rm S} = 3.34$ and a semimajor-axis ratio of $a_{\rm J}/a_{\rm S} = 0.544$.

6 The online material is available in the supplementary data section of the online edition.

Downloaded from https://academic.oup.com/pasj/article/75/6/1030/7272944 by ANKARA user on 22 December 2023

Table 3. Orbital parameters.*

	P (d)	K (m s^{-1})	e	ω (rad)	T_p (JD−2450000)	$M_p \sin i$ (M_J)	a (au)	$\dot{\gamma}$ (m s^{-1} yr^{-1})	$\ddot{\gamma}$ (m s^{-1} yr^{-2})
HD 2952 b	$312.08^{+1.36}_{-1.69}$	$18.42^{+2.53}_{-2.43}$	$0.269^{+0.165}_{-0.150}$	$-2.715^{+0.600}_{-0.629}$	$4896.3^{+21.6}_{-48.0}$	$0.896^{+0.133}_{-0.125}$	$1.117^{+0.003}_{-0.004}$		
HD 4732 b	$371.74^{+0.72}_{-1.86}$	$46.80^{+4.78}_{-4.07}$	$0.266^{+0.081}_{-0.068}$	$1.093^{+0.169}_{-0.193}$	$5660.0^{+12.8}_{-14.5}$	$1.986^{+0.156}_{-0.154}$	$1.129^{+0.001}_{-0.004}$		
HD 4732 c	$3184.20^{+58.12}_{-57.60}$	$38.03^{+1.30}_{-3.15}$	$0.187^{+0.034}_{-0.066}$	$1.893^{+0.289}_{-0.231}$	$9459.3^{+138.8}_{-125.9}$	$3.365^{+0.116}_{-0.269}$	$4.725^{+0.057}_{-0.057}$		
HD 5608 b	$768.70^{+4.72}_{-1.67}$	$21.95^{+1.17}_{-1.14}$	$0.110^{+0.029}_{-0.080}$	$-1.604^{+0.268}_{-1.206}$	$3936.4^{+27.8}_{-721.7}$	$1.168^{+0.062}_{-0.057}$	$1.790^{+0.007}_{-0.003}$	$-5.138^{+0.167}_{-0.594}$	
HD 14067 b	$2725.81^{+13.12}_{-7.50}$	$100.17^{+4.17}_{-5.60}$	$0.701^{+0.023}_{-0.040}$	$1.787^{+0.090}_{-0.086}$	$5797.5^{+8.8}_{-11.8}$	$8.806^{+0.421}_{-0.387}$	$5.113^{+0.016}_{-0.009}$		
75 Cet b	$696.62^{+1.33}_{-1.69}$	$36.92^{+1.09}_{-1.35}$	$0.093^{+0.026}_{-0.042}$	$-2.750^{+5.513}_{-0.184}$	$5056.9^{+34.6}_{-60.5}$	$2.479^{+0.074}_{-0.090}$	$1.912^{+0.002}_{-0.003}$		
75 Cet c	$2051.62^{+45.98}_{-40.47}$	$9.44^{+1.04}_{-1.39}$	$0.023^{+0.191}_{-0.003}$	$2.147^{+2.737}_{-0.890}$	$4284.9^{+474.0}_{-765.7}$	$0.912^{+0.088}_{-0.143}$	$3.929^{+0.058}_{-0.052}$		
81 Cet b	$1005.57^{+1.84}_{-1.94}$	$58.51^{+1.39}_{-1.20}$	$0.037^{+0.015}_{-0.025}$	$-2.909^{+0.950}_{-0.628}$	$3458.4^{+106.0}_{-180.6}$	$3.307^{+0.078}_{-0.067}$	$2.104^{+0.003}_{-0.003}$		
ϵ Tau b	$585.82^{+0.26}_{-0.33}$	$93.24^{+0.74}_{-0.73}$	$0.076^{+0.009}_{-0.008}$	$1.883^{+0.119}_{-0.106}$	$3492.3^{+11.3}_{-10.0}$	$7.190^{+0.056}_{-0.056}$	$1.878^{+0.001}_{-0.001}$		
HD 32518 b	$157.35^{+0.10}_{-0.08}$	$98.88^{+5.60}_{-5.88}$	$0.028^{+0.034}_{-0.019}$	$-0.618^{+1.876}_{-1.244}$	$4375.2^{+108.3}_{-6.5}$	$2.849^{+0.160}_{-0.171}$	$0.594^{+0.000}_{-0.000}$		
6 Lyn b	$919.86^{+1.92}_{-3.71}$	$32.76^{+0.67}_{-1.52}$	$0.042^{+0.024}_{-0.032}$	$2.111^{+1.540}_{-1.077}$	$3537.3^{+121.2}_{-224.7}$	$1.881^{+0.038}_{-0.089}$	$2.028^{+0.003}_{-0.005}$		
HD 47366 b	$360.08^{+0.27}_{-0.72}$	$40.15^{+1.97}_{-2.20}$	$0.071^{+0.030}_{-0.046}$	$-2.654^{+5.231}_{-0.143}$	$5308.7^{+24.4}_{-68.8}$	$2.082^{+0.099}_{-0.113}$	$1.207^{+0.001}_{-0.002}$		
HD 47366 c	$677.53^{+1.29}_{-1.16}$	$24.02^{+1.18}_{-1.08}$	$0.161^{+0.045}_{-0.041}$	$2.856^{+0.163}_{-0.525}$	$3950.3^{+16.5}_{-54.0}$	$1.522^{+0.072}_{-0.070}$	$1.840^{+0.002}_{-0.002}$		
o Uma b	$1569.81^{+12.76}_{-13.59}$	$33.11^{+1.64}_{-2.77}$	$0.149^{+0.044}_{-0.079}$	$0.712^{+0.539}_{-0.374}$	$3348.8^{+132.6}_{-84.1}$	$3.651^{+0.176}_{-0.298}$	$3.691^{+0.020}_{-0.021}$		
4 Uma b	$270.27^{+0.24}_{-0.09}$	$242.24^{+7.45}_{-14.31}$	$0.453^{+0.021}_{-0.036}$	$0.499^{+0.055}_{-0.094}$	$5958.1^{+2.3}_{-4.1}$	$7.902^{+0.199}_{-0.378}$	$0.877^{+0.001}_{-0.000}$		
41 Lyn b	$183.93^{+0.09}_{-0.09}$	$56.42^{+1.87}_{-1.88}$	$0.040^{+0.022}_{-0.031}$	$-0.252^{+1.158}_{-1.099}$	$4354.4^{+80.2}_{-16.9}$	$1.654^{+0.054}_{-0.055}$	$0.648^{+0.000}_{-0.000}$		
HD 104985 b	$199.68^{+0.09}_{-0.07}$	$169.06^{+3.33}_{-3.74}$	$0.047^{+0.015}_{-0.028}$	$2.336^{+0.581}_{-0.488}$	$5083.5^{+17.7}_{-16.1}$	$5.559^{+0.110}_{-0.122}$	$0.715^{+0.000}_{-0.000}$		
11 Com b	$323.21^{+0.06}_{-0.05}$	$288.63^{+2.39}_{-2.37}$	$0.238^{+0.007}_{-0.007}$	$1.594^{+0.030}_{-0.031}$	$4519.4^{+1.5}_{-1.6}$	$15.464^{+0.123}_{-0.125}$	$1.178^{+0.000}_{-0.000}$		
HD 120084 b	$2134.79^{+8.08}_{-13.31}$	$40.50^{+1.88}_{-2.04}$	$0.478^{+0.035}_{-0.034}$	$1.902^{+0.130}_{-0.092}$	$4965.7^{+29.1}_{-19.3}$	$3.762^{+0.156}_{-0.188}$	$4.192^{+0.011}_{-0.017}$		
24 Boo b	$30.33^{+0.00}_{-0.01}$	$55.67^{+2.31}_{-2.66}$	$0.032^{+0.039}_{-0.023}$	$-3.128^{+1.559}_{-1.666}$	$5129.2^{+3.0}_{-15.4}$	$0.883^{+0.036}_{-0.043}$	$0.194^{+0.000}_{-0.000}$		
o CrB b	$187.01^{+0.15}_{-0.16}$	$33.56^{+1.71}_{-2.16}$	$0.105^{+0.036}_{-0.079}$	$0.771^{+0.742}_{-0.837}$	$4443.7^{+27.8}_{-18.9}$	$1.120^{+0.057}_{-0.071}$	$0.699^{+0.000}_{-0.000}$		
γ Lib b	$414.88^{+1.24}_{-1.47}$	$21.17^{+1.94}_{-2.01}$	$0.160^{+0.071}_{-0.107}$	$-2.962^{+5.754}_{-0.086}$	$5020.3^{+23.7}_{-86.3}$	$1.126^{+0.101}_{-0.108}$	$1.319^{+0.003}_{-0.003}$		
γ Lib c	$966.49^{+2.27}_{-1.96}$	$73.38^{+1.75}_{-2.02}$	$0.065^{+0.033}_{-0.022}$	$2.663^{+0.453}_{-0.366}$	$5563.8^{+67.6}_{-56.7}$	$5.231^{+0.120}_{-0.147}$	$2.318^{+0.004}_{-0.003}$		
ω Ser b	$278.59^{+0.80}_{-0.61}$	$23.11^{+1.94}_{-3.38}$	$0.180^{+0.066}_{-0.127}$	$2.499^{+0.600}_{-1.272}$	$5022.3^{+20.1}_{-63.7}$	$0.736^{+0.060}_{-0.106}$	$0.838^{+0.002}_{-0.001}$		
κ CrB b	$1253.68^{+3.07}_{-6.48}$	$23.78^{+0.52}_{-0.99}$	$0.040^{+0.013}_{-0.032}$	$3.099^{+4.617}_{-7.392}$	$1743.5^{+181.3}_{-633.1}$	$1.522^{+0.033}_{-0.065}$	$2.500^{+0.004}_{-0.009}$	$0.518^{+0.033}_{-0.316}$	
HD 145457 b	$176.13^{+0.18}_{-0.20}$	$66.46^{+3.12}_{-2.65}$	$0.111^{+0.039}_{-0.040}$	$-0.848^{+0.516}_{-0.490}$	$3347.1^{+19.7}_{-10.2}$	$2.794^{+0.132}_{-0.117}$	$0.762^{+0.001}_{-0.001}$		
ν Oph b	$529.93^{+0.08}_{-0.07}$	$287.60^{+1.19}_{-0.74}$	$0.126^{+0.003}_{-0.004}$	$0.164^{+0.028}_{-0.021}$	$1506.0^{+2.3}_{-1.8}$	$21.548^{+0.092}_{-0.056}$	$1.765^{+0.000}_{-0.000}$		
ν Oph c	$3180.60^{+5.01}_{-4.52}$	$175.47^{+1.57}_{-1.02}$	$0.179^{+0.007}_{-0.005}$	$0.149^{+0.033}_{-0.034}$	$-114.1^{+16.6}_{-17.6}$	$23.693^{+0.205}_{-0.139}$	$5.829^{+0.006}_{-0.006}$		
HD 167042 b	$417.67^{+0.43}_{-0.41}$	$30.52^{+0.70}_{-0.95}$	$0.010^{+0.033}_{-0.004}$	$0.950^{+1.213}_{-2.358}$	$2935.5^{+136.9}_{-65.6}$	$1.397^{+0.031}_{-0.044}$	$1.220^{+0.001}_{-0.001}$	$1.361^{+0.230}_{-0.291}$	
HD 173416 b	$322.03^{+1.33}_{-1.52}$	$35.33^{+4.07}_{-4.46}$	$0.208^{+0.089}_{-0.094}$	$-2.058^{+0.589}_{-0.578}$	$4735.0^{+23.4}_{-253.1}$	$1.841^{+0.206}_{-0.225}$	$1.158^{+0.003}_{-0.004}$		
HD 175679 b	$1357.64^{+1.74}_{-2.04}$	$378.37^{+3.51}_{-5.65}$	$0.386^{+0.011}_{-0.007}$	$-0.222^{+0.019}_{-0.031}$	$3274.6^{+4.4}_{-6.1}$	$36.868^{+0.337}_{-0.626}$	$3.341^{+0.003}_{-0.003}$		
HD 180314 b	$394.73^{+0.13}_{-0.13}$	$343.39^{+3.83}_{-3.92}$	$0.247^{+0.009}_{-0.009}$	$-0.982^{+0.044}_{-0.044}$	$3570.6^{+2.4}_{-2.4}$	$22.707^{+0.252}_{-0.255}$	$1.448^{+0.000}_{-0.000}$		
ξ Aql b	$136.97^{+0.11}_{-0.18}$	$53.07^{+2.69}_{-4.72}$	$0.059^{+0.087}_{-0.037}$	$-0.000^{+1.857}_{-0.040}$	$3001.0^{+46.7}_{-2.1}$	$1.941^{+0.091}_{-0.179}$	$0.625^{+0.000}_{-0.001}$		
18 Del b	$982.85^{+1.06}_{-0.92}$	$114.96^{+1.98}_{-0.96}$	$0.024^{+0.007}_{-0.018}$	$1.119^{+0.503}_{-1.012}$	$4356.1^{+102.9}_{-118.2}$	$9.207^{+0.160}_{-0.077}$	$2.476^{+0.002}_{-0.002}$	$-1.291^{+0.377}_{-0.473}$	$0.177^{+0.052}_{-0.069}$
HD 208897 b	$358.27^{+0.87}_{-1.50}$	$29.45^{+1.25}_{-1.04}$	$0.020^{+0.049}_{-0.010}$	$-1.981^{+2.815}_{-0.084}$	$6178.2^{+4.7}_{-311.4}$	$1.194^{+0.049}_{-0.044}$	$1.063^{+0.002}_{-0.003}$	$4.073^{+0.441}_{-0.825}$	
HD 210702 b	$355.50^{+0.38}_{-0.61}$	$36.11^{+1.46}_{-1.27}$	$0.071^{+0.019}_{-0.051}$	$1.962^{+0.858}_{-0.447}$	$2189.9^{+40.9}_{-28.5}$	$1.515^{+0.062}_{-0.053}$	$1.079^{+0.001}_{-0.001}$		
14 And b	$186.76^{+0.11}_{-0.12}$	$86.08^{+2.76}_{-2.95}$	0 (fixed)	0 (fixed)	$2853.0^{+2.1}_{-2.1}$	$3.559^{+0.114}_{-0.122}$	$0.775^{+0.000}_{-0.000}$		

*These parameters are derived with only RV data. Here $\dot{\gamma}$ (m s^{-1} yr^{-1}) and $\ddot{\gamma}$ (m s^{-1} yr^{-2}) are the linear trend and quadratic trend, respectively. The newly confirmed planet (75 Cet c) is marked in bold text.

Downloaded from https://academic.oup.com/pasj/article/75/6/1030/7272944 by ANKARA user on 22 December 2023

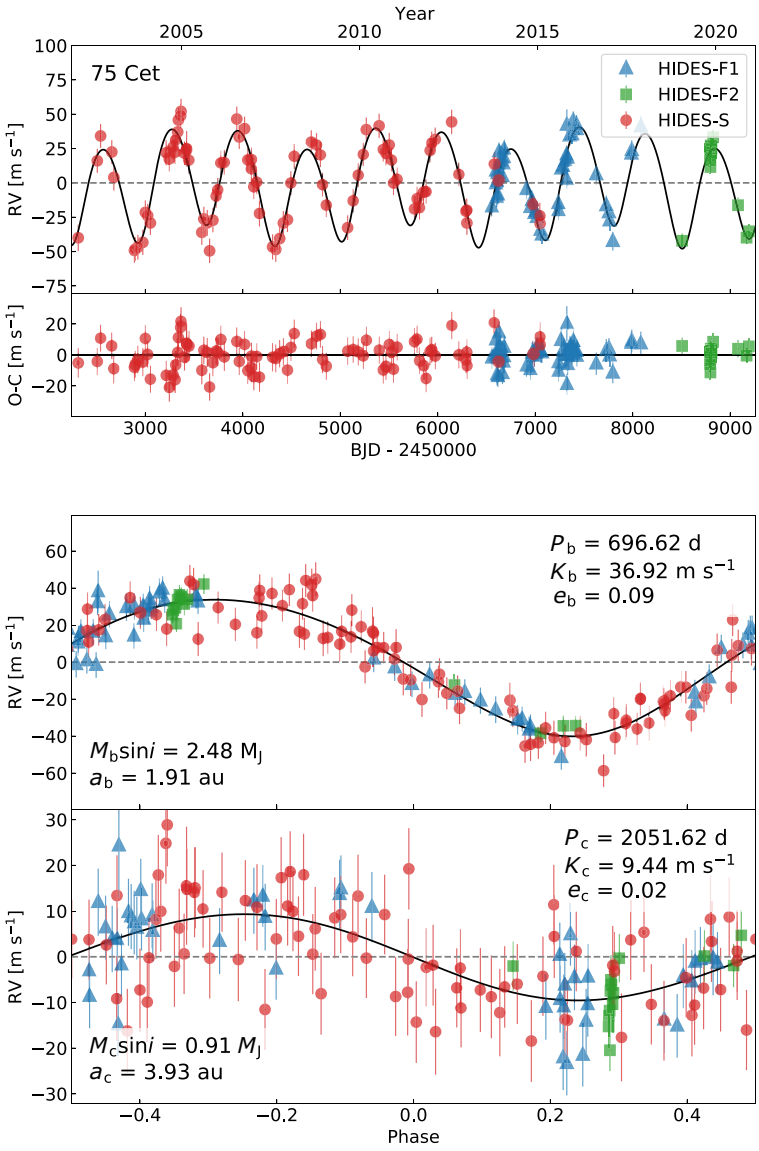


Fig. 3. Double Keplerian solution to 75 Cet. Top: Best-fit double Keplerian curve in the full observation span, including fitted RV offsets between instruments and jitters that are included in the error bars. Middle: Residuals of the RVs with respect to the best-fit model. Bottom: Phase-folded orbits of planets b and c. Data taken by HIDES-S, HIDES-F1, and HIDES-F2 using the 1.88 m telescope at OAO are shown with red circles, blue triangles, and green squares, respectively.

75 Cet c, defined as a planet around an evolved star, having a mass of approximately $1M_J$ and an orbital separation of around $\gtrsim 4$ au, adds to a population of planets of which we currently have only two other examples with comparable properties: BD +49 828 b, which orbits a giant star with a mass of 1.6 $M_\odot$ at a distance of 4.2 au and has a minimum mass of 1.6 M_J (Niedzielski et al. 2015b), and HD 25723 c, which orbits a giant star with a mass of 2.12 $M_\odot$ at a distance of 4.35 au and has a minimum mass of 1.33 M_J (Tala Pinto et al. 2020). The shortage of planets like 75 Cet c is currently unclear, and this might be due to the selection effect because these planets are always hard to confirm due to the necessity of a decades-long observational baseline.

4.3 RV long-term trend

Our best fits showed that five stars have significant RV accelerations over decades, i.e., the RV long-term trend. Four of the five, including HD 5608, κ CrB, HD 167042, and HD 208897, showed a linear trend, and their best-fit orbits are shown in table 3 and figure 4. The slope of the RV trend can be used for estimating the minimum of the dynamical mass of the outer body (Winn et al. 2009):

$$\frac{M_c \sin i_c}{a_c^2} \sim \frac{\dot{\gamma}}{G}. \quad (2)$$

Downloaded from https://academic.oup.com/pasj/article/75/6/1030/7272944 by ANKARA user on 22 December 2023

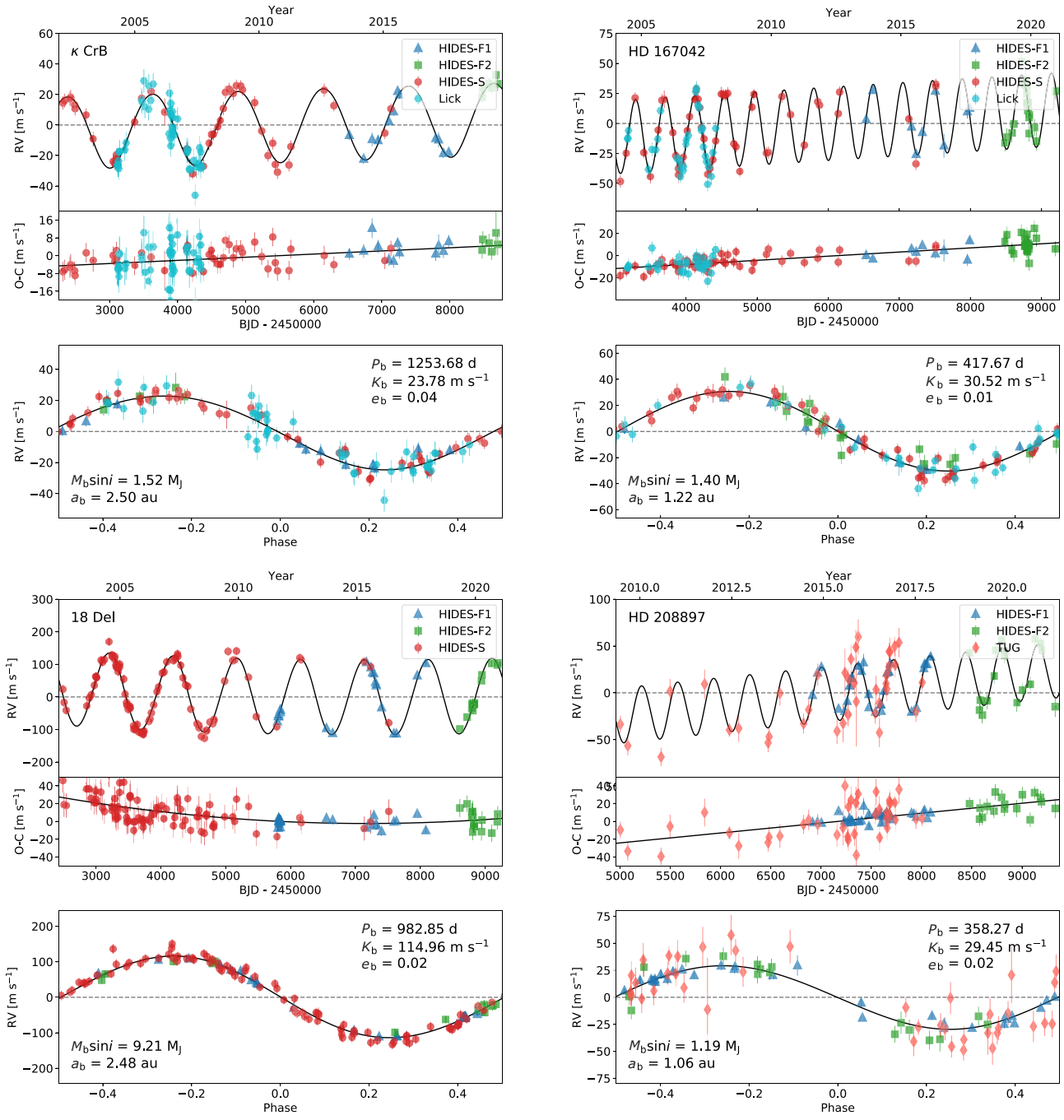


Fig. 4. Keplerian orbital fits to κ CrB, HD 167042, 18 Del, and HD 208897. For each panel, the top subplot displays the best-fit 1-Keplerian curve in the full observation span, including fitted RV offsets between instruments and jitters that are included in the error bars; the middle subplot displays residuals of the RVs with respect to the best-fit model; and the bottom subplot displays the phase-folded orbit of the planet. Data taken by HIDES-S, HIDES-F1, and HIDES-F2 using the 1.88 m telescope at OAO are shown with red circles, blue triangles, and green squares, respectively. Data taken by the Hamilton echelle spectrograph on the Coudé Auxiliary Telescope at the Lick Observatory (Lick) are shown with cyan hexagons, while the data taken by the Coude echelle spectrograph on the 1.5 m Russian-Turkish Telescope at TUG are shown with red diamonds.

Here $\dot{\gamma}$ is the RV acceleration, M_c is the mass of the outer companion, i_c is the orbital inclination, G is the gravitational constant, and a_c is the semimajor axis of the outer companion. Assuming (near) circular orbits for the outer companions, the RV linear acceleration trend could be assumed to be at least half of the orbit. Our observation baselines are approximately 20 yr, and the stars are more massive than 1 $M_\odot$. Thus, the prospective outer planets should reside over ~10 au away from the central star.

Another one of the five, 18 Del, displayed a significant turning point at around JD 2457000 in the RV curve, and we derived a best-fit orbit; see table 3 and figure 4. To

Downloaded from https://academic.oup.com/pasj/article/75/6/1030/7272944 by ANKARA user on 22 December 2023

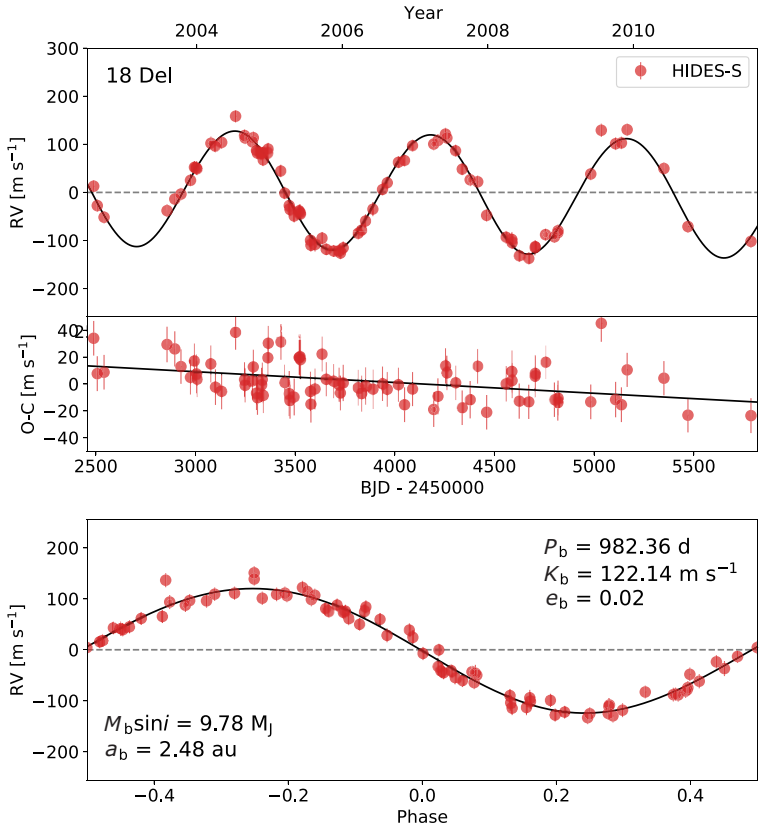


Fig. 5. Single Keplerian solution to 18 Del using RVs obtained by HIDES-S earlier than JD 2456000. Top: Best-fit single Keplerian curve. Middle: residuals of the RVs with respect to the best-fit model. Bottom: Phase-folded orbit of the planet.

estimate the mass of a prospective outer companion, a linear acceleration or deceleration should be determined. Thus, we divided the RV time series into acceleration and deceleration sides. Notably, the deceleration side provided a longer baseline and contained more data points predominantly taken by HIDES-S. We performed a Keplerian orbital fit with HIDES-S data showing deceleration (observation earlier than JD 2456000), and it consequently yielded a value of $\dot{\gamma} = -2.922$ m s^{-1} yr^{-1} (figure 5).

Given the slopes, we derived $(M_c \sin i_c)/a_c^2$ values of -0.029, 0.003, 0.008, -0.016, and 0.023 for HD 5608, κ Crb, HD 167042, 18 Del, and HD 208897, respectively. We present the correlation between mass and the semimajor axis in figure 6.

Among the five stars, HD 5608 has been confirmed to possess a low-mass stellar companion through imaging detection, as reported by Ryu et al. (2016). Because of our intention to present a joint fit using RV, relative astrometry, and direct imaging for this system in section 6, we will not elaborate on it in this section. Conversely, the remaining four systems were not reported to have outer companions, with κ CrB and 18 Del subjected to imaging attempts by Bonsor et al. (2013) and Ryu et al. (2016), respectively.

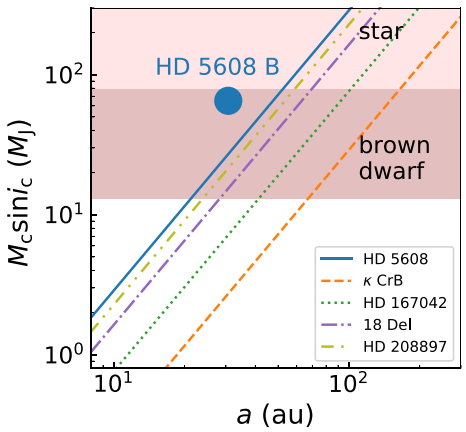


Fig. 6. Mass of the prospective outer companion as a function of the semimajor axis. HD 5608, κ Crb, HD 167042, and HD 208897 are represented with different line styles, and we specifically mark the confirmed companion HD 5608 B in this figure. The upper light shaded area indicates the stellar regime, while the middle dark shaded area indicates the brown dwarf regime.

Despite the non-detection, some estimates on κ CrB and 18 Del were given according to the observations. In particular, Bonsor et al. (2013) used adaptive optic imaging and the RV trend to impose a mass-separation constraint and

Downloaded from https://academic.oup.com/pasj/article/75/6/1030/7272944 by ANKARA user on 22 December 2023

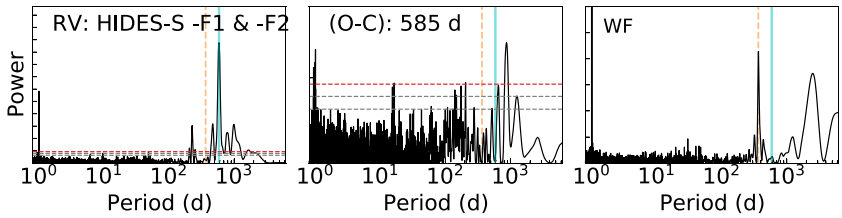


Fig. 7. GLS periodograms for ϵ Tau. From left to right: Observed RVs, RV residuals to the single Keplerian fitting of the known planet, and the window function of the observed RVs. The horizontal lines represent 10%, 1%, and 0.1% FAP levels from bottom to top. The vertical cyan solid lines indicate planetary signals and the vertical orange dashed line indicates 1 yr.

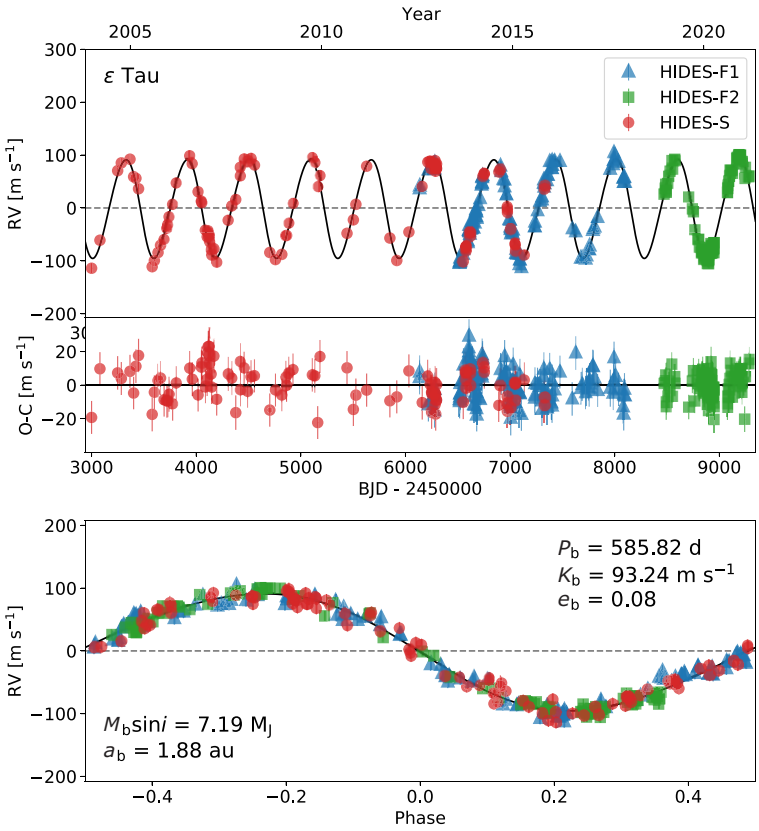


Fig. 8. Single Keplerian solution to ϵ Tau. Top: Best-fit single Keplerian curve in the full observation span, including fitted RV offsets between instruments and jitters that are included in the error bars. Middle: residuals of the RVs with respect to the best-fit model. Bottom: Phase-folded orbit of the planet. Data taken by HIDES-S, HIDES-F1, and HIDES-F2 using the 1.88 m telescope at OAO are shown with red circles, blue triangles, and green squares, respectively.

put forth three possible scenarios for κ CrB. Moreover, they formulated three disk scenarios based on their constraint and resolved images from the Hershel spacecraft. However, it is possible that the previously established constraints for the potential outer companion were overestimated. By incorporating our latest RV trend and updated stellar properties, we revised the estimation, which may in turn require modifications to the three proposed scenarios for κ CrB.

(1) All three scenarios require an outer companion with a minimum mass of 0.63 M_J and a semimajor axis wider than 14.7 au.

(2) In scenario 1, which involves a wide belt ranging from 20 to 220 au, the presence of an outer companion can only be supported within the narrow range of 14.7 to 20 au.

(3) In scenario 2, which consists of two narrow belts at 40 and 165 au, the survival of the outer companion depends on its location relative to the two belts. If it exists inside the inner belt, it must be situated between 14.7 and 40 au. If it exists between the two belts, it must have a mass of at least 4.9 M_J. Additionally, based on the RV trend and assuming an upper limit of 40 M_J

Downloaded from https://academic.oup.com/pasj/article/75/6/1030/7272944 by ANKARA user on 22 December 2023

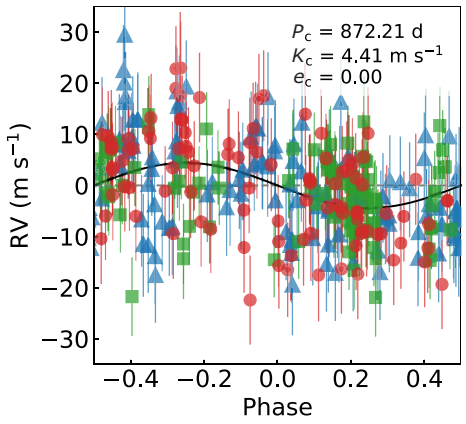


Fig. 9. Phase-folded curve of the regular 872-d variation in ϵ Tau RVs. The symbols are the same as those in figure 8.

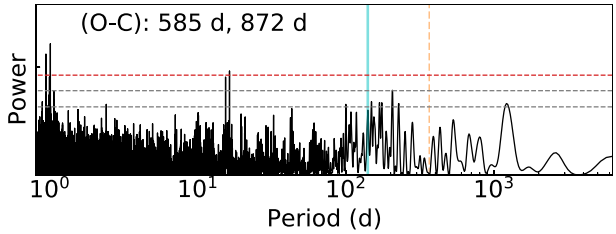


Fig. 10. GLS periodograms of ϵ Tau RVs with the removal of the known planet and regular 872-d variation. The horizontal lines represent 10%, 1%, and 0.1% FAP levels from bottom to top. The vertical cyan solid line indicates the planetary signal, and the vertical orange dashed line indicates 1 yr.

for the outer companion's mass beyond 70 au, we estimate that the outer companion must be situated within approximately 125 au to avoid affecting the stability of the inner belt.

(4) In scenario 3, which involves a stirred disk with dust peaking at 83 au, the disk can be stirred out to 53 au by the inner body. We also apply equation 15 from Mustill and Wyatt (2009) to demonstrate that the outer companion's influence on the disk is negligible if it is located very close to the host star, with a minimum mass of 0.63 M_J and a radial distance of 14.7 au, and an orbit characterized by an extremely low eccentricity of less than 0.003. Although we cannot exclude this unlikely situation, the probability of it occurring is relatively low in this scenario.

18 Del was reported to harbor a distant companion 18 Del B (Mugrauer et al. 2014) outside the field of view of the HiCIAO frame (Ryu et al. 2016). The projected separation of 18 Del B is 2199 au and its mass is 0.19 $M_\odot$. Based on the mass separation relation shown in figure 6, it can be confidently concluded that 18 Del B does not contribute to the observed trend. An upper mass limit as a function of separation with an inner orbital boundary was obtained from imaging observation by Ryu et al. (2016), Their results indicated that, if present, the companion should have a maximum mass of approximately 300 M_J and a minimum mass of approximately 4 M_J at 10 au for the inner most, and 90 M_J at 50 au for the outer most, suggesting that it could be a high-mass planet, brown dwarf, or low-mass stellar companion.

5 Noteworthy systems

5.1 ϵ tau: additional RV variations

ϵ Tau (HD 28305, HR 1409, HIP 20889) is a K0 giant star in the nearest open cluster, the Hyades cluster, and its planet is the first one ever discovered in an open cluster. We started to collect data in 2003 December, and we released the discovery of the planet after 20 data points in Sato et al. (2007). We continued the follow-up observation with HIDES-S, HIDES-F1, and HIDES-F2 until 2021 March and in total obtained 386 spectra with RVs.

We fitted the data with a single Keplerian model, and it yielded the orbital parameters for the companion of $P = 585.82^{+0.26}_{-0.33}$ d, $K = 93.24^{+0.74}_{-0.73}$ m s^{-1}, and $e = 0.076^{+0.009}_{-0.008}$. Adopting a stellar mass of $M_\star = 2.57\ M_\odot$, we obtained the companion mass of $M_p \sin i = 7.194\ M_J$ and a semimajor axis of $a = 1.878$ au. The rms scatter of the single Keplerian fitting was 9.33 m s^{-1}.

As seen in figure 7, the RV residuals to the single Keplerian fitting (figure 8) exhibit a distinct regular variation at 872 d with FAP apparently lower than 0.1%, suggesting a possible outer companion in the system. We thus performed a double Keplerian fit to the RV system, with the eccentricity of the possible outer companion equal to 0. Consequently, we obtained $P = 872.21$ d and $K = 4.41$ m s^{-1} (figure 9), referring to a minimum mass of $M_p \sin i = 0.326\ M_J$ and a semimajor axis of $a = 2.28$ au. The rms scatter of the 2-Keplerian model was suppressed to ~ 8.69 m s^{-1} (decreased by ~ 0.64 m s^{-1}).

After the subtraction of an 872-d variation, another two independent signals, respectively at periods of 16 and 15 d, remained in the residuals with FAP slightly lower than 0.1% (figure 10). They can be interpreted by sinusoidal curves with periods of $P = 16.31$ d and $P = 15.34$ d, and semi-amplitudes of $K = 3.70$ m s^{-1} and $K = 3.33$ m s^{-1}. With the subtraction of 16- and 15-d variations, the rms scatter was further suppressed to $\sim$7.83 m s^{-1} (by ~ 0.86 m s^{-1}) compared to the double Keplerian model with $P = 585$ d and $P = 872$ d.

The solar-like oscillation and instrumental jitter could be responsible for the remaining rms scatter. According to the scaling relation in Kjeldsen and Bedding (1995), the oscillation amplitude for ϵ Tau is approximately 7 m s^{-1}.

Downloaded from https://academic.oup.com/pasj/article/75/6/1030/7272944 by ANKARA user on 22 December 2023

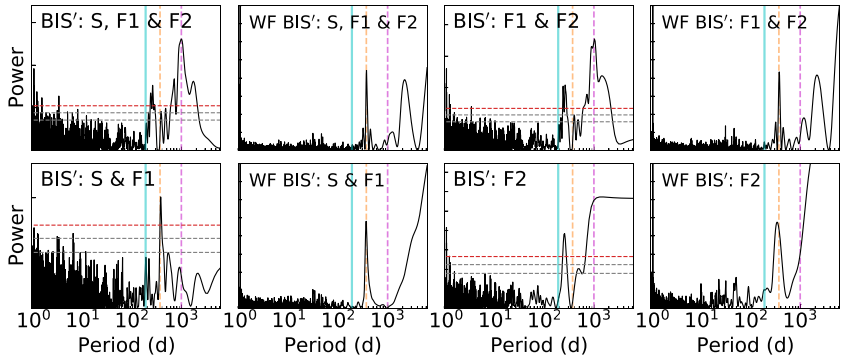


Fig. 11. GLS periodograms of BIS′ of ϵ Tau (left panels) and the observational window functions (right panels). BIS′ calculated by data taken from HIDES-S, HIDES-F1, and HIDES-F2 are represented by S, F1, and F2, respectively. The horizontal lines represent 10%, 1%, and 0.1% FAP levels from bottom to top. The vertical cyan solid line indicates the planetary signal, the vertical orange dashed line indicates 1 yr, and the vertical magenta dashed line indicates the BIS′ signal introduced by HIDES-F2.

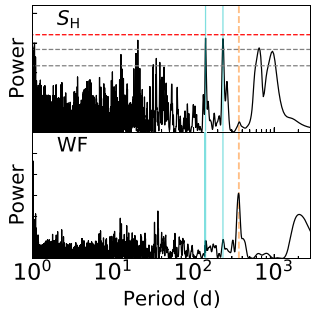


Fig. 12. GLS periodograms of S_H of ϵ Tau. The horizontal lines represent 10%, 1%, and 0.1% FAP levels from bottom to top. The vertical cyan solid lines indicate the focused signals at 141 and 232 d, respectively, in the S_H time series, and the vertical orange dashed line indicates 1 yr.

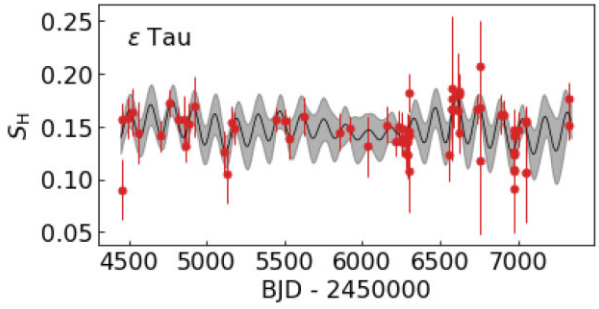


Fig. 13. GP results of S_H of ϵ Tau. The red circles with error bars are S_H measurements taken by HIDES-S. The solid black line is the GP prediction, with its error shown in gray.

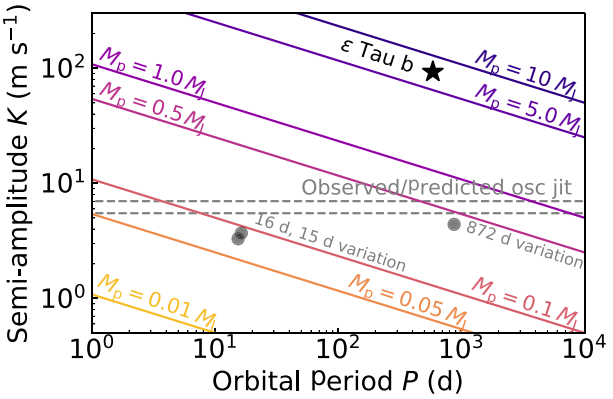


Fig. 14. Detectability of a planet orbiting ϵ Tau. The colored solid lines indicate the orbital period against the RV semiamplitude of planets having different masses. The known planet is shown with a black star, and three regular variations in the RV residuals are shown with gray circles. The RV semiamplitudes of observed and predicted oscillation jitters of ϵ Tau are shown with dashed gray lines.

Ando et al. (2010) first detected oscillations in this star based on a few days of RV observations; Stello et al. (2017) then obtained consistent results with their data. Arentoft et al. (2019) reported intensive observations of the solar-like oscillation with over 4800 spectra. The filtered RV data in Arentoft et al. (2019) have an rms scatter of 5.38 m s^{-1}. Considering the instrumental jitter of HIDES ($\lesssim$ 4.5 m s^{-1}: Teng et al. 2022a and this work), solar-like oscillation and instrumental jitter could be a plausible explanation for the rms scatter.

In order to investigate the true scenario for additional regular variations in the RV time series, we calculated the GLS periodograms to the BIS, BIS′, and Ca II H index S_H. The periodogram to BIS′ exhibited a strong 990-d signal, which was then confirmed to be caused by HIDES-F2 (figure 11). The periodogram to BIS′ of HIDES-S and HIDES-F1 did not illustrate periodicity relevant to periods of RV variations. Therefore, the 872-d variation, which exhibits the strong power in the periodogram to the 1-Keplerian model, can be considered a dubious planetary signal. However, the 16- and 15-d variations, which show relatively weak power in the periodogram of the 2-Keplerian model, are more likely to be instrumental or intrinsically from the star.

The periodogram to S_H exhibited two possible periods with almost the same power at 141 and 232 d, respectively (figure 12). Considering the strong window function effect

Downloaded from https://academic.oup.com/pasj/article/75/6/1030/7272944 by ANKARA user on 22 December 2023

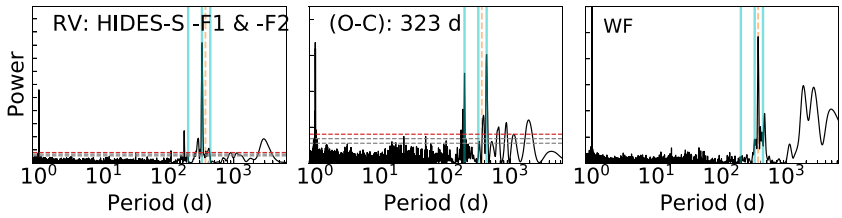


Fig. 15. GLS periodograms for 11 Com. From left to right: Observed RVs, RV residuals to the single Keplerian fitting of the known substellar companion, and the window function of the observed RVs. The horizontal lines represent 10%, 1%, and 0.1% FAP levels from bottom to top. The vertical cyan solid line indicates the focused periodic signal, including a planetary signal at 323 d and two significant signals in the residuals at 198 and 434 d, respectively, and the vertical orange dashed line indicates 1 yr.

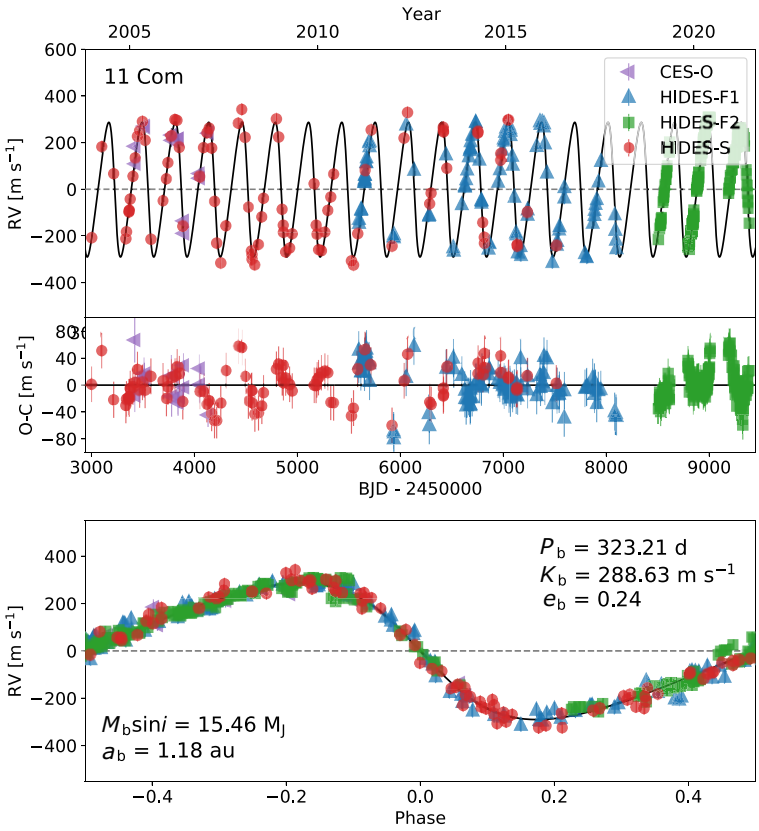


Fig. 16. Single Keplerian solution to 11 Com. Top: Best-fit 1-Keplerian curve in the full observation span, including fitted RV offsets between instruments and jitters that are included in the error bars. Middle: Residuals of the RVs with respect to the best-fit model. Bottom: Phase-folded orbit of the planet. Data taken by HIDES-S, HIDES-F1, and HIDES-F2 using the 1.88 m telescope at OAO are shown with red circles, blue triangles, and green squares, respectively, and data taken by CES-O on the 2.16 m telescope at Xinglong Observatory are shown with purple triangles.

at 1 yr, one should be the true signal and possibly refer to the rotation of the star, and the other one should be the alias ($1/141 - 1/232 \simeq 1/365$). Adopting the projected rotational velocity of $v \sin i = 3.52$ km s^{-1} (Takeda et al. 2008), the maximum rotational period should be around 177 d. This suggests 141 d is more likely to be the true rotational period.

Schröder et al. (2020) investigated the magnetic activity of four giant stars in the Hyades cluster by Ca II H&K emission. They estimated the rotational periods of three of them (γ Tau, δ Tau, and θ^1 Tau) using the Gaussian process (GP) and adopted rotational periods of around 140 d for these three giants. However, they did not determine the rotational period of ϵ Tau.

In our work, we performed GP to HIDES S_H data of ϵ Tau. We adopted the same GP kernel as in Schröder et al. (2020), the *celerite* approximation (Foreman-Mackey et al. 2017), but set a uniform prior between 100 and 200 d to the period. The formulation is

$$k(\tau) = \frac{B}{2+C} e^{-\tau/L} \left[\cos\left(\frac{2\pi\tau}{P_{\rm rot}}\right) + (1+C) \right], \quad (3)$$

Downloaded from https://academic.oup.com/pasj/article/75/6/1030/7272944 by ANKARA user on 22 December 2023

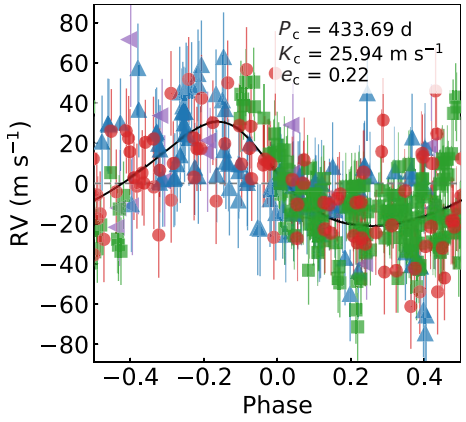


Fig. 17. Phase-folded curve of the regular 434-d variation in 11 Com RVs. The symbols are the same as those in figure 16.

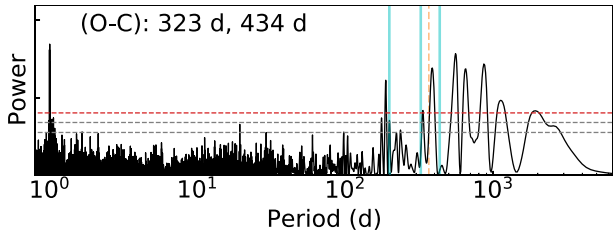


Fig. 18. GLS periodograms of 11 Com RVs with removal of the known substellar companion and regular 434-d variation. The horizontal lines represent 10%, 1%, and 0.1% FAP levels from bottom to top. The vertical cyan solid line indicates the focused signals, including a planetary signal at 323 d and two significant signals in the residuals at 198 and 434 d, and the vertical orange dashed line indicates 1 yr.

where k is the covariance matrix, τ is the time difference, B and C are normalization constants, L describes the lifetime of the features, and $P_{\rm rot}$ is the desired rotational period.

Considering the inactiveness of the Ca II H&K emission with a low amplitude of $S_{\rm H}$ variation, we set factor C by eye in the GP kernel equal to 0. As a result, we obtained a rotational period of 141.1 d (figure 13), which is close to the rotational periods of the other three giant stars, i.e., γ Tau, δ Tau, and θ^1 Tau. Here, we also note that either 141 or 232 d revealed by the periodogram of $S_{\rm H}$ is contradictory to the estimation of Schröder et al. (2020) of a minimal rotational period of 350 d based on the scaling relation in Mittag, Schmitt, and Schröder (2018).

The long-baseline monitoring of the host star aims at searching for an additional companion. In figure 14, we present the RV semiamplitude against the orbital period with hypothetical planets of different masses. Based on existing data, regular variation with a semiamplitude of ~ 4 m s^{-1} can be detected, and there is no long-term trend in the RV time series. Figure 14 also suggests that we may not find any Jupiter-mass planet surviving around ϵ Tau by RVs. However, the instrumental jitter of HIDES is close to 4 m s^{-1}; therefore, less massive close-in planets, if they exist, are probably hidden in the jitter. In addition, for a giant star like ϵ Tau with $R_\star > 10\ R_\odot$, it is also hard to detect a close-in planet with photometry, since the transit depth for a Jupiter-like planet would be lower than 0.0001.

5.2 11 Com: additional regular RV variations

11 Com (HD 107383, HR 4697, HIP 60202) is a G8 III star and reported to harbor a substellar companion in Liu et al. (2008). We started observations of 11 Com at OAO with HIDES-S in 2003 December. After its RV variations were detected, we then started observation of this star with CES-O at Xinglong in 2005 to confirm the variations of the star independently. We continued monitoring the star after the report of the companion at OAO with HIDES-S, HIDES-F1, and HIDESF2 until 2021 June and in total obtained 415 spectra with RVs.

We fitted the data with a single Keplerian model, and it yielded the orbital parameters for the companion of $P = 323.21^{+0.06}_{-0.05}$ d, $K = 288.63^{+2.39}_{-2.37}$ m s^{-1}, and $e = 0.238^{+0.007}_{-0.007}$. Adopting a stellar mass of $M_\star = 2.09\ M_\odot$, we obtained the companion mass of $M_{\rm p}\sin i = 15.464\ M_{\rm J}$ and a semimajor axis of $a = 1.178$ au. The rms scatter of the single Keplerian fitting was 24.70 m s^{-1}.

As illustrated in figure 15, the RV residuals to the single Keplerian fitting (figure 16) exhibited periodic variations at 198 and 434 d, suggesting a possible inner or outer companion(s). Considering the strong power at 1 yr in the window function, the 198-d signal could be an alias of the 434-d signal ($1/198 \simeq 1/434 + 1/365$). We thus applied a double Keplerian fit with the known companion fixed to its best-fit orbital parameters. Consequently, the rms scatter was suppressed to 20.21 m s^{-1} (decreased by 4.49 m s^{-1}), and we obtained $P = 433.69$ d, $K = 25.94$ m s^{-1}, $e = 0.220$, $M_{\rm p}\sin i = 1.513\ M_{\rm J}$, and $a = 1.43$ au (figure 17). Nevertheless, prominent signals persist in the periodogram of the residuals at periods of several hundred days (figure 18).

However, the double planet scenario can be hardly feasible since the strong interaction between the two companions could make the system dynamically unstable. We tested the dynamical stability with `MERCURY6` integrator code (Chambers 1999). The integrator was initiated using the RV-derived orbital parameters of the inner companion, under the assumption of the co-planarity and prograde motion of the outer companion. Consequently, the system always dissipated quickly and never kept stable from the RV-derived initials. The inner companion (11 Com b) is highly massive, which could clear up the neighboring area so that the existence of either an outer planet or an inner companion with short separation should be doubtful. To comprehensively investigate the stability of the system, it is necessary to perform simulations across a wider

Downloaded from https://academic.oup.com/pasj/article/75/6/1030/7272944 by ANKARA user on 22 December 2023

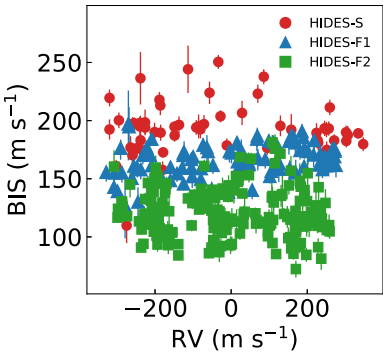


Fig. 19. BIS against RVs of 11 Com. The data are taken by HIDES-S, HIDES-F1, and HIDES-F2 using the 1.88 m telescope at OAO. The symbols are the same as those in figure 16.

parameter space. However, this analysis will be presented in a subsequent publication.

We also analyzed the line shape deformation by calculating BIS, BIS′, and the S index of Ca II lines, and their periodograms. As a result, no significant periodicity was found. As seen in figure 19, the BISs of different instruments are averagely on different levels (HIDES-S, $\overline{\mathrm{BIS}} = 193.48$ m s^{-1}; HIDES-F1, $\overline{\mathrm{BIS}} = 164.67$ m s^{-1}; HIDES-F2, $\overline{\mathrm{BIS}} = 120.84$ m s^{-1}), indicating that the observed line deformation was primarily driven by the IP rather than the star's intrinsic activity. The star's projected rotational velocity is $v \sin i = 1.75$ km s^{-1} (Takeda et al. 2008). Adopting a stellar radius of $R_\star = 13.76\ R_\odot$, we derived a maximum rotational period of $P_{\mathrm{rot}} = 397.9$ d, which is slightly shorter than the RV variation of 434 d.

More scenarios can be responsible for regular RV variation and mimic planetary signals. Long secondary periods (LSPs; Saio et al. 2015) in red giant stars, probably caused by an oscillatory convective mode, can be monitored through the RV method. They usually show photometric variations up to 1 mag and RV variations of a few m s^{-1} in luminous ($L > 300\ L_\odot$) giant stars (Saio et al. 2015). A new form of stellar variability, whose mechanism is not fully understood, was detected in the K giants γ Dra (K5 III, $B - V = 1.53$; Hatzes et al. 2018) and Aldebaran (K5 III, $B - V = 1.54$; Reichert et al. 2019). They have RV semiamplitudes over 100 m s^{-1}, and they are likely to produce stars with larger $B - V$ values. However, 11 Com has photometric stability down to $\sigma = 0.006$ mag and $B - V = 0.99$ (ESA 1997), which is distinct from the

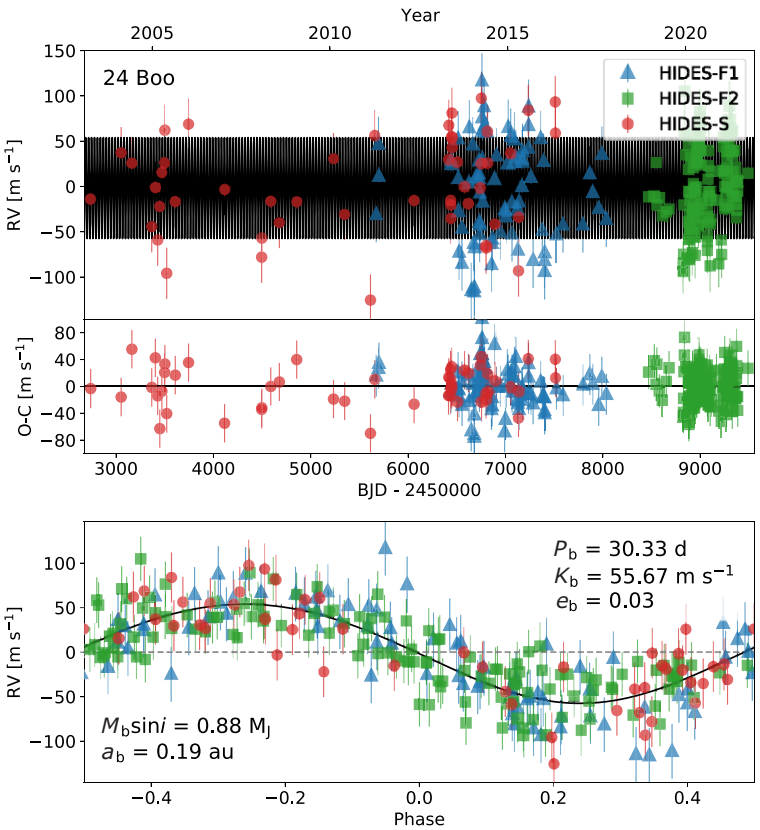


Fig. 20. Single Keplerian solution to 24 Boo. Top: Best-fit single Keplerian curve in the full observation span, including fitted RV offsets between instruments and jitters that are included in the error bars. Middle: Residuals of the RVs with respect to the best-fit model. Bottom: Phase-folded orbit of the planet. Data taken by HIDES-S, HIDES-F1, and HIDES-F2 using the 1.88 m telescope at OAO are shown with red circles, blue triangles, and green squares, respectively.

Downloaded from https://academic.oup.com/pasj/article/75/6/1030/7272944 by ANKARA user on 22 December 2023

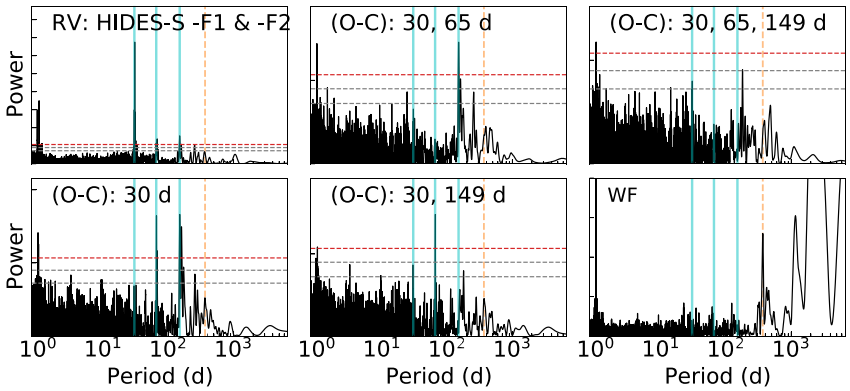


Fig. 21. GLS periodograms for 24 Boo. Top left: Observed RVs. Bottom left: RV residuals to the single Keplerian fitting of the known planet. Top middle: RV residuals with the removal of the known planet and regular 65-d variation. Bottom middle: RV residuals with the removal of the known planet and regular 149-d variation. Top right: RV residuals to the 3-Keplerian fitting to the known planet, and 65- and 149-d variations. Bottom right: window function of the observed RVs. The horizontal lines represent 10%, 1%, and 0.1% FAP levels from bottom to top. The vertical cyan solid lines indicate the focused periodic signals, including a planetary signal at 30 d and two significant signals in the residuals at 65 and 149 d, and the vertical orange dashed line indicates 1 yr.

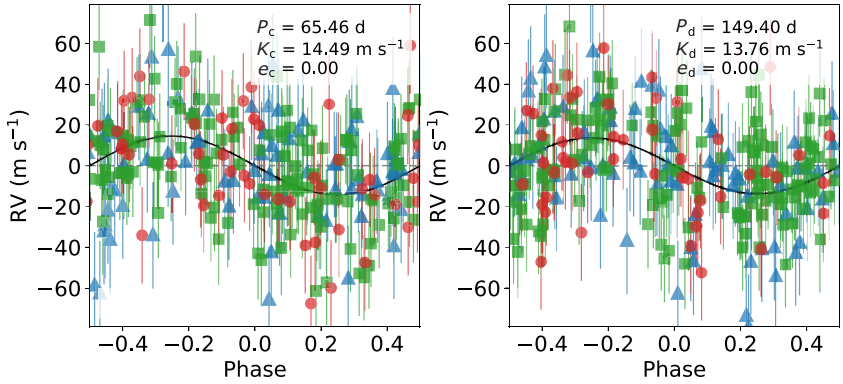


Fig. 22. Phase-folded curves of the regular 65- (left) and 149-d (right) variations in 24 Boo RVs. The symbols are the same as those in figure 21.

observed properties of LSPs. Heeren et al. (2021) released the RV variations of ϵ Cyg A, which pretended to be a planetary signal but is likely an extreme example of a heartbeat binary system. The system has a close star separation of 15 au. Although 11 Com A has a stellar companion, the heartbeat can be neglected due to the large separation of 999.0 au (Roell et al. 2012).

An asteroseismology analysis was provided by Ando et al. (2010). From intensive RV monitoring, we estimated an RV amplitude of ~ 10 m s^{-1} caused by solar-like p-mode oscillation. Using the scaling relation in Kjeldsen and Bedding (1995), we estimated a p-mode oscillation jitter amplitude of about 10.7 m s^{-1}, which is in good agreement with the observation. Although the oscillation should be responsible for the large RV scatter of the residuals, it is not the cause of long-period (i.e., a few hundred days) variations since the oscillation time scale is only a few hours.

Therefore, the complicated RV variations in the RV time series remain mysterious, and so far, we cannot conclude a self-consistent explanation for them. Follow-up work to appear in a forthcoming paper may lift the veil of truth.

5.3 24 Boo: two planet candidates

24 Boo is a G3 IV star and reported to harbor a close-in giant planet in Takarada et al. (2018). We started observation of 24 Boo at OAO in 2003 April. After a 13-yr monitoring period with HIDES-S and HIDES-F1, we confirmed and released the planet in 2018. Since a 150-d variation remained in the residual of the single Keplerian model, we continued intensive observation of this star with HIDES-F1 and HIDES-F2. By 2021 June, we had in total obtained 282 spectra with RVs. A single Keplerian model fitting yielded $P = 30.33^{+0.00}_{-0.01}$ d, $K = 55.67^{+2.31}_{-2.66}$ m s^{-1}, and $e = 0.032^{+0.039}_{-0.023}$ (figure 20). Adopting a stellar mass of $M_\star = 1.05\ M_\odot$, we can derive the companion mass of $M_\mathrm{p} \sin i = 0.883^{+0.036}_{-0.043}\ M_\mathrm{J}$

Downloaded from https://academic.oup.com/pasj/article/75/6/1030/7272944 by ANKARA user on 22 December 2023

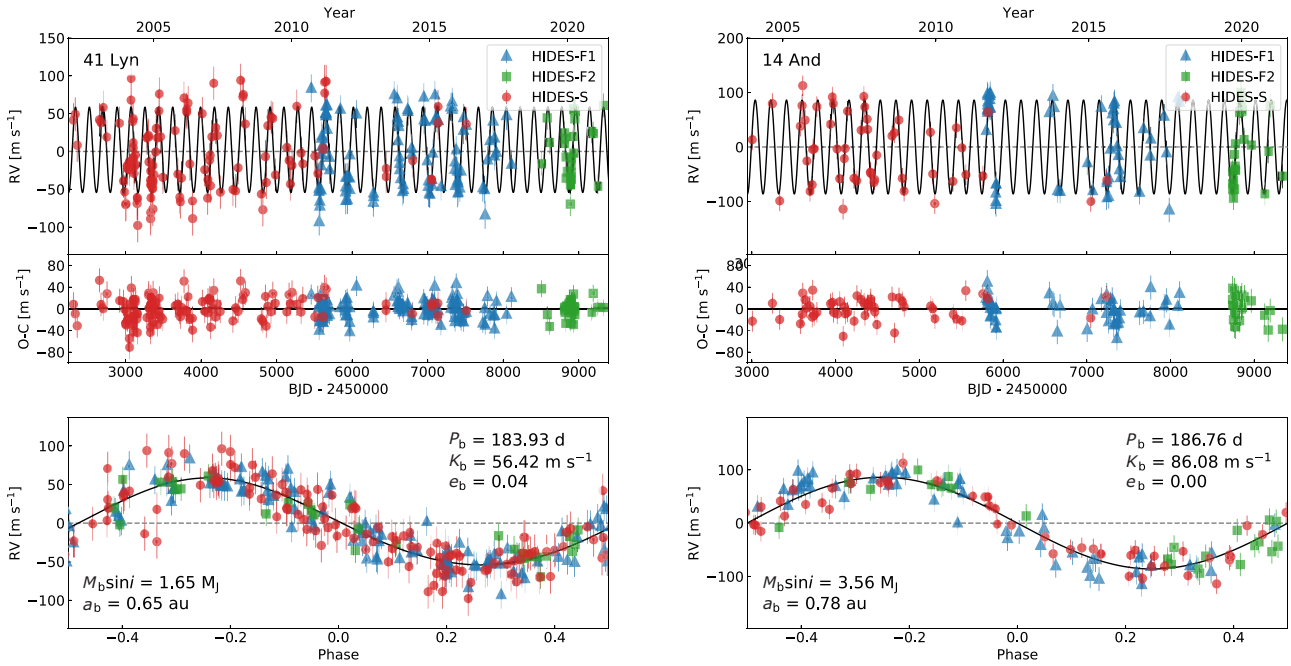


Fig. 23. Single Keplerian solution to 41 Lyn (left) and 14 And (right). Top: Best-fit 1-Keplerian curve in the full observation span, including fitted RV offsets between instruments and jitters that are included in the error bars. Middle: Residuals of the RVs with respect to the best-fit model. Bottom: Phase-folded orbit of the planet. Data taken by HIDES-S, HIDES-F1, and HIDES-F2 using the 1.88 m telescope at OAO are shown with red circles, blue triangles, and green squares, respectively.

and a semimajor axis of $a = 0.194$ au. The rms scatter of the single Keplerian fit was 27.81 m s^{-1}.

As seen in figure 21, the RV residuals to the single Keplerian fitting exhibit regular variations at 65 and 149 d. Considering large rms scatter in residuals, these variations also suggested a possible outer companion(s). We then separately subtracted 65- and 149-d signals by sinusoidal curve fitting, and the periodogram of the residuals showed the other signal. We thus performed a triple Keplerian fitting with the known planet fixed and the eccentricities of prospective planets fixed to 0. Consequently, the rms scatter was suppressed to 23.59 m s^{-1} (decreased by 4.22 m s^{-1}), and we obtained $P_c = 65.46$ d, $K_c = 14.49$ m s^{-1}, and $P_d = 149.40$ d, $K_c = 13.76$ m s^{-1}. The semiamplitudes of these variations are lower than the rms scatter. If these variations are truly introduced by planets then we could have one planet with $M_p \sin i = 0.30\ M_J$ and $a = 0.32$ au, and another planet with $M_p \sin i = 0.37\ M_J$ and $a = 0.56$ au (figure 22).

We also calculated the line profiles and the Ca II index, yet we did not find any periodicity related to 30, 65, and 149 d. As the star is slowly rotating with $v \sin i \lesssim 3.36$ km s^{-1}, we derived its maximum rotational period to be about 184 d, which is longer than either 65 or 149 d. In addition, since these two signals are weak compared to the large jitter and scatter, we cannot validate the existence of the second and third planets at this stage.

Furthermore, we note that the 24 Boo system is almost a twin of the HD 167768 system (Teng et al. 2023) in a few aspects. The central stars are both metal-poor (Fe/H $\lesssim -0.7$) and deeply evolved red-giant branch stars ($\log g < 2.5$ cgs) in the galactic thick disk (Takeda et al. 2008), and they both harbor a close-in giant planet with two possible planet candidates at wider orbits.

5.4 41 Lyn and 14 And: synchronous BIS variations

41 Lyn (HD 81688, HR 2743, HIP 46471) is classified as a K0 III-IV star and reported to have a planet in Sato et al. (2008a). The first spectrum was collected in 2003 March with HIDES-S, and we continued monitoring the star with HIDES-S, HIDES-F1, and HIDES-F2 after the announcement of the planet until 2021 April. The best-fit Keplerian model yields a near circular orbit with $P = 183.93^{+0.09}_{-0.09}$ d, $K = 56.42^{+1.87}_{-1.88}$ m s^{-1}, and $e = 0.040^{+0.022}_{-0.031}$. The rms scatter of RV residuals was 20.17 m s^{-1}. Adopting a stellar mass of $M_\star = 1.07\ M_\odot$, we obtained the companion mass of $M_p \sin i = 1.654\ M_J$ and a semimajor axis of $a = 0.648$ au.

14 And (HD 221345, HR 8930, HIP 116076) is classified as a K0 III star and reported to host a planet in Sato et al. (2008b). The first spectrum was collected in

Downloaded from https://academic.oup.com/pasj/article/75/6/1030/7272944 by ANKARA user on 22 December 2023

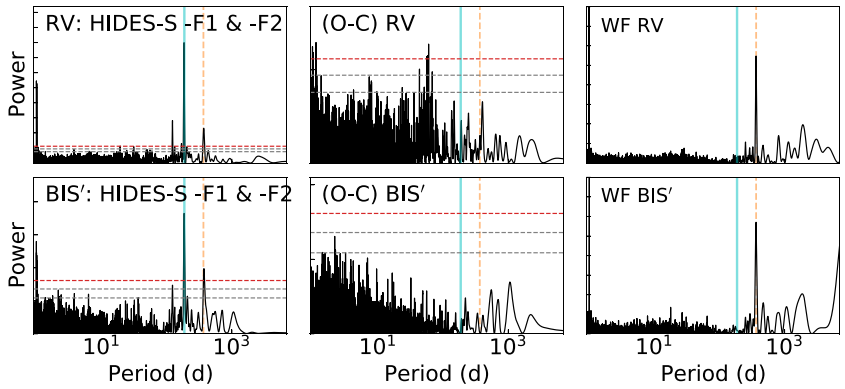


Fig. 24. GLS periodograms for 41 Lyn. Top left: observed RVs. Bottom left: BIS′. Top middle: RV residuals to the 1-Keplerian fitting of the known planet. Bottom middle: BIS′ residuals with removal of regular variation. Top right: Window function of the observed RVs. Bottom right: Window function of BIS′. The horizontal lines represent 10%, 1%, and 0.1% FAP levels from bottom to top. The vertical cyan solid lines indicate planetary signals, and the vertical orange dashed line indicates 1 yr.

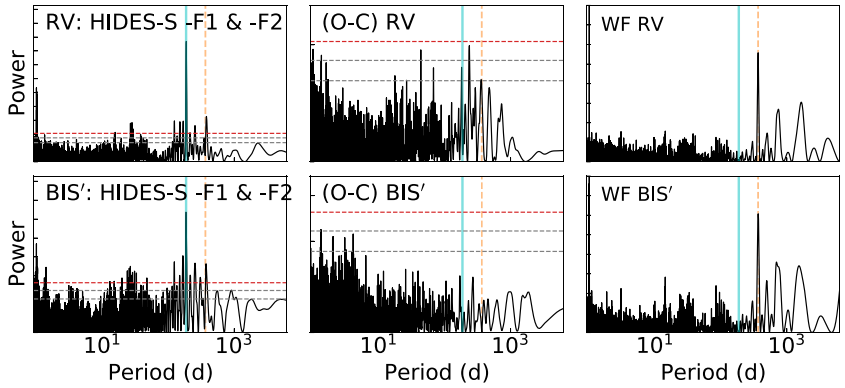


Fig. 25. GLS periodograms for 14 And. Top left: observed RVs. Bottom left: BIS′. Top middle: RV residuals to the 1-Keplerian fitting of the known planet. Bottom middle: BIS′ residuals with removal of regular variation. Top right: Window function of the observed RVs. Bottom right: Window function of BIS′. The horizontal lines represent 10%, 1%, and 0.1% FAP levels from bottom to top. The vertical cyan solid lines indicate planetary signals, and the vertical orange dashed line indicates 1 yr.

2004 January with HIDES-S, and we continued monitoring the star with HIDES-S, HIDES-F1, and HIDES-F2 after the announcement of the planet until 2021 May. The RV variation can be well fitted by a circular orbital with $P = 186.76^{+0.11}_{-0.12}$ d and $K = 86.08^{+2.76}_{-2.95}$ m s^{-1}. The rms scatter of RV residuals was 21.28 m s^{-1}. Adopting a stellar mass of $M_\star = 1.78\ M_\odot$, we obtained the companion mass of $M_{\rm p}\sin i = 3.559\ M_{\rm J}$ and a semimajor axis of $a = 0.775$ au.

The latest RV Keplerian fitting results (figure 23) of 41 Lyn and 14 And accord with previous reports (Sato et al. 2008a, 2008b). However, with long-baseline monitoring, we note that the line profiles of both stars regularly vary in time over periods of their fitted orbital periods.

Here, BIS′ is applied to quantify the line profile variation, and it is defined as the mean removed BIS (Teng et al. 2022a). As illustrated in figures 24 and 25, GLS periodograms showed that the RV data and BIS′ data share almost the same periodicity for 41 Lyn and 14 And, respectively. We then performed a sinusoidal curve fitting to BIS′ for both stars. Similar to the circular orbital fitting to RVs (e.g., the aforementioned fitting of 14 And), the BIS′ fitting included free parameters of semiamplitude, period, phase of the curve, and offset to the BIS′ zero point of each instrument. The determination of best-fit parameters followed the same way as Keplerian fitting in this study (section 3).

For 41 Lyn, we obtained $P_{\rm BIS'} = 184.70$ d, which is almost equal to the best-fit orbital period of $P_{\rm orb} = 183.93$ d. Once again, for 14 And, it is $P_{\rm BIS'} = 185.60$ d to $P_{\rm orb} = 186.76$ d. Moreover, BIS variations of both stars seemed synchronous to their RV variations, as the BIS phases coincided well with the RV phases. As shown in figure 26, we scale the amplitude of the BIS′ curve and find that it almost overlaps with the RV curve for both stars. We further calculated the correlation coefficient with Pearson's

Downloaded from https://academic.oup.com/pasj/article/75/6/1030/7272944 by ANKARA user on 22 December 2023

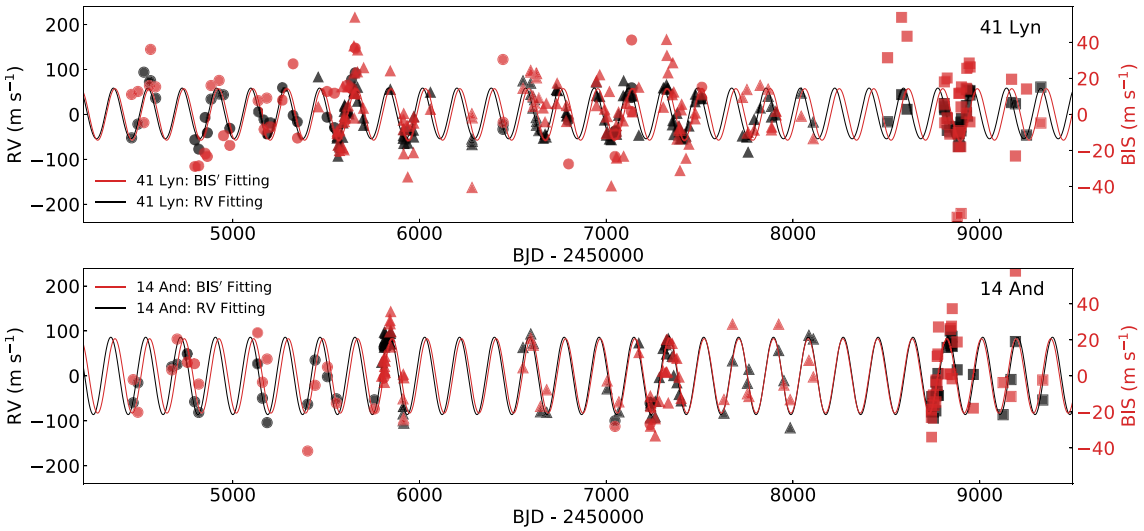


Fig. 26. Comparison between RVs and the BIS of 41 Lyn (upper) and 14 And (lower). The RVs with offset removed and the BIS with offset removed are shown in black and red markers, respectively. The markers with different shapes indicate the different instruments used: circle, triangle, and square represent HIDES-S, HIDES-F1, and HIDES-F2, respectively. The best-fit 1-Keplerian orbit and BIS variation are shown with black and red curves, respectively.

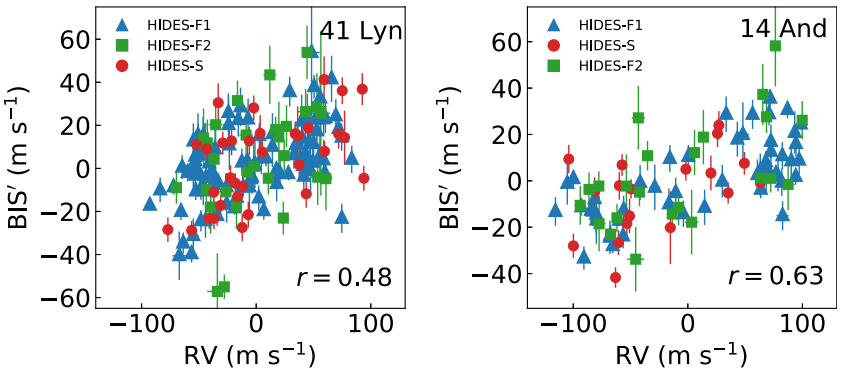


Fig. 27. BIS′ (mean removed BIS) against RVs of 41 Lyn (left) and 14 And (right). The data are taken by HIDES-S, HIDES-F1, and HIDES-F2 using the 1.88 m telescope at OAO. The symbols are the same as those in figure 23.

r between BIS′ and RVs with the removal of their instrumental offsets. Consequently, we obtained $r = 0.48$ for 41 Lyn and $r = 0.63$ for 14 And, which both indicate relatively strong correlation (figure 27).

The maximum rotational period can be estimated by projected rotational velocity $v \sin i$ and stellar radius $R_\star$. Adopting $v \sin i = 1.2$ km s^{-1} (Takeda et al. 2008) and $R_\star = 11.13\ R_\odot$ for 41 Lyn, and $v \sin i = 2.6$ km s^{-1} (Takeda et al. 2008) and $R_\star = 11.55\ R_\odot$ for 14 And, we obtain the maximum rotational periods of 487 and 225 d for 41 Lyn and 14 And, respectively. Combined with the fact that line profile correlates with RV, it could be inferred that 41 Lyn b (HD 81688 b) and 14 And b are questionable, and they are probably mimicked by line shape deformation due to the rotational modulation of stars.

Nonetheless, we are not yet able to confirm the rotational periods of 41 Lyn and 14 And. These two stars are considered to be chromospherically inactive stars for the inexistence of emission in the core of Ca II H lines (Sato et al. 2008a, 2008b). Hipparcos photometry revealed photometric stability of $\sigma = 0.006$ mag for both 41 Lyn and 14 And. We also analyzed the periodicity of the Ca II H index $S_{\rm H}$ and Hipparcos photometry. However, no significant periodic signal was indicated by the GLS periodogram.

In addition, we noted another ∼58-d signal with FAP lower than 0.1% in the periodogram of RV residuals of 41 Lyn. This RV variation could be interpreted by a sinusoidal curve with a period of 57.4 d and a semiamplitude of 5.9 m s^{-1}. At the current stage, we could not deduce the source of this RV variation with current data sets.

Downloaded from https://academic.oup.com/pasj/article/75/6/1030/7272944 by ANKARA user on 22 December 2023

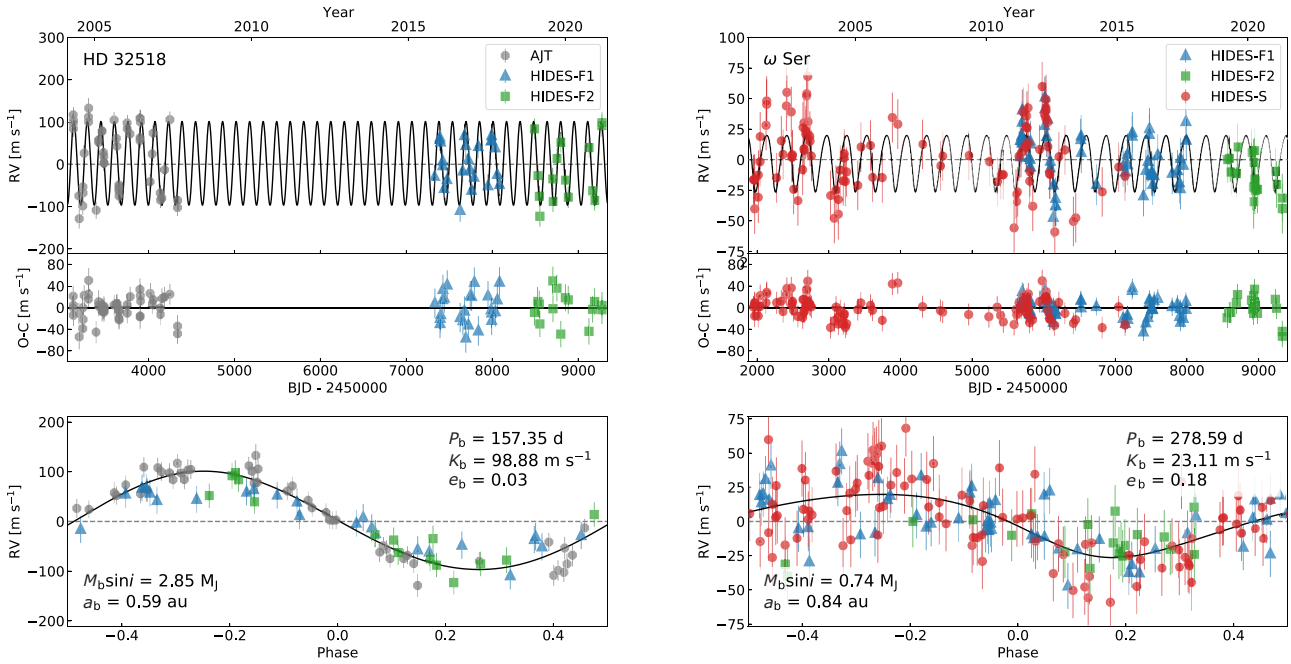


Fig. 28. Single Keplerian solutions to HD 32518 (left) and ω Ser (right). Top: Best-fit single Keplerian curve in the full observation span, including fitted RV offsets between instruments and jitters that are included in the error bars. Middle: Residuals of the RVs with respect to the best-fit model. Bottom: Phase-folded orbit of the planet. Data taken by the CES on the 2 m AJT at Thuringia State Observatory are shown with gray octagons. Data taken by HIDES-S, HIDES-F1, and HIDES-F2 using the 1.88 m telescope at OAO are shown with red circles, blue triangles, and green squares, respectively.

5.5 HD 32518 and ω Ser: unstable RV amplitudes from different observations

HD 32518 (HR 1636, HIP 24003) is a K1 III star (Döllinger et al. 2009) with one previously known planet. Döllinger et al. (2009) observed the star by using the CES of the 2 m Alfred Jensch telescope of the Thüringer Landessternwarte and obtained 58 spectra. We observed this star with HIDES-F1 and HIDES-F2 and obtained 24 and 15 spectra, respectively, and our first HIDES observation was 8 yr after the end of the observation of Döllinger et al. (2009). The best-fit Keplerian model with all data yielded the orbital parameters for the companion of $P = 157.35^{+0.10}_{-0.08}$ d, $K = 98.88^{+5.60}_{-5.88}$ m s^{-1}, and $e = 0.028^{+0.034}_{-0.019}$ (figure 28). Adopting its stellar mass of $M_\star = 1.13\ M_\odot$, we obtained the companion mass of $M_\mathrm{p}\sin i = 2.849\ M_\mathrm{J}$ and a semimajor axis of $a = 0.594$ au.

ω Ser (HD 141680, HR 5888, HIP 77578) is a G8 III star, which was first reported to have RV variation in Sato et al. (2005). The planet was announced in Sato et al. (2013b) with data collected from HIDES-S and HIDES-F1 since 2001 February. We continued to observe the star using HIDES-F1 and HIDES-F2 after Sato et al. (2013b) and collected 179 RVs until April 2021. The best-fit Keplerian model with all RVs yielded the orbital parameters for the companion of $P = 278.59^{+0.80}_{-0.61}$ d, $K = 23.11^{+1.94}_{-3.38}$ m s^{-1}, and $e = 0.180^{+0.066}_{-0.127}$ (figure 28). The rms was 19.42 m s^{-1}. Adopting its stellar mass of $M_\star = 1.01\ M_\odot$, we obtained the companion mass of $M_\mathrm{p}\sin i = 0.736\ M_\mathrm{J}$ and a semimajor axis of $a = 0.838$ au.

According to our latest Keplerian fits, we noted that the semiamplitudes do not conform well with previous results. For HD 32518, Döllinger et al. (2009) obtained $K = 115.83 \pm 4.67$ m s^{-1}, which apparently differs by $K = 98.88^{+5.60}_{-5.88}$ m s^{-1} by this work, and for ω Ser, Sato et al. (2013b) obtained $K = 31.8^{+2.3}_{-2.3}$ m s^{-1}, which differs by $K = 23.11^{+1.94}_{-3.38}$ m s^{-1} by this work.

Meanwhile, we also noted that there were strong signals that remained at the value of orbital periods in the GLS periodogram of the residuals for both stars (figures 29 and 30). This suggested that the RV variations were not fully subtracted from the time series. The previous results were fully (HD 32518) or dominantly (ω Ser) constrained by data from one instrument. We therefore performed Keplerian orbital fits separately by data sets from different instruments. Here, we still considered HIDES-F1 and HIDES-F2 as two independent instruments, but we did not separate them into different fittings. As shown in figure 31, the fittings depending on different instruments were distinctive from each other.

For HD 32518, the semiamplitude from the HIDES data, $K = 73.85^{+3.84}_{-6.56}$ m s^{-1}, was apparently lower than that from the AJT data, $K = 113.48^{+4.66}_{-4.17}$ m s^{-1} over an

Downloaded from https://academic.oup.com/pasj/article/75/6/1030/7272944 by ANKARA user on 22 December 2023

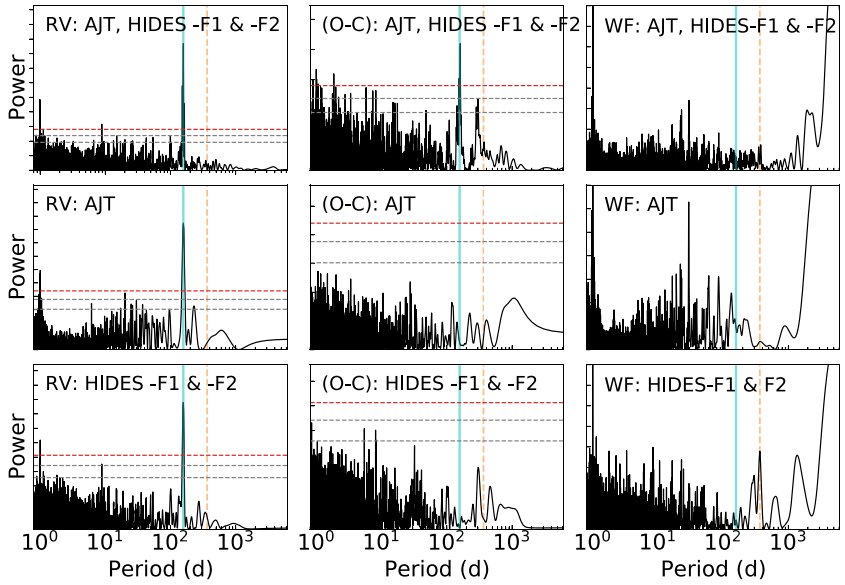


Fig. 29. GLS periodograms for HD 32518. From left to right column: Observed RVs, RV residuals to the single Keplerian fitting of the known planet, and the window function of the observed RVs. From top to bottom row: All observed data, data taken by the CES on the 2 m AJT at Thuringia State Observatory, and data taken by HIDES-F1 and HIDES-F2 on the 1.88 m telescope at OAO. The horizontal lines represent 10%, 1%, and 0.1% FAP levels from bottom to top. The vertical cyan solid line indicates the planetary signal, and the vertical orange dashed line indicates 1 yr.

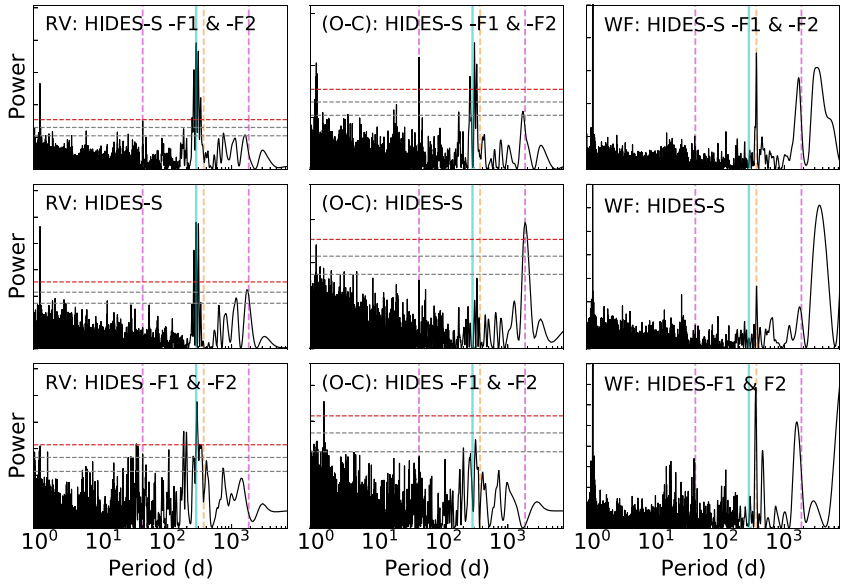


Fig. 30. GLS periodograms for ω Ser. From left to right column: Observed RVs, RV residuals to the single Keplerian fitting of the known planet, and the window function of the observed RVs. From top to bottom row: All data taken by HIDES on the 1.88 m telescope at OAO, data taken by HIDES-S, and data taken by HIDES-F1 and HIDES-F2. The horizontal lines represent 10%, 1%, and 0.1% FAP levels from bottom to top. The vertical cyan solid line indicates the planetary signal, the vertical magenta dashed lines indicate extra periodic signals appearing in the residuals, and the vertical orange dashed line indicates 1 yr.

8-σ level. As shown in the GLS periodogram of residuals (figure 29), the RV variation was fully subtracted in each separate data set. Furthermore, we confirmed that the BISs of both HIDES-F1 and HIDES-F2 did not correlate with the RV by Pearson's correlation with their r values equal to 0.03 and 0.21, respectively, and they did not show strong periodicity around 157 d. The long time lag of HIDES after the AJT observation made it impracticable to determine if the RV amplitude varied with time. The rms scatter obtained from the AJT data and HIDES data

Downloaded from https://academic.oup.com/pasj/article/75/6/1030/7272944 by ANKARA user on 22 December 2023

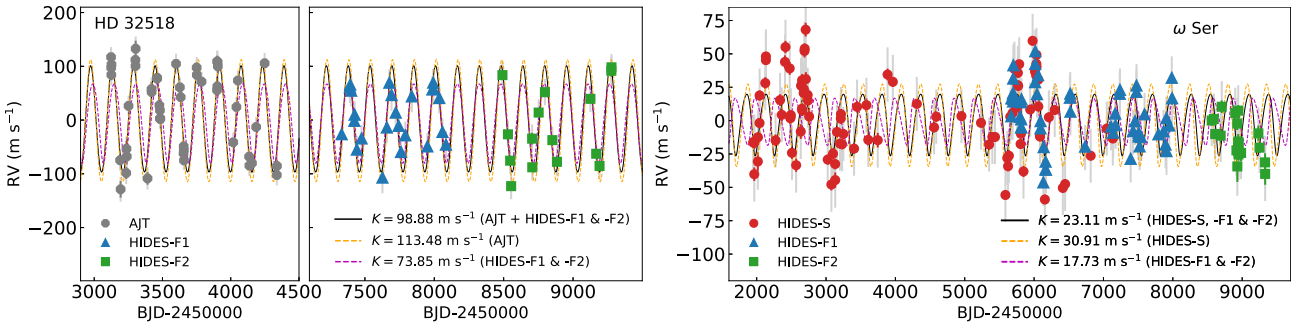


Fig. 31. Comparison between different single Keplerian fitting results for HD 32518 (left) and ω Ser (right) from different data sets. Black solid curve shows best fits using all observed data. Yellow dashed curve shows best fits using only data taken by the CES on the 2 m AJT at Thuringia State Observatory for HD 32518, and data taken by HIDES-S for ω Ser. Magenta dashed curve shows best fits using data taken by HIDES-F1 and HIDES-F2 on the 1.88 m telescope at OAO. RV markers are the same as those in figure 28.

were both about 18 m s^{-1}. Hence we cannot confirm the true reason for the large difference in RV semiamplitudes at this stage.

For ω Ser, the semiamplitude from the HIDES-F1 and F2 data, $K = 17.73^{+4.24}_{-3.74}$ m s^{-1}, was apparently lower than that from the HIDES-S data, $K = 30.91^{+2.49}_{-4.21}$ m s^{-1} over a 3-σ level. As seen in the GLS periodogram of residuals (middle column in figure 30), the 278-d RV variation was clearly subtracted in separate data sets, while it was not fully subtracted in the full data. Moreover, full data residuals exhibited an additional periodicity of 40.54 d, and HIDES-S residuals exhibited another additional periodicity of 1852 d.

Assuming a planetary situation, the 40.54-d signal in the full data set could be subtracted by a Keplerian orbit of $P = 40.54$ d, $K = 12.7$ m s^{-1}, $e = 0.28$, and with a planetary mass of $M_{\rm p}\sin i = 0.2$ $M_{\rm J}$, and the rms scatter suppressed to ~ 17.75 m s^{-1} (decreased by ~ 1.67 m s^{-1}). The 1852-d signal in the HIDES-S data set could be interpreted by another Keplerian orbit of $P = 1840$ d, $K = 14.5$ s^{-1}, $e = 0.02$, and with a planetary mass of $M_{\rm p}\sin i = 0.82$ $M_{\rm J}$, and the rms scatter suppressed to $\sim$16.69 m s^{-1} (decreased by $\sim$2.73 m s^{-1}).

However, we could hardly treat them as planet candidates. According to the window function to ω Ser observations (right column in figure 30), peaks appeared close to 1852 d for all three sets, and another peak emerged at 40 d for HIDES-F1 and HIDES-F2. These strongly suggested that the periodicity might be caused by an observational window, although they could be well fitted by Keplerian orbits. In addition, the number of HIDES-F2 observations (21) is less than the numbers of HIDES-S (99) and HIDES-F1 (59) observations. Since the RVs from HIDES-F1 around BJD 2456000 by eye conformed well with RVs from HIDES-S, more observations from HIDES-F2 are necessary to determine a convincing RV semiamplitude, as well as long-term periodicity.

6 Joint fits with astrometry

Among the revisited stars in this study, four stars, HD 5608, HD 14067, HD 120084, and HD 175679, showed significant astrometric acceleration from HGCA of $\chi^2 > 14$ (Brandt 2018, 2021), which allows us to introduce astrometric data and perform joint constraints on the orbital parameters for the four systems.

As introduced in section 4, we refined the orbital parameters of the four systems by RV-only analyses (figure 32 and table 3). However, we did not directly adopt RVs in those analyses to the joint constraint; instead, we re-extracted the RVs from HIDES-S, HIDES-F1, and HIDES-F2 by using the same reference spectra. This was mainly to

(1) better express the RV long-term trend in the decades-long baseline;
(2) avoid fake RV long-term trends or fake RV offsets introduced by over-fitting;

however, this could include acceptable RV offsets between different observation modes (appendix 1) and lose some precision for HIDES-F1 and HIDES-F2. We then performed Keplerian orbital fits in the same way as described in section 3 and obtained new orbital parameters, the RV long-term trend, RV offsets, and extra jitters. Specifically for HD 5608, the significant astrometric acceleration is triggered by the outer stellar companion and manifests as RV long-term acceleration; we thus subtracted the orbital motion due to the inner planetary companion with its best-fit model. This completes the preparation of the RV data.

The stars' absolute astrometry data were directly obtained from the HGCA EDR3 version. In addition, HD 5068 has relative astrometry for its distant companion from direct imaging (Ryu et al. 2016).

We performed joint constraints by using `orvara` software (Brandt et al. 2021), which adopts astrometric and RV measurements and generates MCMC simulations to

Downloaded from https://academic.oup.com/pasj/article/75/6/1030/7272944 by ANKARA user on 22 December 2023

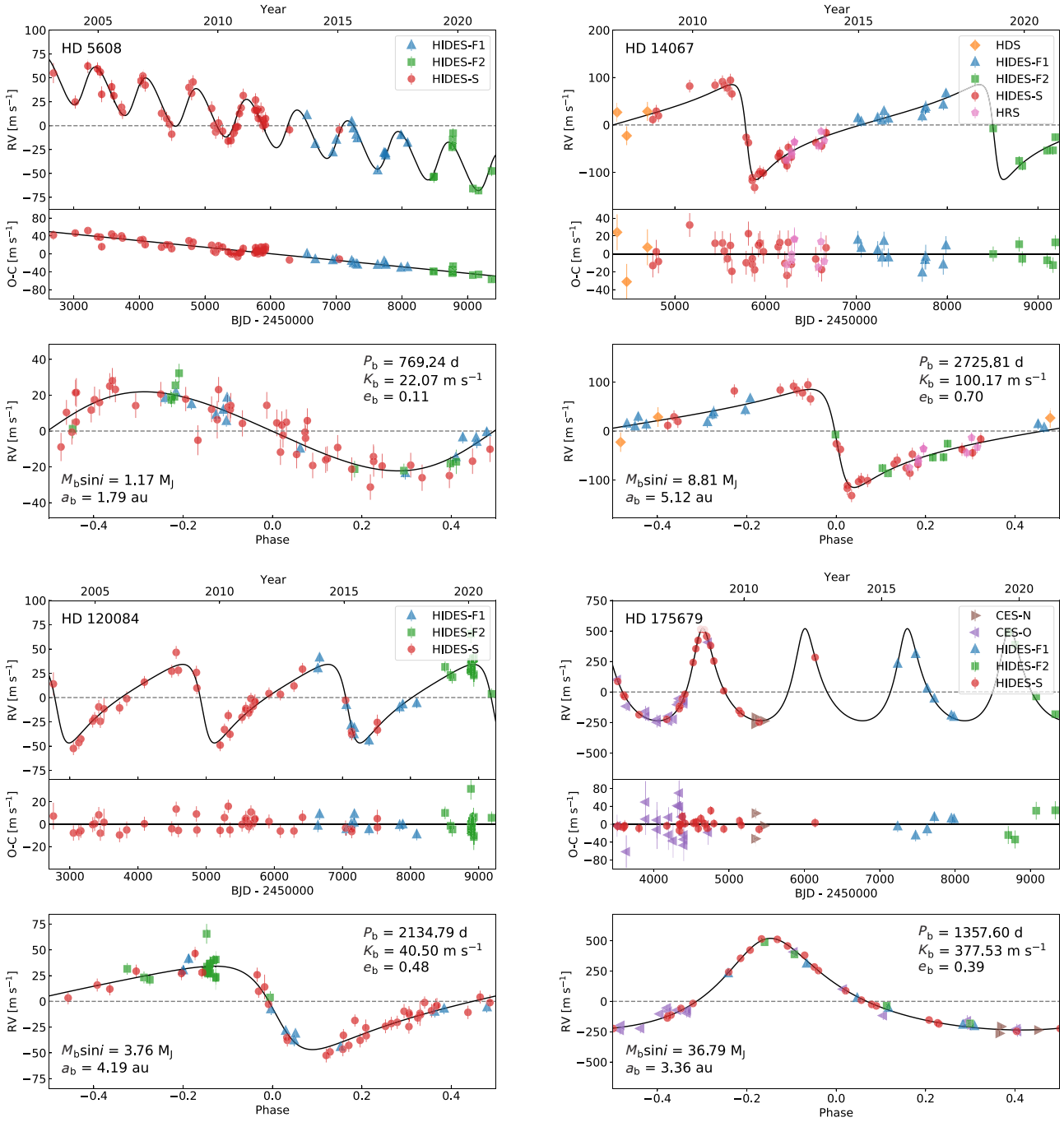


Fig. 32. Single Keplerian solutions to HD 5608, HD 14067, HD 120084, and HD175679. For each panel, the top subplot displays the best-fit single Keplerian curve in the full observation span, including fitted RV offsets between instruments and jitters that are included in the error bars; the middle subplot displays residuals of the RVs with respect to the best-fit model; and the bottom subplot displays the phase-folded orbit of the planet. Data taken by HIDES-S, HIDES-F1, and HIDES-F2 using the 1.88 m telescope at OAO are shown with red circles, blue triangles, and green squares, respectively. Data taken by the HDS on the Subaru telescope at Maunakea are shown with orange spades. Data taken by CES-O, CES-N, and HRS on the 2.16 m telescope at Xinglong Observatory are shown with purple triangles, brown triangles, and pink pentagons, respectively.

further estimate the orbital parameters. In the joint constraints, we applied the default orbital parameters provided by `orvara`. We set all parameters free with moderate priors. We adopted Gaussian priors on stellar mass according to the values derived in section 2, with the log-uniform prior on the extra RV jitter between 1 m s^{-1} and 5 σ of fitted extra jitters from `RadVel`, and default priors provided by `orvara` on other parameters.

We generated MCMC simulations with `ptemcee` (Foreman-Mackey et al. 2013; Vousden et al. 2016) to

Downloaded from https://academic.oup.com/pasj/article/75/6/1030/7272944 by ANKARA user on 22 December 2023

Table 4. Joint fitting results of HD 5608, HD 14067, HD 120084, and HD 175679.

Object	HD 5608 B	HD 14067 b	HD 120084 b	HD 175679 b
Primary mass $M_{\rm pri}$ ($M_\odot$)	$1.28^{+0.23}_{-0.23}$	$2.40^{+0.20}_{-0.20}$	$2.16^{+0.28}_{-0.27}$	$2.70^{+0.30}_{-0.30}$
Secondary mass $M_{\rm sec}$ ($M_{\rm J}$)	$121.2^{+8.3}_{-7.0}$	$15.3^{+6.2}_{-4.5}$	$6.4^{+2.9}_{-1.9}$	$61.8^{+15}_{-9.4}$
Semimajor axis a (au)	$30.7^{+8.8}_{-4.9}$	$5.15^{+0.14}_{-0.15}$	$4.21^{+0.17}_{-0.19}$	$3.36^{+0.12}_{-0.13}$
$\sqrt{e}\sin\omega$	$-0.63^{+0.29}_{-0.16}$	$0.773^{+0.022}_{-0.022}$	$0.673^{+0.026}_{-0.028}$	$-0.122^{+0.014}_{-0.013}$
$\sqrt{e}\cos\omega$	$-0.13^{+0.36}_{-0.33}$	$-0.220^{+0.052}_{-0.051}$	$-0.167^{+0.061}_{-0.058}$	$0.5969^{+0.0072}_{-0.0073}$
Inclination i (°)	$147.5^{+6.6}_{-13}$	118^{+31}_{-84}	49^{+87}_{-21}	$41.3^{+109}_{-6.4}$
Inclination i ($i < 90°$) (°)*	—	39^{+28}_{-13}	38^{+22}_{-12}	$39.2^{+6.2}_{-5.1}$
Inclination i ($i > 90°$) (°)*	$147.5^{+6.6}_{-13}$	141^{+12}_{-23}	139^{+15}_{-29}	$152.4^{+3.3}_{-4.4}$
Ascending node Ω (°)	141^{+56}_{-48}	165^{+37}_{-49}	156^{+129}_{-37}	228^{+17}_{-150}
Mean longitude at $\lambda_{\rm ref}$ (°)	112^{+84}_{-76}	$27.3^{+3.0}_{-3.0}$	$146.9^{+2.7}_{-2.8}$	$137.93^{+0.51}_{-0.50}$
Period (yr)	146^{+74}_{-37}	$7.513^{+0.044}_{-0.038}$	$5.864^{+0.024}_{-0.026}$	$3.7109^{+0.0035}_{-0.0036}$
Argument of periastron ω (°)	257^{+32}_{-35}	$105.9^{+3.8}_{-3.8}$	$103.9^{+5.1}_{-5.2}$	$348.4^{+1.3}_{-1.3}$
Eccentricity e	$0.53^{+0.18}_{-0.26}$	$0.650^{+0.027}_{-0.028}$	$0.483^{+0.027}_{-0.029}$	$0.3714^{+0.0080}_{-0.0079}$
Semimajor axis a (mas)	524^{+151}_{-84}	$36.6^{+1.0}_{-1.0}$	$40.5^{+1.7}_{-1.8}$	$19.99^{+0.71}_{-0.76}$
Periastron $T_{\rm p}$ (JD–2450000)	22895^{+17464}_{-5098}	5797^{+11}_{-12}	7083^{+17}_{-17}	$5990.1^{+3.7}_{-3.8}$
Mass ratio	$0.091^{+0.021}_{-0.015}$	$0.0061^{+0.0024}_{-0.0018}$	$0.00287^{+0.0013}_{-0.00084}$	$0.0219^{+0.0053}_{-0.0030}$

*The inclination distributions are bimodal for companions without direct imaging measurements, so we separately report the values for prograde and retrograde orbits.

explore the parameter space. For each star, we generated 15 temperatures and 100 walkers with at least 4×10^5 steps per walk. Here we briefly address the definition of "temperature" from Vousden, Farr, and Mandel (2016). At higher temperatures, the posterior distribution approaches the prior, facilitating an efficient exploration of the entire prior volume by the chain without becoming trapped in areas of parameter space with high probability density. Conversely, at lower temperatures, a chain can more effectively sample from high-probability regions. In each simulation, we recorded every 50 steps and set 20% of the chain as the burn-in length. The orbital parameters fitted and derived by joint constraints are given in table 4.

6.1 HD 5608 B

The significant acceleration in astrometry is triggered by its stellar companion that was first confirmed by direct imaging by Ryu et al. (2016). Here, we comprehensively adopted the latest RVs and absolute and relative astrometry and confirmed the stellar companion. HD 5608 B has a best-fit mass of $121.0^{+8.3}_{-7.0}$ $M_{\rm J}$ and it agrees with the mass estimation of 0.10 $M_\odot$ (105.8 $M_{\rm J}$) in Ryu et al. (2016) within 2σ. In addition, HD 5608 B has a large estimated eccentricity of 0.53, resulting in a periastron distance of $a(1-e) \sim 246$ au. The best-fit orbit with RV and astrometry measurements is shown in figure 33.

We note that the inner planetary companion has a slight eccentricity of about 0.1, and thus it is reasonable to consider the Kozai mechanism as a trigger to the eccentricity. The oscillation timescale of the Kozai mechanism can be estimated as (Holman et al. 1997)

$$P_{\rm Kozai} \sim \frac{M_{\rm A}}{M_{\rm B}} \frac{P_{\rm B}^2}{P_{\rm pl,0}} (1 - e_{\rm B}^2)^{3/2}, \tag{4}$$

where $M_{\rm A}$ is the mass of the primary star, $M_{\rm B}$ is the mass of the stellar companion, $P_{\rm B}$ is the period of the companion, $P_{\rm pl,\,0}$ is the initial orbital period of the planet, and $e_{\rm B}$ is the eccentricity of the stellar companion. Taking the best fit of HD 5608 B into the equation, we obtained the timescale $P_{\rm Kozai} \sim 68$ kyr, which is sufficiently shorter than the system's age (over Gyr).

We expect future observations, including continuous RV monitoring and direct imaging, to lead to tighter constraints on the orbital configuration of the HD 5608 system. We also hope to deeply investigate the stability and Kozai mechanism of this system with new observations so as to recover the evolutionary progress of the system.

6.2 HD 14067 b

From the latest RVs, we confirmed that the wide-orbit solution ($P \sim 2800$ d) of HD 14067 b given by Wang et al. (2014) should be the true scenario. By combining the RVs

Downloaded from https://academic.oup.com/pasj/article/75/6/1030/7272944 by ANKARA user on 22 December 2023

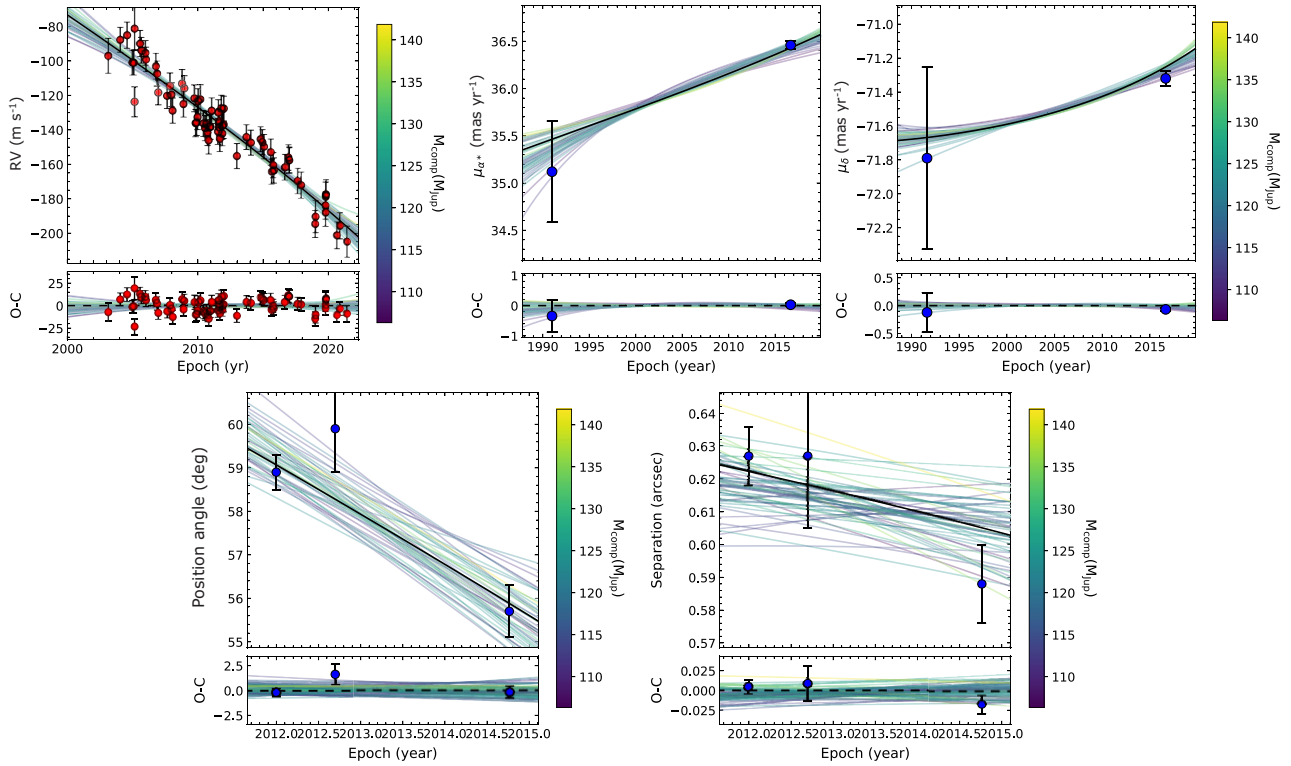


Fig. 33. Joint fit result of HD 5608 B using RV and astrometry with the removal of the known planet (HD 5608 b). The best-fit orbit is indicated with black solid curves, while the randomly selected 50 orbits are shown with colored lines, corresponding to the estimated masses of HD 5608 B. Upper left: RV curve with offset-removed RVs in red circles. Upper middle and upper right: proper motion variations of HD 5608 along RA and Dec. Bottom left and bottom right: position angles and the measured projected separations of HD 5608 B relative to HD 5608.

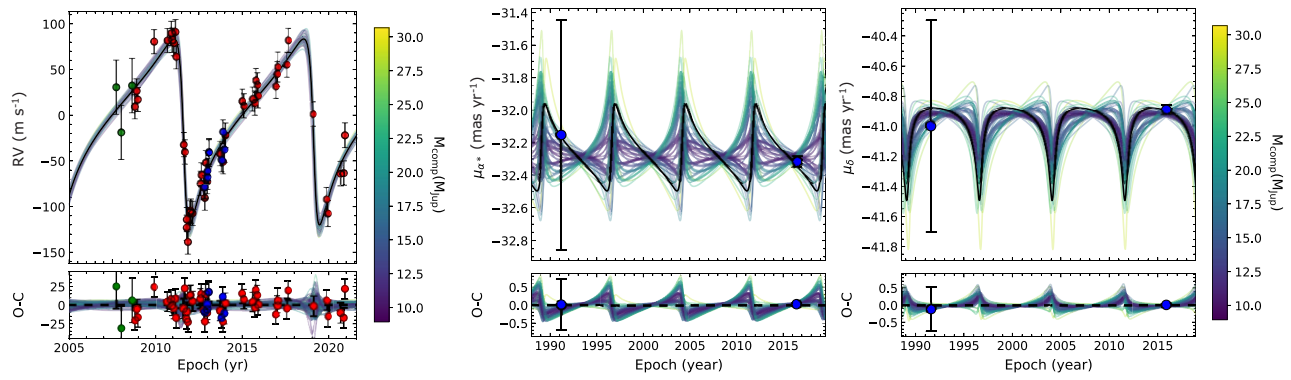


Fig. 34. Joint fit of HD 14067 b using RV and astrometry. Left: RV curve with RVs in red circles. Middle and right: Proper motion variations of HD 14067 along RA and Dec. The best-fit orbital solution is shown with a black solid line, and another 50 orbits randomly taken from MCMC chains are shown with colored lines, corresponding to the estimated masses of HD 14067 b.

with astrometry data, we estimated a best-fit semimajor axis (a) of $5.14^{+0.21}_{-0.22}$ au, a mass of $15.3^{+6.2}_{-4.5}$ M_J, and an inclination of $39^{+28}_{-13}{}^\circ$ or $147.5^{+6.6}_{-13}{}^\circ$. Furthermore, the joint constraint also supports the highly eccentric orbit with the best fit of $e = 0.650^{+0.027}_{-0.028}$. The best-fit orbit with RV and astrometry measurements is shown in figure 34.

6.3 HD 120084 b

HD 120084 b has a best-fit semimajor axis (a) of $4.21^{+0.17}_{-0.19}$ au, a mass of $6.4^{+2.9}_{-1.9}$ M_J, and an inclination of $38^{+22}_{-12}{}^\circ$ or $139^{+15}_{-29}{}^\circ$. The best-fit orbit with RV and astrometry measurements is shown in figure 35.

Downloaded from https://academic.oup.com/pasj/article/75/6/1030/7272944 by ANKARA user on 22 December 2023

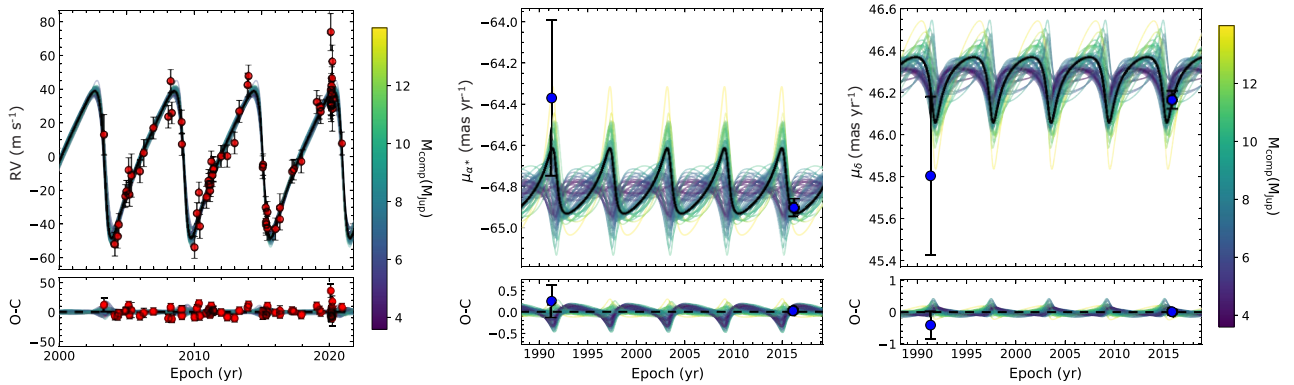


Fig. 35. Joint fit of HD 120084 b using RV and astrometry. Left: RV curve with RVs in red circles. Middle and right: Proper motion variations of HD 120084 along RA and Dec. The best-fit orbital solution is shown with a black solid line, and another 50 orbits randomly taken from MCMC chains are shown with colored lines, corresponding to the estimated masses of HD 120084 b.

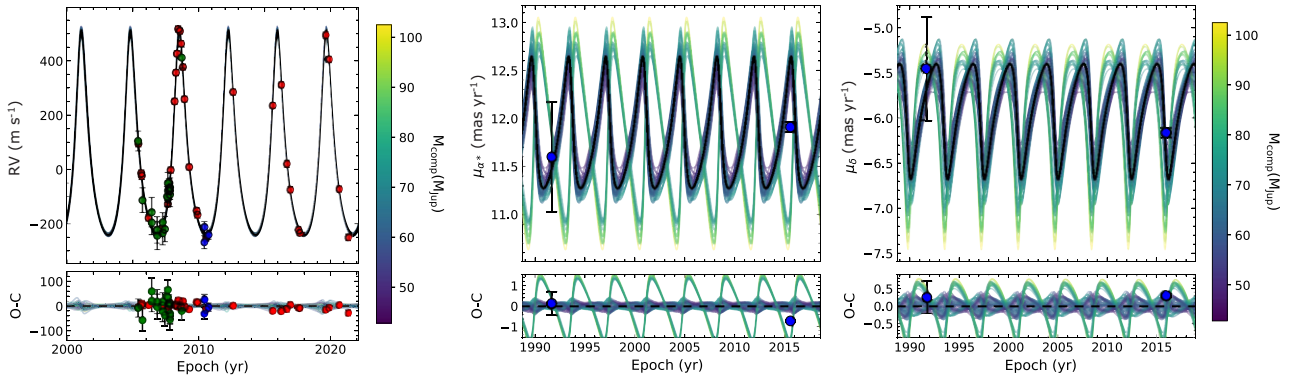


Fig. 36. Joint fit of HD 175679 b using RV and astrometry. Left: RV curve with RVs in red circles. Middle and right: Proper motion variations of HD 175679 along RA and Dec. The best-fit orbital solution is shown with a black solid line, and another 50 orbits randomly taken from MCMC chains are shown with colored lines, corresponding to the estimated masses of HD 175679 b.

6.4 HD 175679 b

From the joint constraint, HD 175679 b has a best-fit semi-major axis (a) of $3.36^{+0.12}_{-0.13}$ au, a mass of $62.2^{+15}_{-9.5}$ M_J, and an inclination of $39.2^{+6.2^\circ}_{-5.1}$ or $152.4^{+3.3^\circ}_{-4.4}$. Our fitting answers the remaining question in Wang et al. (2012): the companion is more likely to be a massive brown dwarf rather than a low-mass star. The best-fit orbit with RV and astrometry measurements is shown in figure 36.

7 Discussion

Hunting for extra companions in the known systems around evolved stars in OPSP was inspired by the increasing world of multiple-planet systems and their particular role in terms of the formation and evolution of planetary systems. The revisited systems were mostly published years ago, with only RV measurements covering several orbital phases. In addition, the masses of these central stars were estimated with coarse isochrones. Thus, we both refined the orbital parameter of the planets with new RVs, and the re-estimated properties of their central stars, so that stars and planets could be distributed in proper populations, and the RV residuals could be examined for extra signal.

In this section, we focus on the multiplicity of planetary systems around evolved stars. We investigate its correlation with the metallicity of host stars and the total mass of planets in the systems.

7.1 Sample selection

Our sample selection was based on a data crossing from both the Extrasolar Planets Encyclopaedia (Exoplanet.eu)[7] and NASA exoplanet archive.[8,9] We basically followed planetary systems and their parameters given by Exoplanet.eu, but we filled in the blanks in Exoplanet.eu if there were records provided by the NASA exoplanet archive or

7 ⟨http://exoplanet.eu/⟩.

8 ⟨https://exoplanetarchive.ipac.caltech.edu⟩.

9 We acquired the data on 2022 December 17.

Downloaded from https://academic.oup.com/pasj/article/75/6/1030/7272944 by ANKARA user on 22 December 2023

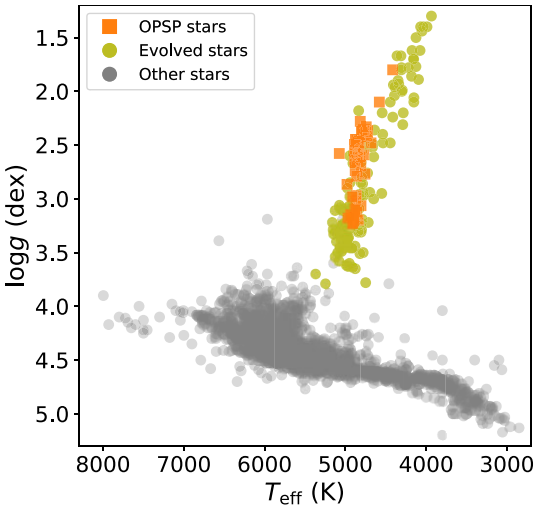


Fig. 37. HR diagram of planet-harboring stars. The evolved stars selected for this study are shown using color. Specifically, those observed in OPSP are shown with orange squares.

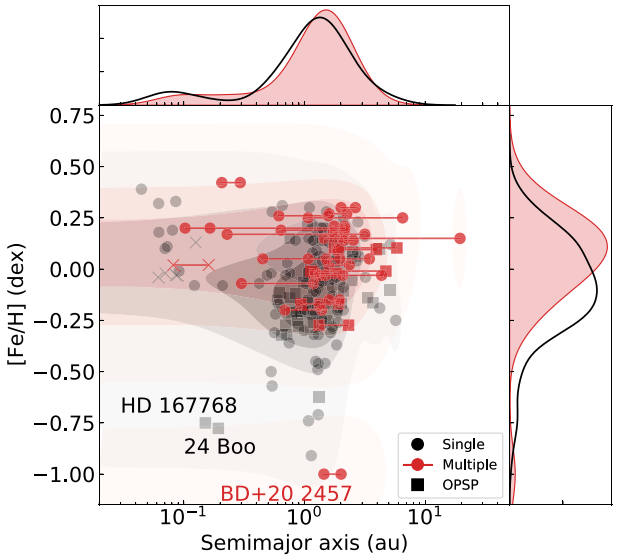


Fig. 38. Metallicity as a function of the semimajor axis for known planetary systems orbiting evolved stars. Each data point corresponds to a confirmed planet, with multiple-planet systems indicated with a red marker and connected by a straight line. Planets identified in OPSP are shown with squares, and those without a measured mass are indicated with a cross. All contour plots are flattened for visualization purposes, with red contours indicating multiple-planet systems and non-colored contours indicating single-planet systems.

SIMBAD.[10] We also supplemented the confirmed planetary systems in the NASA exoplanet archive to our samples if they did not emerge in Exoplanet.eu.

We selected planetary systems around evolved stars. The evolved stars were defined as $\log g < 3.8$ (less than one-fourth of the surface gravity of the Sun), $T_{\rm eff} < 5400$ K, and $R > 2R_\odot$ to ensure that host stars are evolved, and they should be out of the main sequence. Consequently, we obtained 172 planetary systems (figures 37 and 38), including 143 single-planet systems ($N_{\rm pl} = 1$) and 29 multiple-planet systems ($N_{\rm pl} \geq 2$), 156 systems detected by RVs, and 16 systems detected by transit.

For the selected samples, we believe that there would not be a large bias to cover planets having short or intermediate orbital periods of $P \lesssim 10^3$ d. This is because most of the systems were detected by RVs, whose observational time spans were normally longer than a few years, and those detected by transit in Kepler were also observed at a time scale of 4 yr. The current planet discoveries around evolved stars are all gas giant planets. The least massive one is Kepler-56 b (Huber et al. 2013), with a minimum mass of $M_{\rm p} = 0.06\ M_{\rm J}$.

In order to estimate the properties of planetary systems around evolved stars, we performed a bootstrap resampling, which is efficient for small samples that cannot be described by Gaussian distribution, or for samples whose distribution is unknown. We also expected that, via resampling, we could reduce the influence of extreme cases and recover less biased statistical properties, e.g., median value. We randomly shuffled all the selected systems 1×10^5 times, and we picked up $\lceil 2 \times \sqrt{N} \rceil = 27$ samples in each shuffle. In addition, we injected moderate Gaussian noises into the parameters of each sample. Specifically, we set $\sigma = 0.1$ dex to metallicity (the iron abundance [Fe/H]) of each host star, and $\sigma = 0.2\ M_{\rm p,\,tot}$ to the total planet mass in each system.

At first glance, we noted that the resampled metallicity is slightly higher than that directly calculated from the true 172 samples. The resampling revealed a mean and median of -0.04 ± 0.05 and -0.02 ± 0.06, respectively, while the true samples were -0.07 and -0.04. These are biased by planet-harboring stars with extremely low metallicity, e.g., HD 4760 (Niedzielski et al. 2021), BD +20 2457 (Niedzielski et al. 2009), etc.

7.2 Color cut-off bias in OPSP

Originally, a color cut-off of $0.6 \lesssim B - V \lesssim 1.0$ was adopted in OPSP star selection standards to achieve intrinsic RV stability of $\sigma \sim 20$ m s^{-1}. We basically kept this standard during the operation of the program, including the extensions of EAPS-Net. However, some studies revealed that a cut-off could result in the exclusion of the more metal-rich and low-gravity stars from the evolved star samples in different programs (Mortier et al. 2013; Wittenmyer et al. 2017). In addition, Mortier et al. (2013) calculated $B - V$ values with different given $\log g$ and [Fe/H] values for a given $T_{\rm eff}$ of 4850 K with a calibration of Sekiguchi and Fukugita (2000), which was summarized from 537 Infrared Space Observatory standard stars. Here, 4850 K is a typical temperature of an evolved star in OPSP and other planet

10 (http://simbad.u-strasbg.fr/simbad).

Downloaded from https://academic.oup.com/pasj/article/75/6/1030/7272944 by ANKARA user on 22 December 2023

surveys around evolved stars. From their calculation, a star having $\log g = 2.5$, a typical gravity in OPSP, will probably be ruled out with a $B - V < 1.0$ cut-off if the star has a higher [Fe/H] value. Since the metal-rich stars are ruled out due to the strong $B - V$ selection effect, planetary systems around metal-rich stars were not surveyed.

Similarly, we found that the OPSP planet-harboring stars tend to be more metal poor than the sample that we selected in the above subsection. We derived the mean and median of the metallicity (we hereafter use [Fe/H] for the metallicity) from bootstrap resampling and obtained -0.13 ± 0.08 and -0.12 ± 0.08, respectively. These values were lower than those of the whole evolved planet-harboring star samples of -0.04 ± 0.05 and -0.02 ± 0.06 at the $\lesssim 2$-σ level. A Kolmogorov–Smirnov test (K-S test; Kolmogorov 1933; Smirnov 1948) revealed a p-value equal to zero, which indicated a distinction between OPSP planet-harboring stars and the whole sample. Here, we note that the sample selected in the above subsection should be somewhat biased, because this sample was the most inclusive one among planetary systems around evolved stars, and it was obtained from a mixture of planetary systems around evolved stars from different surveys, including the RV survey and transit survey with different star selection criteria. But this sample provides enough evidence of the selection effect of the color cut-off of OPSP for its metal-poor contribution to the whole sample. Additionally, the shuffle in bootstrap resampling was uniformly conducted, which does not introduce a new selection effect when calculating the mean and median values. Therefore, we believe that our metallicity estimation can properly reflect the metal-poor selection effect due to the $B - V$ color cut-off in OPSP. Furthermore, we anticipate that a large unbiased sample with ∼50–100 planetary systems around evolved stars can be established in the future, and reliable statistics and a selection effect can be diagnosed within this sample.

The positive correlation between the occurrence of giant planets and metallicity could be concluded from surveys without a color cut-off, e.g., Reffert et al. (2015); Jones et al. (2016); Wittenmyer et al. (2016b). Wolthoff et al. (2022) recently investigated the aforementioned three surveys and also obtained a positive result in evolved stars. However, the color cut-off bias around evolved stars could lead to opposition, manifesting a null correlation. Wittenmyer et al. (2017) showed that the positive correlation could be hardly summarized from surveys, e.g., OPSP (Takeda et al. 2008; Mortier et al. 2013), which contained color cut-off to avoid redder stars. As for our OPSP, we have not yet completed the survey, and providing an updated correlation of giant planet occurrence within OPSP is out of the scope of this paper. The relevant study will be presented in a forthcoming paper.

The positive giant planet–metallicity correlation could be considered evidence for the core-accretion model (e.g., Pollack et al. 1996), in which planet formation requires solid materials to concrete a core before the accretion of gas in the protoplanetary disk, and thus higher stellar metallicity relates to the planet's higher formation rate. A mechanism independent from metallicity, e.g., gravitational instability (Boss 1997), in which a companion directly forms by the gravitational collapse of the gas without a solidified progenitor, can also contribute to planet formation.

Recently, some studies revealed that the gas giant companions of different masses might refer to different populations and form via different mechanisms. More specifically, planets as massive as Jupiter are likely to form via core accretion, while brown dwarfs or planets more massive than several Jupiter masses may form via gravitational disk instability. Schlaufman (2018) showed that planets or substellar companions more massive than a boundary (e.g., 10 $M_{\rm J}$) may not orbit metal-rich stars, and Maldonado & Villaver (2017) and Maldonado et al. (2019) confirmed that BD hosts do not show the giant planet–metallicity correlation. Santos et al. (2017); Adibekyan (2019) and Sousa et al. (2021) claimed different formation mechanisms of planets with masses above and below 4 $M_{\rm J}$, and Adibekyan (2019) also argued that planets of the same (high) mass could be formed through different channels. Thus, the planet-metallicity correlation should be a key to the formation scenario of giant planets.

7.3 Metallicity and multiplicity

Fischer and Valenti (2005) first pointed out that high stellar metallicity appeared to be correlated with the presence of multiple-planet systems. In this study, we tested this trend on evolved stars.

First, we divided the whole samples into single-planet systems (hereafter singles) and multiple-planet systems (hereafter multis). The resampling revealed that the number ratio of multis to singles around evolved stars was 0.21 ± 0.10, which is lower than that of all detected planetary systems (∼0.28 by exoplanet.eu). Qualitatively, as a planetary system and its host star evolve, the system could lose a planet(s) due to tidal interactions between the planet(s) and its host stars, between planets, or between the planet(s) and fly-by body(ies). Thus, the ratio of multis to singles should be averagely lower at the higher evolutionary stage of the planetary systems.

For metallicity, the resampling revealed that the mean metallicities of multis and singles were respectively 0.04 ± 0.12 and -0.09 ± 0.06, suggesting that multis should be averagely more metal rich (figure 39). A K-S test with a p-value equal to zero revealed the distinction between the

Downloaded from https://academic.oup.com/pasj/article/75/6/1030/7272944 by ANKARA user on 22 December 2023

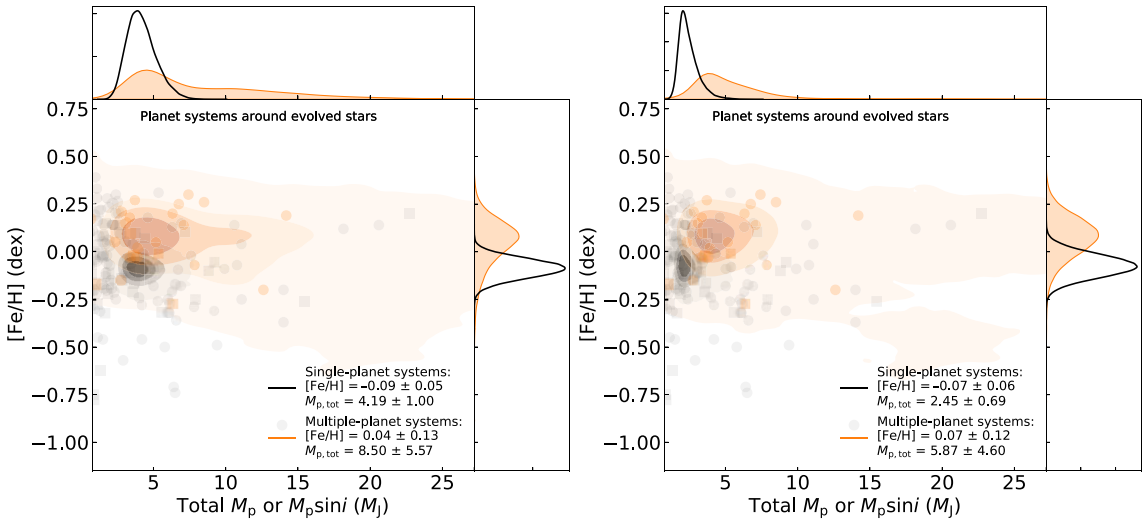


Fig. 39. Distribution of the resampled metallicity against the total planet mass for all selected planetary systems around evolved stars. (Left: Distribution of mean values. Right: Distribution of median values.) The orange contours refer to multiple-planet systems while non-colored contours refer to single-planet systems. The scattered plots are the selected planetary systems around evolved stars to generate the resampling.

two samples. The resampling also revealed that the average total planet mass of multis is slightly higher than that of singles. But it should be noted that the mean value might not reflect the actual case. The masses of gas giant companions and the metallicity of host stars differ significantly. A brown dwarf can be $\sim 10^2$ times more massive than a Saturn-mass planet, and a planet-harboring star in the galactic thick disk is averagely more metal poor than that in the galactic thin disk. Therefore, we checked the median values of metallicity and total planet mass from the resampling. Similarly, multis appeared to be more metal rich and more massive than singles. But the median total masses of both multis and singles were significantly lower than the mean values by a few Jupiter masses, which indicated the overestimation in total masses by the mean value.

As introduced in the previous subsection, the occurrence of planets as massive as Jupiter tends to agree well with the giant planet–metallicity correlation, while the occurrence of massive gas companions does not. Hence, we further focused on planetary systems containing Jupiter-mass planets. We restricted each system's mean planet mass to a maximum of 5 M_J (for simplicity, we call them Jupiter-mass planets), and we examined the metallicity, multiplicity, and total planet mass. Consequently, the resampling revealed mean metallicities of 0.09 ± 0.11 and -0.05 ± 0.06, and mean total planet masses of 4.31 ± 1.42 M_J and 1.90 ± 0.29 M_J for multis and singles, respectively (figure 40). The median metallicities were illustrated similarly by 0.09 ± 0.11 and -0.04 ± 0.06 for multis and singles, respectively. Meanwhile, the mass difference between the median and mean was reduced to <0.3 M_J with the restriction to the planet masses (figure 40). Both revealed the trend that metallicity positively correlates with multiplicity and total planet mass for planetary systems having Jupiter-mass planets. As the formation of the core of a Jupiter-like planet depends on the metallicity of the star and its disk, we thus believe that the positive correlation can be considered evidence for the core-accretion model (e.g., Ida & Lin 2004).

Moreover, we became interested in two planetary systems during our discussions on planetary systems having Jupiter-mass planets. The systems, 24 Boo and HD 167768, have been identified as single stars but with potential planet candidates, as indicated by our current work and previous research (Teng et al. 2023). Both host stars belong to the thick disc metal-poor population with [Fe/H] $\lesssim -0.7$ but enhanced alpha element abundances. To investigate the impact of these two systems, we conducted additional resampling by considering them as multis, utilizing the masses of the planet candidates (two for 24 Boo and two for HD 167768) obtained from this study and Teng et al. (2023). Consequently, we confirmed a marginal positive correlation between metallicity and multiplicity/total mass, but the mean and median metallicities of multis decreased by 0.07 and 0.04 dex, respectively, compared to when these systems were assumed to be singles (figure 41).

Thus, according to the rare cases of 24 Boo and HD 167768, we hereby raise three questions in this paper.

(1) Is [Fe/H] the best (or a proper) parameter to describe the metallicity of a planetary system?
(2) Does a giant planet in the galactic thick disk refer to the same planet population as that in the thin disk?

Downloaded from https://academic.oup.com/pasj/article/75/6/1030/7272944 by ANKARA user on 22 December 2023

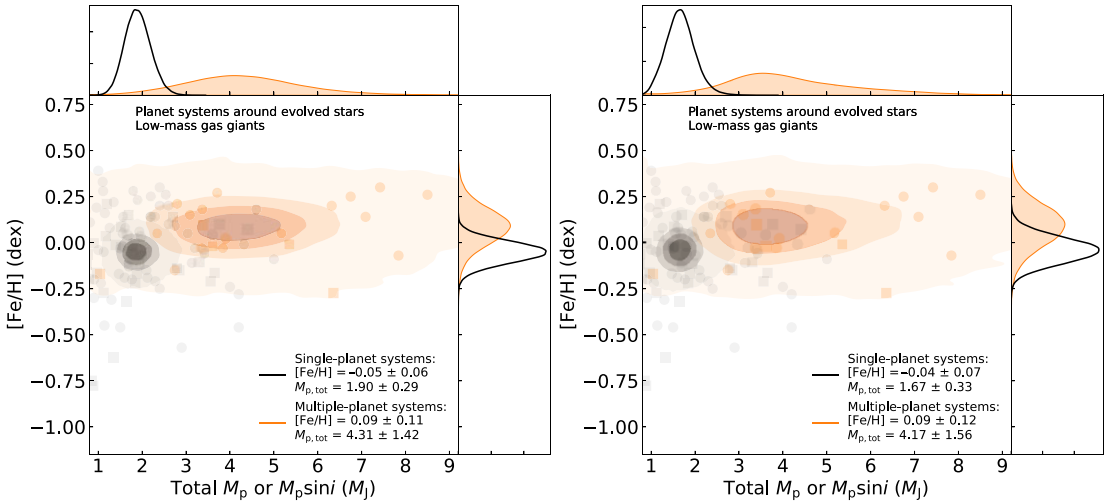


Fig. 40. Distribution of the resampled metallicity against the total planet mass for planetary systems harboring Jupiter-mass planets around evolved stars. Left: Distribution of mean values. Right: Distribution of median values. The orange contours refer to multiple-planet systems while non-colored contours refer to single-planet systems. The scattered plots are the selected planetary systems around evolved stars to generate the resampling.

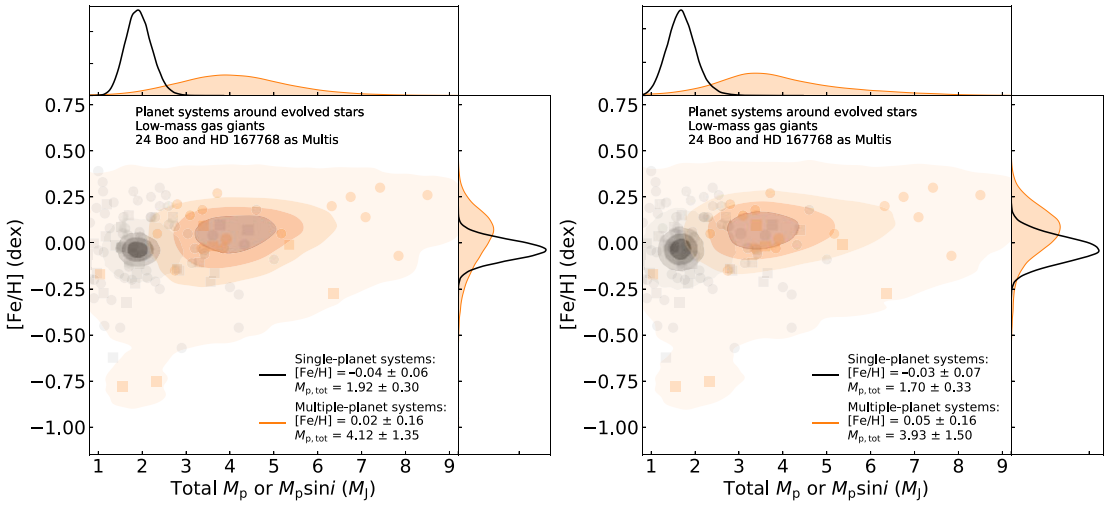


Fig. 41. Distribution of the resampled metallicity against the total planet mass for planetary systems harboring Jupiter-mass planets around evolved stars, and 24 Boo and the HD 167768 system as multiple-planet systems. Left: Distribution of mean values. Right: Distribution of median values. The orange contours refer to multiple-planet systems while non-colored contours refer to single-planet systems. The scattered plots are the selected planetary systems around evolved stars to generate the resampling.

(3) If a giant planet in the thick disk forms via the core-accretion mechanism, is the core composition the same or different from that of planets in the thin disk?

Answering these questions is out of the scope of this data-release paper.

8 Summary

In the present study, we revisited 32 evolved stars known to harbor planets, as part of the OPSP and its extended collaborative network, the EAPS-Net, using the most recent precise RV measurements obtained at OAO.

We confirmed one new wide-orbit planet in the known 75 Cet system (75 Cet c; $P = 2051.62$ d, $M_p \sin i = 0.91\ M_J$), and we confirmed the RV long-term trends in five stars (HD 5608, κ CrB, HD 167042, 18 Del, and HD 208897), which indicates the possible outer massive companions. Additionally, we further investigated the RV variability of 11 stars for different reasons.

(1) For ϵ Tau, 11 Com, and 24 Boo, we detected additional periodic RV variations.
(2) For 41 Lyn and 14 And, we found that line profiles synchronously vary with RV over time.

Downloaded from https://academic.oup.com/pasj/article/75/6/1030/7272944 by ANKARA user on 22 December 2023

(3) For HD 32518 and ω Ser, we showed that the amplitudes of RV variations are not stable over different data sets.
(4) For HD 5608, HD 14067, HD 120084, and HD 175679, we jointly constrained the orbital parameters by RVs and astrometry data.

Furthermore, our analysis has provided confirmation that the strict $B - V$ color cut-off employed in OPSP resulted in a sample that is more metal deficient. This conclusion was drawn from a comparison between planetary systems discovered in OPSP and a complete sample of planetary systems that exist around evolved stars. Most significantly, our investigation of the complete sample reveals a tendency for metal-rich stars to possess a greater number of multiple-planet systems with a higher total planetary mass. This correlation is particularly pronounced in planetary systems that contain Jupiter-mass planets, which can be strong evidence for the core-accretion planet formation model.

Supplementary data

The following supplementary data are available at *PASJ* online: all RV and other spectral measurements in CSV and text formats.

Acknowledgments

This research is primarily based on data collected at OAO, which is operated by the National Astronomical Observatory of Japan. We are grateful to all the staff members at OAO for their support during the observations. We thank the observatory for allowing us to use the data obtained during the engineering times at OAO, including a portion of observations of the RV standard star τ Cet, ι Per, and ϵ Vir. We thank the students of Tokyo Institute of Technology and Kobe University for their kind help with the observations at OAO. I.B., S.S., and M.Y. are grateful to TÜBİTAK National Observatory, IKI, KFU, and AST for their partial support in using RTT-150 (Russian-Turkish 1.5 m telescope in Antalya). We express our special thanks to Yoichi Takeda for support with the stellar property analysis. We thank John A. Johnson, Brendan P. Bowler, Debra A. Fischer, and Andrew W. Howard for their kind help with the RV data observed at Lick observatory. We thank the anonymous referee for valuable comments and suggestions that helped to improve the manuscript.

This research adopted data obtained from the Maunakea observatory. The authors wish to recognize and acknowledge the very significant cultural role and reverence that the summit of Maunakea has always had within the indigenous Hawaiian community. We are most fortunate to have the opportunity to conduct observations from this mountain.

B.S. was partially supported by the MEXT program "Promotion of Environmental Improvement for Independence of Young Researchers" under the Special Coordination Funds for Promoting Science and Technology, by Grant-in-Aid for Young Scientists (B) No. 17740106 and No. 20740101, Grant-in-Aid for Scientific Research (C) No. 23540263, Grant-in-Aid for Scientific Research on Innovative Areas No. 18H05442 from the Japan Society for the Promotion of Science (JSPS), and by Satellite Research in 2017-2020 from the Astrobiology Center, NINS. H.I. was supported by JSPS KAKENHI Grants No. JP16H02169 and No. JP23244038. M.Y. was supported by the Scientific and Technological Research Council of Turkey (TÜBİTAK), under Project No. 114F099. I.B. was financed by subsidy FZSM-2023-0015 of the Ministry of Education and Science of the Russian Federation allocated to the Kazan Federal University for the State assignment in the sphere of scientific activities.

This research has made use of IRAF. It is distributed by the National Optical Astronomy Observatories, which is operated by the Association of Universities for Research in Astronomy, Inc. under a cooperative agreement with the National Science Foundation, USA. This research made use of the following `Python` packages for scientific calculation:

(1) for randomization, likelihood maximization, MAP, and the K-S test, we used `NumPy` (Harris et al. 2020) and `SciPy` (Virtanen et al. 2020),
(2) for the GLS periodogram, we used `astropy` (Astropy Collaboration 2013),
(3) for stellar properties, we used `isoclassify` (Huber et al. 2017),
(4) for the Keplerian orbital fit, we used `RadVel` (Fulton et al. 2018)[11], `htof` (Brandt 2021), and `orvara` (Brandt et al. 2021),
(5) for GP, we used `celerite` (Foreman-Mackey et al. 2017),
(6) for MCMC sampling, we used `emcee` (Foreman-Mackey et al. 2013) and `ptemcee` (Foreman-Mackey et al. 2013; Vousden et al. 2016).

This research made use of the SIMBAD database, operated at CDS, Strasbourg, France. This work made use of data from the European Space Agency (ESA) mission Gaia ⟨https://www.cosmos.esa.int/gaia⟩, processed by the Gaia Data Processing and Analysis Consortium (DPAC, https://www.cosmos.esa.int/web/gaia/dpac/consortium). Funding for the DPAC has been provided by national institutions, in particular, the institutions participating in the Gaia Multilateral Agreement. This research made use of the NASA Exoplanet Archive, which is operated by the California Institute of Technology, under contract with the National Aeronautics and Space Administration under the Exoplanet Exploration Program. This research made use of data obtained from tools provided by the portal exoplanet.eu of the Extrasolar Planets Encyclopedia.

Appendix 1 Instrumental stability of HIDES

The instrumental stabilities of HIDES-S and HIDES-F1 were examined and discussed in Teng et al. (2022a). With RV standard stars, we ensured that HIDES-S and HIDES-F1 could be stable with their individual modes at a level of $\lesssim 4$ m s^{-1}. Here, we examine the stability of HIDES-F2 independently and the 20-yr long-term stability of HIDES with a combination of three individual observation modes. We note that a slight order shift happened to the CCD in 2019 November due to an earthquake near the observatory; hence, we also separately examine the stability of HIDES-F2 pre- and post-earthquake.

Three different RV standard stars were adopted to examine the instrumental stability of HIDES-F2 (figure 42). τ Cet (HD 10700, G8 V, $V = 3.5$), known to have stable RV

11 Fulton, B. J., & Petigura, E. 2017, RadVel: Radial Velocity Fitting Toolkit ⟨https://doi.org/10.5281/zenodo.580821⟩.

Downloaded from https://academic.oup.com/pasj/article/75/6/1030/7272944 by ANKARA user on 22 December 2023

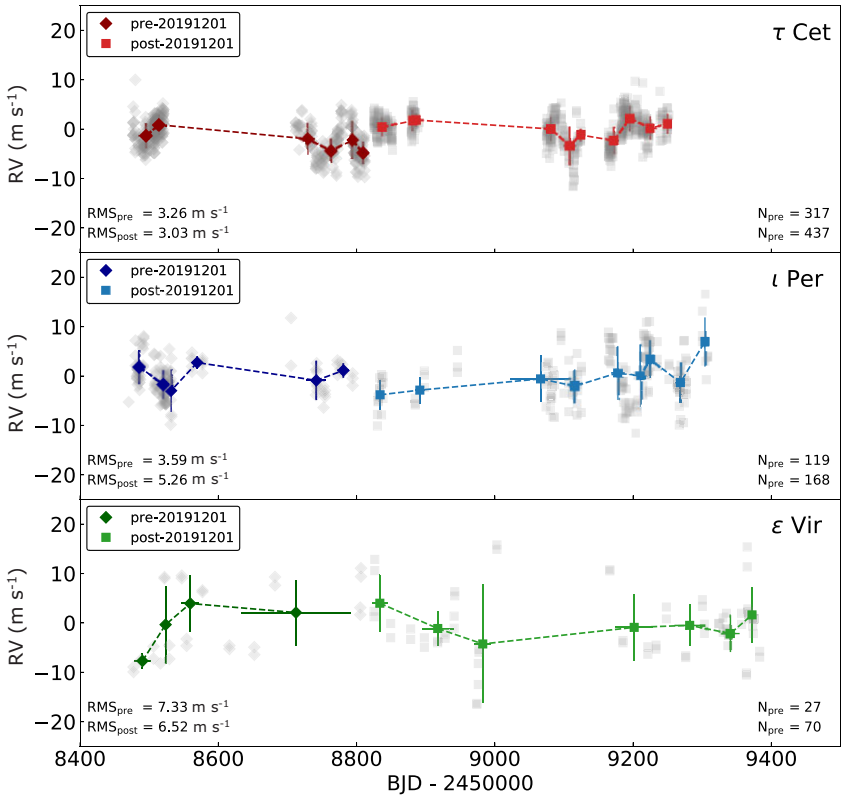


Fig. 42. RVs of τ Cet, ι Per, and ϵ Vir obtained by HIDES-F2. Single measurements are shown with non-colored markers, and binned measurements are shown with colored markers connected by dashed lines for an indication of trends. We use 20191201 to indicate the earthquake, and HIDES was not scheduled between 2019 November 25 and 2019 December 6.

among solar-type stars, was set to be one of the RV standard stars in this study. The typical exposure time of τ Cet was set to be 5 min, and the RVs were all measured from the same reference spectrum. Consequently, we obtained root mean squares pre- and post-earthquake of 3.26 m s^{-1} ($N_{\rm obs} = 317$) and 3.03 m s^{-1} ($N_{\rm obs} = 437$), and we did not observe significant RV offset between the occurrence of the earthquake. This suggested the negligible influence of the order shift due to the earthquake for stars that emerged in OPSP. Similarly, we examined the stabilities of another two RV standard stars ι Per (HD 19373, G0 V, $V = 4.05$) and ϵ Vir (HD 113226, G8 III, $V = 2.79$) in OPSP (Sato et al. 2005). Two stars showed typical errors of 3–7 m s^{-1} and negligible RV difference pre- and post-earthquake for stars that emerged in OPSP.

To search for instrumental variations, we calculated the GLS periodogram of the full RVs of the three RV standard stars. As shown in figure 43, we discovered a significant variation of approximately two months from RVs of both τ Cet and ι Per with estimated amplitudes of $\lesssim 3$ m s^{-1}. However, such a variation could not be derived from ϵ Vir RVs and some previous studies on τ Cet, e.g., the planet discovery of τ Cet with HARPS and Keck (Feng et al. 2017). Therefore, we infer that the two-month variation with low amplitude might be introduced from the instrument itself.

As for the stability of HIDES over 20 yr, it was diagnosed by RVs of τ Cet for its mild RV variation and long-term stability. We re-extracted the RVs obtained by HIDES-S, HIDES-F1, and HIDES-F2 with the same reference spectrum, and we empirically eliminated the RVs with observational errors over 6 m s^{-1}. As shown in figure 44, we could apparently observe an offset between HIDES-S and HIDES-F1, HIDES-F2 at a maximum of ~ 5 m s^{-1}, and an offset between HIDES-F1 and HIDES-F2 of ~ 2.5 m s^{-1}. In most cases, we could ignore the instrumental RV offsets by setting them as free parameters in the Keplerian orbital fit. In this study, it was not suggested to simply ignore the RV offsets for stars showing astrometric accelerations, because we could trace astrometric accelerations with long-term consecutive RV monitoring based on a unified zero point.

In the case of HIDES, however, the RV standard stars were sparsely observed by HIDES-S and HIDES-F1. It was thus never a good strategy to fit and remove the trends with lines or curvatures because of the overcorrection to the zero point. Instead, we could adopt a more moderate correction by ignoring the slight instrumental RV variations inside individual observation modes but shifting the RV offsets between individual modes based on the mean level. This had two primary benefits in this study.

Downloaded from https://academic.oup.com/pasj/article/75/6/1030/7272944 by ANKARA user on 22 December 2023

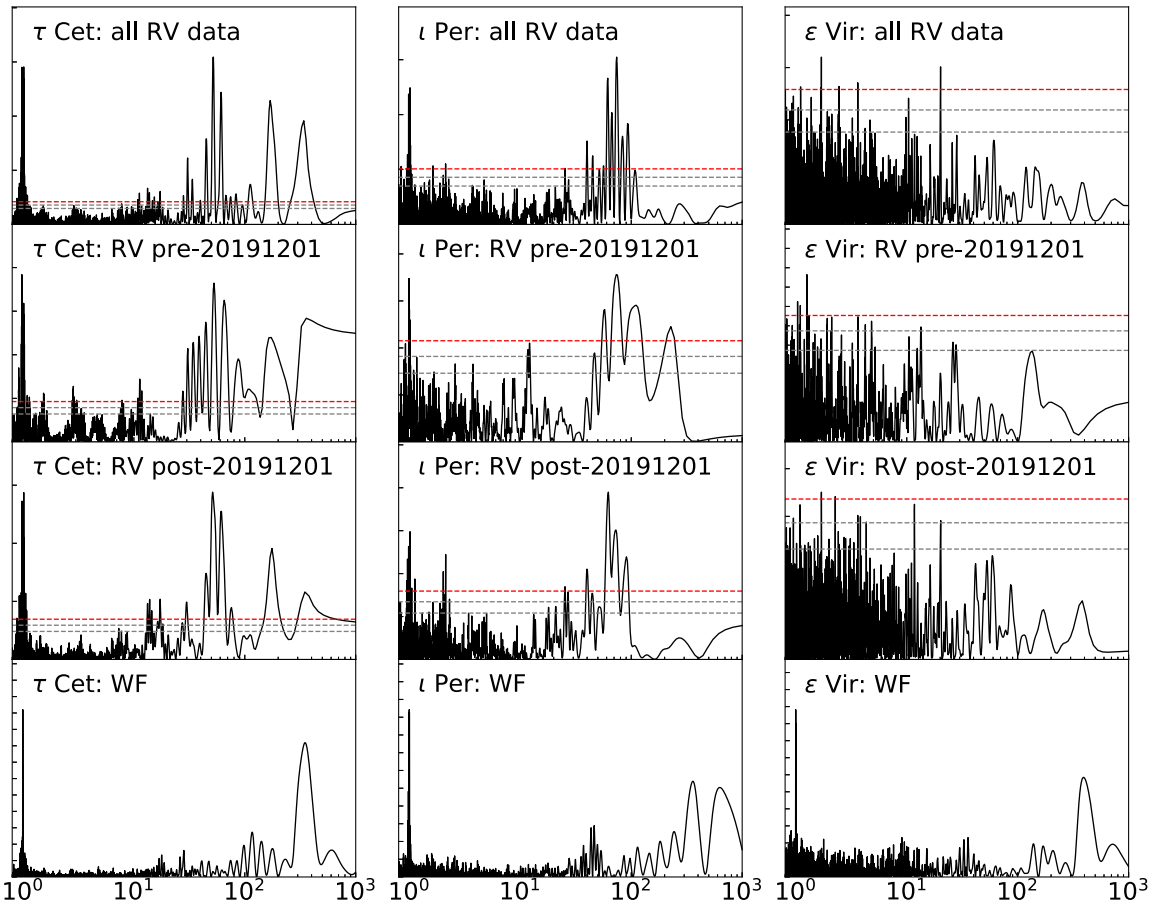


Fig. 43. GLS periodograms of RVs of τ Cet (left panel), ι Per (middle panel), and ϵ Vir (right panel) obtained by HIDES-F2. In each panel, we present the GLS periodograms of each star derived from different data sets and the window function. In each subplot, the horizontal lines represent 10%, 1%, and 0.1% FAP levels from bottom to top.

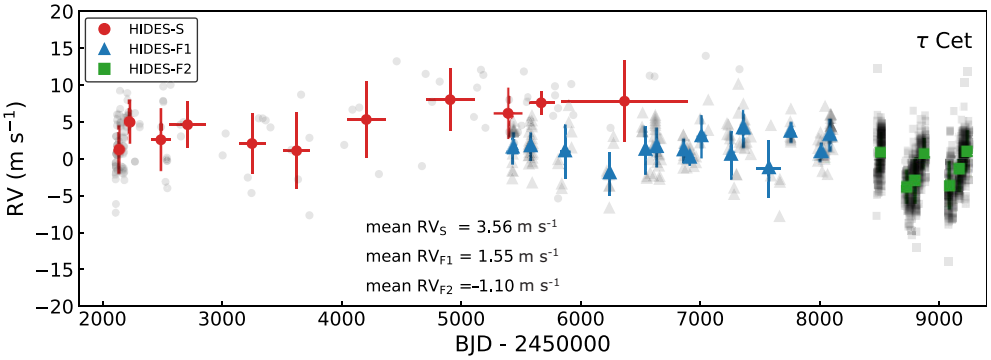


Fig. 44. RVs of τ Cet measured by a unified reference spectrum. Single measurements are shown with non-colored markers, and binned measurements are shown with colored markers.

(1) It did not influence the RV orbit fitting in subsection 3.4 since, as mentioned before, the RV offsets to an arbitrary zero point in the Keplerian model were set to be free parameters.
(2) It moderately flattened the RV offsets between different observation modes so that the RV variations of the revisited stars can be well described in the longest time scale of 20 yr.

This moderate correction was applied to four systems (HD 5608, HD 14067, HD 120084, and HD 175679; see section 6) when we performed the joint constraint with RV and astrometry.

Downloaded from https://academic.oup.com/pasj/article/75/6/1030/7272944 by ANKARA user on 22 December 2023

Appendix 2 RV fitting results for normal stars

In this section, we present the Keplerian orbital solutions to the normal stars, which are not concretely described in the main text (sections 4, 5, and 6). In figures 45, 46, and 47, we present the orbits of single-planet systems, including HD 2952, HD 4732, HD 16400, 6 Lyn, 4 Uma, o Uma, HD 104985, o CrB, HD 145457, HD 173416, HD 180314, ξ Aql, and HD 210702. In figure 48, we present the orbits of double-planet systems, including HD 4732, HD 47366, γ Lib, and ν Oph.

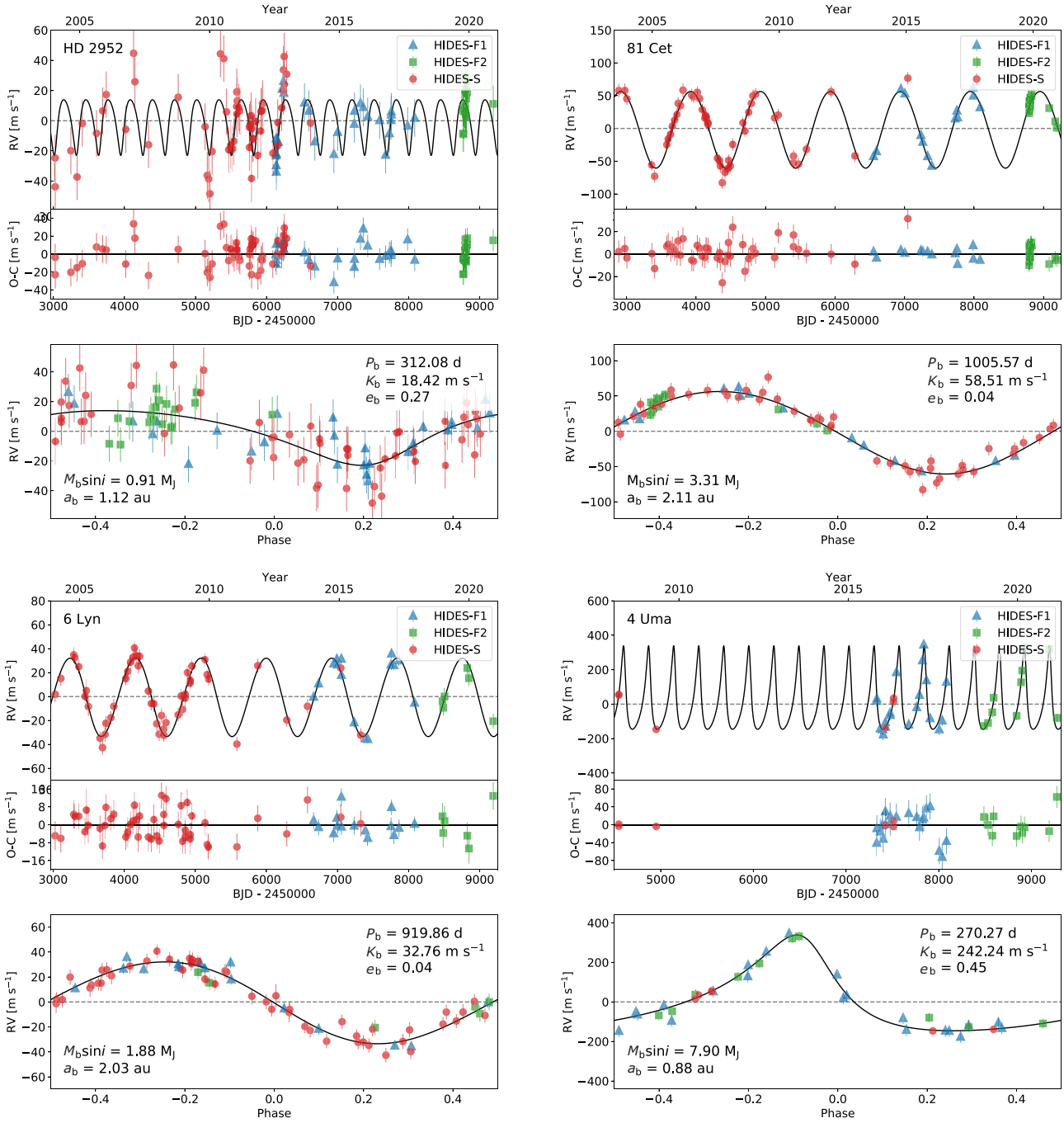


Fig. 45. Keplerian orbital fits to HD 2952, HD 4732, HD 16400, 6 Lyn, and 4 Uma.

Downloaded from https://academic.oup.com/pasj/article/75/6/1030/7272944 by ANKARA user on 22 December 2023

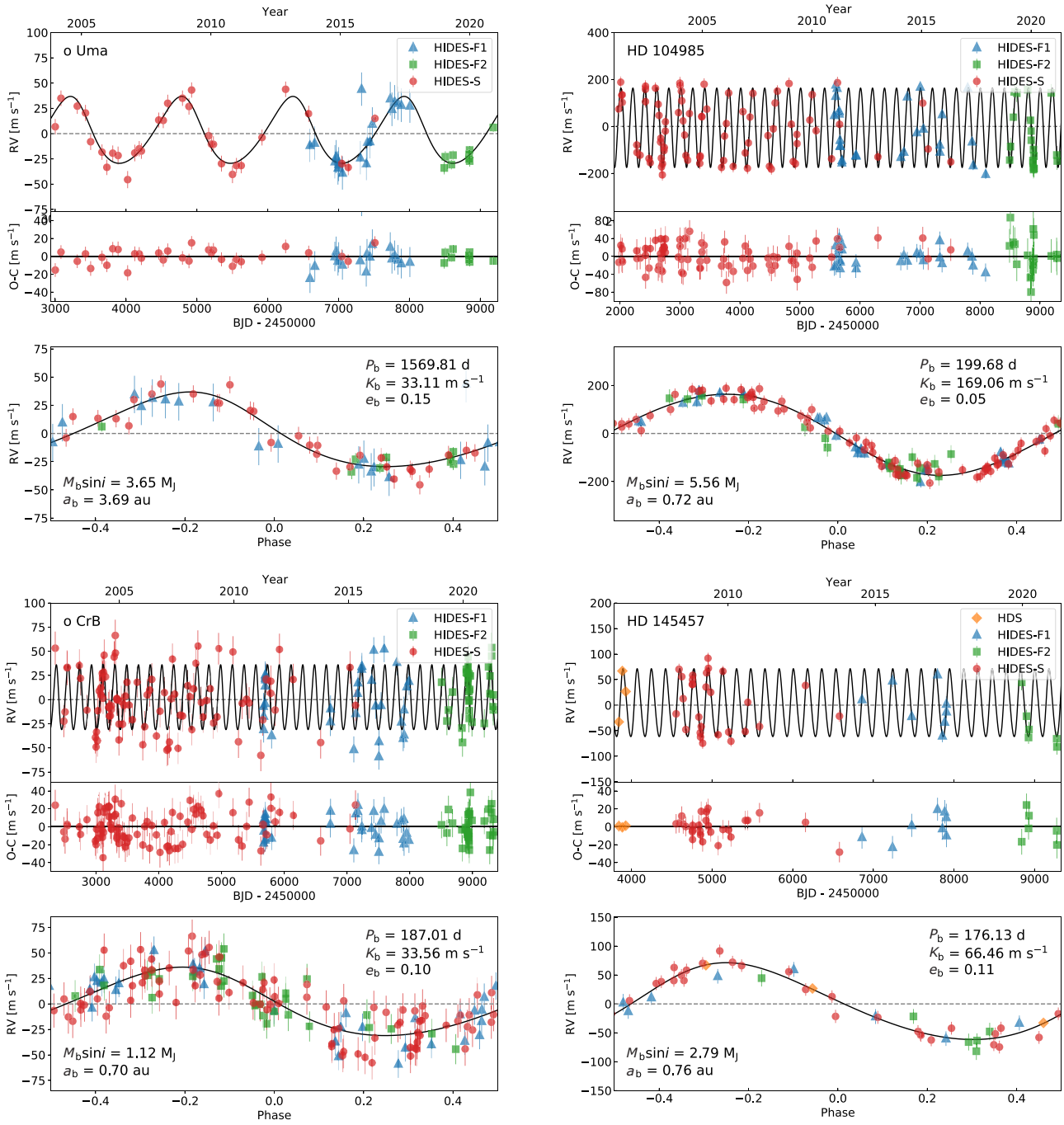


Fig. 46. Keplerian orbital fits to o Uma, HD 104985, o CrB, and HD 145457.

Downloaded from https://academic.oup.com/pasj/article/75/6/1030/7272944 by ANKARA user on 22 December 2023

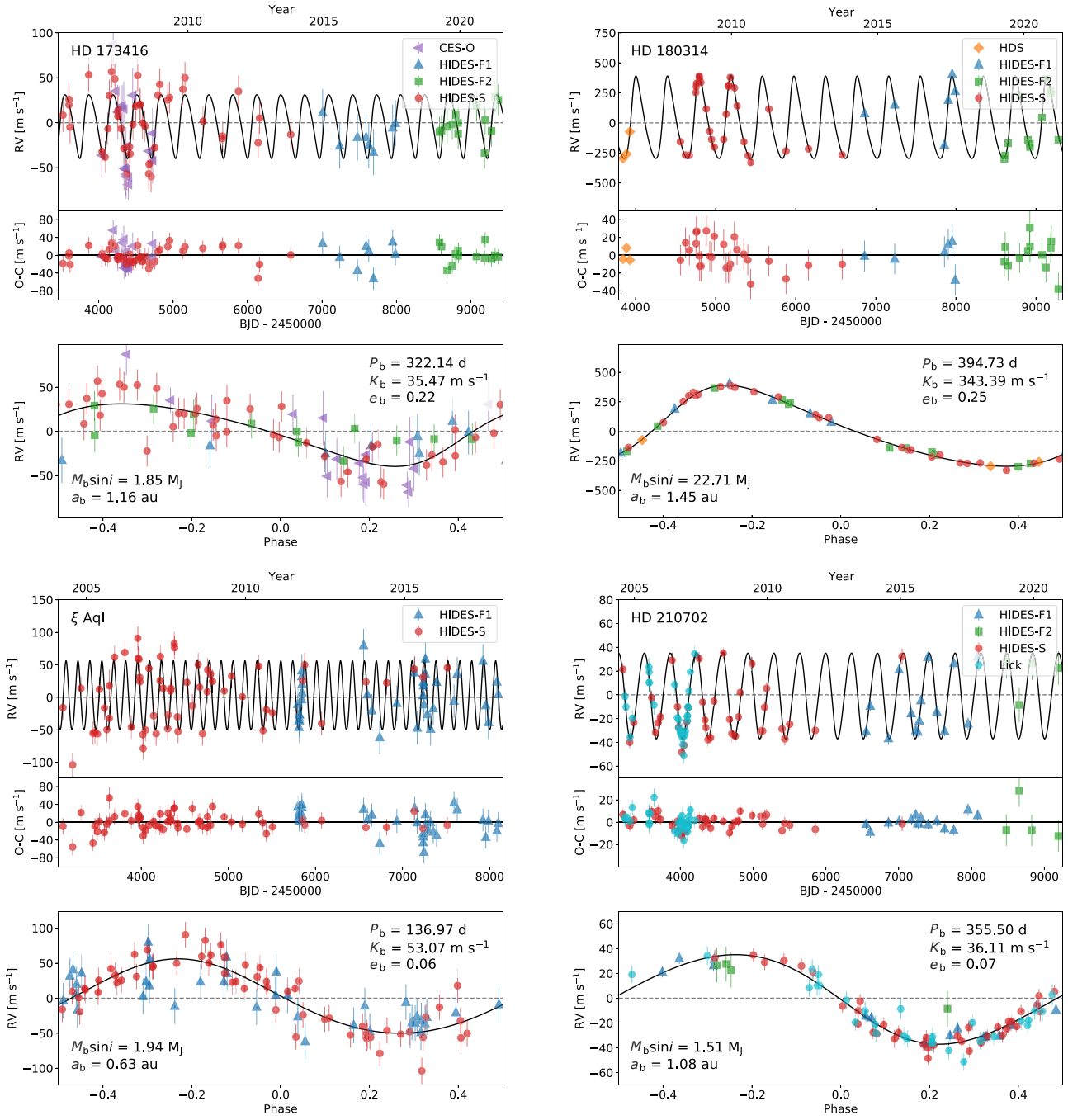


Fig. 47. Keplerian orbital fits to HD 173416, HD 180314, ξ Aql, and HD 210702.

Downloaded from https://academic.oup.com/pasj/article/75/6/1030/7272944 by ANKARA user on 22 December 2023

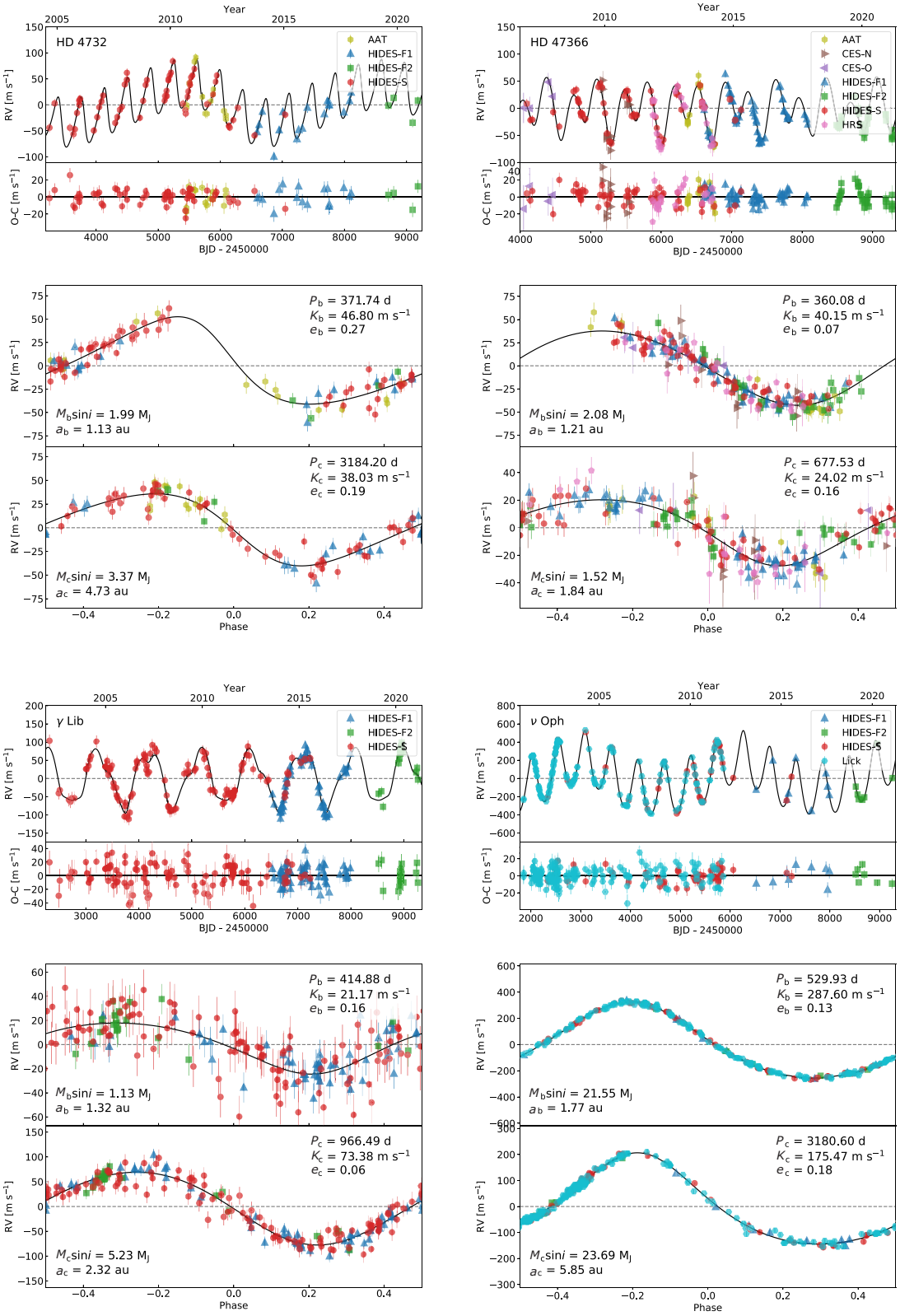


Fig. 48. Keplerian orbital fits to HD 4732, HD 47366, γ Lib, and ν Oph.

Downloaded from https://academic.oup.com/pasj/article/75/6/1030/7272944 by ANKARA user on 22 December 2023

References

Adibekyan, V. 2019, Geosciences, 9, 105
Ando, H., Tsuboi, Y., Kambe, E., & Sato, B. 2010, PASJ, 62, 1117
Andrews, S. M., Rosenfeld, K. A., Kraus, A. L., & Wilner, D. J. 2013, ApJ, 771, 129
Arentoft, T., et al. 2019, A&A, 622, A190
Astropy Collaboration 2013, A&A, 558, A33
Baluev, R. V. 2008, MNRAS, 385, 1279
Baranne, A., et al. 1996, A&AS, 119, 373
Bonsor, A., Kennedy, G. M., Crepp, J. R., Johnson, J. A., Wyatt, M. C., Sibthorpe, B., & Su, K. Y. L. 2013, MNRAS, 431, 3025
Boss, A. P. 1997, Science, 276, 1836
Bowler, B. P., et al. 2010, ApJ, 709, 396
Brandt, T. D. 2018, ApJS, 239, 31
Brandt, T. D. 2021, ApJS, 254, 42
Brandt, T. D., Dupuy, T. J., Li, Y., Brandt, G. M., Zeng, Y., Michalik, D., Bardalez Gagliuffi, D. C., & Raposo-Pulido, V. 2021, AJ, 162, 186
Bryan, M. L., et al. 2016, ApJ, 821, 89
Butler, R. P., Marcy, G. W., Williams, E., McCarthy, C., Dosanjh, P., & Vogt, S. S. 1996, PASP, 108, 500
Chambers, J. E. 1999, MNRAS, 304, 793
Delisle, J.-B., & Ségransan, D. 2022, A&A, 667, A172
Diego, F., Charalambous, A., Fish, A. C., & Walker, D. D. 1990, Proc. SPIE, 1235, 562
Döllinger, M. P., Hatzes, A. P., Pasquini, L., Guenther, E. W., Hartmann, M., Girardi, L., & Esposito, M. 2007, A&A, 472, 649
Döllinger, M. P., Hatzes, A. P., Pasquini, L., Guenther, E. W., & Hartmann, M. 2009, A&A, 505, 1311
Duncan, D. K., et al. 1991, ApJS, 76, 383
ESA 1997, The Hipparcos and Tycho Catalogues, vol. 1200 (Noordwijk: ESA Publications Division)
Feng, F., et al. 2022, ApJS, 262, 21
Feng, F., Lisogorskyi, M., Jones, H. R. A., Kopeikin, S. M., Butler, R. P., Anglada-Escudé, G., & Boss, A. P. 2019, ApJS, 244, 39
Feng, F., Tuomi, M., Jones, H. R. A., Barnes, J., Anglada-Escudé, G., Vogt, S. S., & Butler, R. P. 2017, AJ, 154, 135
Fischer, D. A., & Valenti, J. 2005, ApJ, 622, 1102
Foreman-Mackey, D., Agol, E., Ambikasaran, S., & Angus, R. 2017, AJ, 154, 220
Foreman-Mackey, D., Hogg, D. W., Lang, D., & Goodman, J. 2013, PASP, 125, 306
Frink, S., Quirrenbach, A., Fischer, D., Röser, S., & Schilbach, E. 2001, PASP, 113, 173
Fulton, B. J., Petigura, E. A., Blunt, S., & Sinukoff, E. 2018, PASP, 130, 044504
Giguere, M. J., Fischer, D. A., Payne, M. J., Brewer, J. M., Johnson, J. A., Howard, A. W., & Isaacson, H. T. 2015, ApJ, 799, 89
Gray, R. O., & Corbally, C. J. 1994, AJ, 107, 742
Haisch, K. E., Lada, E. A., & Lada, C. J. 2001a, AJ, 121, 2065
Haisch, K. E., Lada, E. A., & Lada, C. J. 2001b, ApJ, 553, L153
Han, I., Lee, B. C., Kim, K. M., Mkrtichian, D. E., Hatzes, A. P., & Valyavin, G. 2010, A&A, 509, A24
Harris, C. R., et al. 2020, Nature, 585, 357
Hatzes, A. P., et al. 2018, AJ, 155, 120
Hatzes, A. P., Guenther, E. W., Endl, M., Cochran, W. D., Döllinger, M. P., & Bedalov, A. 2005, A&A, 437, 743
Heeren, P., et al. 2021, A&A, 647, A160
Holman, M., Touma, J., & Tremaine, S. 1997, Nature, 386, 254
Huber, D., et al. 2017, ApJ, 844, 102
Huber, D., et al. 2013, Science, 342, 331
Ida, S., & Lin, D. N. C. 2004, ApJ, 616, 567
Izumiura, H. 2005, J. Korean Astron. Soc., 38, 81
Izumiura, H. 1999, Publ. Yunnan Obs., Suppl., 77
Jeong, G., et al. 2018, A&A, 610, A3
Jofré, E., Petrucci, R., Saffe, C., Saker, L., Artur de la Villarmois, E., Chavero, C., Gómez, M., & Mauas, P. J. D. 2015, A&A, 574, A50
Johnson, J. A., et al. 2011, ApJS, 197, 26
Johnson, J. A., et al. 2007, ApJ, 665, 785
Jones, M. I., et al. 2016, A&A, 590, A38
Jones, M. I., Jenkins, J. S., Rojo, P., & Melo, C. H. F. 2011, A&A, 536, A71
Kambe, E., et al. 2013, PASJ, 65, 15
Kass, R. E., & Raftery, A. E. 1996, J. Am. Statist. Assoc., 90, 430, 773
Kiefer, F., et al. 2019, A&A, 631, A125
Kiefer, F., Hébrard, G., Lecavelier des Etangs, A., Martioli, E., Dalal, S., & Vidal-Madjar, A. 2021, A&A, 645, A7
Kjeldsen, H., & Bedding, T. R. 1995, A&A, 293, 87
Kolmogorov, A. 1933, Giornale dell'Istituto Italiano degli Attuari, 4, 83
Lagrange, A.-M., Desort, M., Galland, F., Udry, S., & Mayor, M. 2009, A&A, 495, 335
Li, Y., et al. 2021, AJ, 162, 266
Liu, Y.-J., et al. 2008, ApJ, 672, 553
Liu, Y.-J., Sato, B., Zhao, G., & Ando, H. 2009, Res. Astron. Astrophys., 9, 1
Luque, R., et al. 2019, A&A, 631, A136
Maldonado, J., & Villaver, E. 2017, A&A, 602, A38
Maldonado, J., Villaver, E., Eiroa, C., & Micela, G. 2019, A&A, 624, A94
Mittag, M., Schmitt, J. H. M. M., & Schröder, K.-P. 2018, A&A, 618, A48
Mortier, A., Santos, N. C., Sousa, S. G., Adibekyan, V. Z., Delgado Mena, E., Tsantaki, M., Israelian, G., & Mayor, M. 2013, A&A, 557, A70
Mugrauer, M., Ginski, C., & Seeliger, M. 2014, MNRAS, 439, 1063
Mustill, A. J., & Wyatt, M. C. 2009, MNRAS, 399, 1403
Nelder, J. A., & Mead, R. 1965, Comput. J., 7, 308
Niedzielski, A., et al. 2007, ApJ, 669, 1354
Niedzielski, A., et al. 2015a, A&A, 573, A36
Niedzielski, A., Nowak, G., Adamów, M., & Wolszczan, A. 2009, ApJ, 707, 768
Niedzielski, A., Wolszczan, A., Nowak, G., Adamów, M., Kowalik, K., Maciejewski, G., Deka-Szymankiewicz, B., & Adamczyk, M. 2015b, ApJ, 803, 1
Niedzielski, A., Villaver, E., Adamów, M., Kowalik, K., Wolszczan, A., & Maciejewski, G. 2021, A&A, 648, A58
Noguchi, K., et al. 2002, PASJ, 54, 855
Omiya, M., et al. 2012, PASJ, 64, 34
Omiya, M., et al. 2009, PASJ, 61, 825

Downloaded from https://academic.oup.com/pasj/article/75/6/1030/7272944 by ANKARA user on 22 December 2023

Pepe, F., Mayor, M., Galland, F., Naef, D., Queloz, D., Santos, N. C., Udry, S., & Burnet, M. 2002, A&A, 388, 632
Pollack, J. B., Hubickyj, O., Bodenheimer, P., Lissauer, J. J., Podolak, M., & Greenzweig, Y. 1996, Icarus, 124, 62
Queloz, D., et al. 2001, A&A, 379, 279
Quirrenbach, A., Reffert, S., & Bergmann, C. 2011, AIP Conf. Ser., 1331, 102
Quirrenbach, A., Trifonov, T., Lee, M. H., & Reffert, S. 2019, A&A, 624, A18
Reffert, S., Bergmann, C., Quirrenbach, A., Trifonov, T., & Künstler, A. 2015, A&A, 574, A116
Reichert, K., Reffert, S., Stock, S., Trifonov, T., & Quirrenbach, A. 2019, A&A, 625, A22
Ribas, Á., Bouy, H., & Merín, B. 2015, A&A, 576, A52
Roell, T., Neuhäuser, R., Seifahrt, A., & Mugrauer, M. 2012, A&A, 542, A92
Ryu, T., et al. 2016, ApJ, 825, 127
Saio, H., Wood, P. R., Takayama, M., & Ita, Y. 2015, MNRAS, 452, 3863
Santos, N. C., et al. 2017, A&A, 603, A30
Sato, B., et al. 2003, ApJ, 597, L157
Sato, B., et al. 2007, ApJ, 661, 527
Sato, B., et al. 2008a, PASJ, 60, 539
Sato, B., et al. 2008b, PASJ, 60, 1317
Sato, B., et al. 2010, PASJ, 62, 1063
Sato, B., et al. 2012, PASJ, 64, 135
Sato, B., et al. 2013a, ApJ, 762, 9
Sato, B., et al. 2013b, PASJ, 65, 85
Sato, B., et al. 2016, ApJ, 819, 59
Sato, B., Kambe, E., Takeda, Y., Izumiura, H., & Ando, H. 2002, PASJ, 54, 873
Sato, B., Kambe, E., Takeda, Y., Izumiura, H., Masuda, S., & Ando, H. 2005, PASJ, 57, 97
Schlaufman, K. C. 2018, ApJ, 853, 37
Schröder, K.-P., Mittag, M., Jack, D., Rodríguez Jiménez, A., & Schmitt, J. H. M. M. 2020, MNRAS, 492, 1110
Schwarz, G. 1978, Ann. Statist., 6, 461
Sekiguchi, M., & Fukugita, M. 2000, AJ, 120, 1072
Setiawan, J., Pasquini, L., da Silva, L., von der Lühe, O., & Hatzes, A. 2003, A&A, 397, 1151
Smirnov, N. 1948, Ann. Math. Statist., 19, 279
Sousa, S. G., et al. 2021, A&A, 656, A53
Stello, D., et al. 2017, MNRAS, 472, 4110
Takarada, T., et al. 2018, PASJ, 70, 59
Takeda, Y., Sato, B., & Murata, D. 2008, PASJ, 60, 781
Tala Pinto, M., Reffert, S., Quirrenbach, A., Stock, S., Trifonov, T., & Mitchell, D. S. 2020, A&A, 644, A1
Teng, H.-Y., et al. 2022a, PASJ, 74, 92
Teng, H.-Y., et al. 2022b, PASJ, 74, 1309
Teng, H.-Y., et al. 2023, PASJ, 75, 169
Virtanen, P., et al. 2020, Nature Methods, 17, 261
Vousden, W. D., Farr, W. M., & Mandel, I. 2016, MNRAS, 455, 1919
Wang, L., et al. 2014, PASJ, 66, 118
Wang, L., et al. 2012, Res. Astron. Astrophys., 12, 84
Winn, J. N., Johnson, J. A., Albrecht, S., Howard, A. W., Marcy, G. W., Crossfield, I. J., & Holman, M. J. 2009, ApJ, 703, L99
Wittenmyer, R. A., et al. 2016, ApJ, 818, 35
Wittenmyer, R. A., Endl, M., Wang, L., Johnson, J. A., Tinney, C. G., & O'Toole, S. J. 2011, ApJ, 743, 184
Wittenmyer, R. A., Jones, M. I., Zhao, J., Marshall, J. P., Butler, R. P., Tinney, C. G., Wang, L., & Johnson, J. A. 2017, AJ, 153, 51
Wittenmyer, R. A., Liu, F., Wang, L., Casagrande, L., Johnson, J. A., & Tinney, C. G. 2016, AJ, 152, 19
Wolthoff, V., Reffert, S., Quirrenbach, A., Jones, M. I., Wittenmyer, R. A., & Jenkins, J. S. 2022, A&A, 661, A63
Wright, J. T., Upadhyay, S., Marcy, G. W., Fischer, D. A., Ford, E. B., & Johnson, J. A. 2009, ApJ, 693, 1084
Xiao, G.-Y., et al. 2023, Res. Astron. Astrophys., 23, 055022
Yılmaz, M., et al. 2017, A&A, 608, A14
Zechmeister, M., & Kürster, M. 2009, A&A, 496, 577
Zhao, G., & Li, H.-B. 2001, Chin. J. Astron. Astrophys., 1, 555

Downloaded from https://academic.oup.com/pasj/article/75/6/1030/7272944 by ANKARA user on 22 December 2023

© The Author(s) 2023. Published by Oxford University Press on behalf of the Astronomical Society of Japan.
All rights reserved. For permissions, please e-mail: journals.permissions@oup.com